UC Berkeley
UC Berkeley Electronic Theses and Dissertations

Title
Design principles for ensuring robustness and efficiency in clathrin-mediated endocytosis revealed by mathematical modeling and quantitative imaging

Permalink
https://escholarship.org/uc/item/23t3c108

Author
Hassinger, Julian Edwin

Publication Date
2019

Peer reviewed|Thesis/dissertation

Design principles for ensuring robustness and efficiency in clathrin-mediated endocytosis
revealed by mathematical modeling and quantitative imaging

by

Julian Edwin Hassinger

A dissertation submitted in partial satisfaction of the

requirements for the degree of

Doctor of Philosophy

in

Biophysics

in the

Graduate Division

of the

University of California, Berkeley

Committee in charge:

Professor David G Drubin, Co-chair
Professor Padmini Rangamani, Co-chair
Professor James H Hurley
Professor Matthew D Welch

Summer 2019

Design principles for ensuring robustness and efficiency in clathrin-mediated endocytosis
revealed by mathematical modeling and quantitative imaging

Abstract

Design principles for ensuring robustness and efficiency in clathrin-mediated endocytosis
revealed by mathematical modeling and quantitative imaging

by

Julian Edwin Hassinger

Doctor of Philosophy in Biophysics

University of California, Berkeley

Professor David G Drubin, Co-chair

Professor Padmini Rangamani, Co-chair

Clathrin-mediated endocytosis (CME) is a highly conserved pathway in eukaryotes responsible for internalization of cell surface receptors and associated cargo, regulation of biochemical signaling pathways, and maintaining plasma membrane composition via the deformation and pinching off of a vesicle from the plasma membrane. Decades of work by the scientific community have served to identify over 60 different proteins that are directly involved in this process and to determine the relative timing and putative function of a large number of these proteins. One principle conclusion that could be drawn from this large body of work is that CME is both highly robust to perturbations as well as quite efficient in terms of the fraction of nascent endocytic sites that ultimately successfully internalize. The general principles that underlie this robustness and efficiency remained unclear as I began my graduate studies.

To investigate the mechanical robustness of CME, I performed continuum modeling of the shape progression of endocytic sites in response to a "protein coat" that can vary in size, stiffness, and spontaneous curvature. I demonstrated that elevated tension in the membrane stalls the progression of curvature, confirming the physical basis for similar observations made in experimental studies. Additionally, I found that the shape evolution of the membrane should undergo a *snapthrough instability* at physiologically relevant values of membrane tension, which might serve as both an energy and a kinetic barrier to membrane deformation. This instability can be avoided by either increasing the stiffness of the coat or by the action of external forces on the membrane, simulating the proposed role for actin polymerization at endocytic sites. Combining both increased coat stiffness and force from actin polymerization allows for vesiculation even under high membrane tension conditions. These results demonstrate that cells ensure the robustness of CME by employing redundant but complementary mechanisms for deforming the plasma membrane.

To explore how the high efficiency of CME is achieved, I sought to determine how progression through the pathway is regulated. Thus, I undertook a systematic imaging study in which I performed two-color live cell total internal reflection fluorescence (TIRF) microscopy on over two dozen strains of the budding yeast, *Saccharomyces cerevisiae.* Each strain expressed both a GFP-tagged endocytic protein and a red fluorophore-tagged reporter protein which were chosen so as to span the entirety of the CME pathway. Using automated tracking and association software, I extracted the fluorescence intensity over time of over 10,000 endocytic sites. This dataset not only recapitulates the canonical timeline for CME in budding yeast, but also reveals that there is substantially more variability in the timing and abundance of proteins in pathway than had previously been appreciated. Taking advantage of this inherent variability, I sought meaningful statistical correlations in the data that could give insight into the regulation of progression through the pathway. The lifetimes of proteins early in the endocytic pathway are highly correlated with one another, as are those of the late endocytic proteins. However, the lifetimes of the early proteins have no detectable correlation with their own abundances nor with the lifetimes or abundances of late-stage proteins. Taken together, these data quantitatively substantiate the existence of a regulatory transition point between early- and late-stage CME, as had previously been proposed in the absence of entirely conclusive evidence. Additional evidence indicates that progression through this point is regulated by the presence of cargo. This result suggests that cells not only optimize for efficiency in CME on the basis of internalization efficiency but also on a cost-benefit basis by setting a cargo requirement before membrane deformation is initiated.

These insights into the design principles for robustness and efficiency of CME build upon the foundations of past efforts to identify and characterize individual proteins in the endocytic pathway by expanding the focus to a systems level understanding of the process. Additionally, these results demonstrate the synergy of quantitative analysis and modeling in biology, which will become even more important as the tools for generating quantitative data in biology become ever more powerful and easy to use.

For George,

Who taught me there's no such thing as a free lunch

Contents

List of Figures

List of Tables

Acknowledgments

There are so many people I need to thank and acknowledge for helping me to get to this point in my career.

First, I need to thank my family for all of their love and support throughout the years. From the time when I was a precocious (and probably somewhat annoying) child reading and then regurgitating every fact that I could find about animals, all the way through my graduate studies, my parents have always been willing to listen when I rambled on about my scientific interests and encouraged me to pursue my passions. I've always tried to set a good example for my younger brothers, and I've been happy to see them grow into wonderful, confident young men during my time in grad school. My dog David Bowie has helped to keep me sane for the past few years, and I love him for it. I have to thank Jeff for his prophetic dream, my Aunt Chris for helping to get him, and my friends Ben and Hannah for living with and helping to train him.

My labmates and friends have also helped to made these past six years a wonderful time in my life and have helped me so much personally and professionally. The Comp Bio crew of Jeff, Amy, Brooke, Rob and Jim took me in early and have been my home base in Berkeley. All of my friends in Biophysics have made all of our retreats and recruitments a blast, and hopefully Raoul and I can carve out some beach time in the near future. My labmates have been constant sources of help and friendship over the years, and are by this point too numerous to list. A few special shoutouts go to my baymate Bob, who has become a very good friends through the years, Daniel, who somehow has made me into a runner, and Ross, with whom I started in lab and who is still my science hero.

I want to thank the Biophysics Graduate Group for taking a chance on me by bringing me in despite having last taken a biology course in senior year of high school. Actions generally speak louder than words, but I'm glad they listened to me when I said I wanted to bring my training in physics to bear on biology. A special thanks goes to Kate Chase who has made my life, and that of everyone in Biophysics and Comp Bio, so much easier than it otherwise could have been by handling so many things behind the scenes and various issues that arose throughout grad school.

I have to thank Padmini who was my first mentor when I started at Berkeley, and who has been with me every step of the way ever since, even as she's gone on to start her own group in San Diego. She gave me direction when I lacked it, encouragement when I sought it, and a couple of kicks in the pants when I needed it. I'm happy that I can count her as amongst my friends, even though I'm not sure she'll ever fully trust anyone who doesn't drink coffee.

I want to thank David and Georjana for having me in the lab all these years. They really care about all of us in the lab as both scientists and as people, which has attracted a lot of good people to the lab and made our lab environment a true pleasure to be a part of. David in particular has been like a father to me, and I'll miss having someone to talk to about Cal sports all the time. I never did become the experimentalist I think he'd hoped I might become when I joined the lab, but I like to think I've made him proud regardless.

A final acknowledgment has to be made for George Oster, whose curiosity and good humor inspire me still. It didn't occur to me when I started in George's group that I would be the last of his PhD students. I still miss when he would come into the office to talk to Jasmine, Mike, and me about science, Apple, and whatever else seemed interesting in the moment. George's life and career were fascinating and incredible, and I'm happy that I got the chance to have known the man himself.

Chapter 1

Introduction to clathrin-mediated endocytosis

1.1 Overview of clathrin-mediated endocytosis

Clathrin-mediated endocytosis (CME) is a highly conserved process in eukaryotes [1–3] in which a patch of the plasma membrane is invaginated and subsequently pinched off to form an internalized vesicle [4]. CME plays a critical role in the internalization of receptors and associated cargo on the plasma membrane [5], and it is by far the largest contributor to endocytic flux [6]. Over 60 different proteins that directly participate in CME have been identified [7]. Seminal studies in both budding yeast [8–10] and mammalian cells [11] have established that these proteins act as members of functional modules which can be classified by their relative timing and activity at endocytic sites.

Site initiation and cargo recruitment

A set of early and early coat proteins mark the site of a nascent endocytic site. They reside at these sites for a highly variable time before downstream proteins arrive [9, 12, 13]. The early stage proteins function mainly in site initiation and cargo selection [7]. The primary distinction between early and early coat proteins is that the coat proteins eventually internalize with later arriving coat proteins [9, 14, 15], whereas the other early proteins begin to dissociate from endocytic sites before invagination begins [12, 16]. Clathrin itself is one of the early-arriving coat proteins [9, 14].

Clathrin was first observed at coated pits over 50 years ago via electron microscopy [17]. In the years since, biochemical and structural studies revealed that clathrin forms heterohexameric complexes in the shape of three-legged spirals, known as triskelia, which can self-assemble into cage-like structures consisting of pentagons and hexagons [18]. While flat hexagonal lattices of clathrin have been observed in cells [19], purified clathrin, along with its associated adaptor complex, tends to form small closed structures similar to a soccer

ball [4]. It is thought that this seemingly preferred curvature of clathrin contributes to the bending of the plasma membrane at endocytic sites [20].

Despite its titular role, clathrin itself is not strictly required for productive CME in budding yeast, with only around a 50% reduction in cargo uptake [21] and late endocytic sites [9] in clathrin null mutants. CME will also proceed in the absence of nearly the entire early module (clathrin excluded), though uptake of cargo is severely impaired [22]. Similarly, mutants lacking either one or more of the early stage proteins have fewer late endocytic sites, but the dynamics of late-stage CME are faster [12, 15, 16]. A similar phenotype is observed in mammalian cells, wherein knockdown of the endocytic adaptor AP2 results in faster and more regular dynamics [23, 24]. However, the knockdown or deletion of endocytic adaptors significantly impairs cargo uptake [25, 26]. Thus, while the early stage of CME seems to be somewhat dispensable, it appears to be necessary for proper cargo uptake as well as regulating the dynamics of later stages of the pathway.

Membrane deformation and actin assembly

Clathrin and endocytic adaptor proteins alone are capable of deforming membranes *in vitro* [27]. In mammalian cells, this might also be the case — endocytic pits at all stages of membrane deformation can be seen even when scission of the endocytic pit is impaired [28, 29], and inhibition of actin assembly seems only to arrest endocytic sites in highly curved, though relatively shallow, states with wide necks [29, 30]. By contrast, force from actin assembly is required for substantial membrane bending in budding yeast [8], though whether the endocytic coat alone is capable of deforming the plasma membrane at all is a matter of some debate [31, 32].

Actin assembly at endocytic sites requires the Arp2/3 complex [33], manifesting as a branched filament network that is crosslinked by fimbrin [34, 35]. Actin filament nucleation and branching via the Arp2/3 complex in turn requires the presence of nucleation promoting factors (NPFs), most notably WASP/N-WASP in mammalian cells [36] and its homologue Las17 [9, 10] in budding yeast. The so-called WASP/Myosin complex is recruited by mid- and late-coat proteins that are downstream of the early coat [37, 38]. Force from actin polymerization, and possibly myosin motor activity [10, 32], is transduced to the plasma membrane via actin binding proteins residing in the endocytic coat [8, 39] and via anchoring to the base of endocytic sites by myosin [38, 40, 41]. In mammalian cells actin assembly at late stages of endocytosis appears to be regulated in part by coincidence detection of high curvature and phosphoinositide content at endocytic sites [42, 43]. What the ultrastructure of the actin network looks like and how exactly it contributes to successful CME are still open questions in the field.

Scission and uncoating

Scission requires that the membrane be constricted near the base of the endocytic pit such that the inner leaflets of the lipid bilayer can interact [44] to form a hemifission intermediate

[45] that resolves with an internalized vesicle. In mammalian cells, this requires the recruitment and activity of the GTPase dynamin [46], which converts energy from GTP hydrolysis into mechanical work that constricts the endocytic neck [47]. By contrast, the budding yeast dynamin homologue appears to be dispensable for CME under laboratory conditions [31], though some groups dispute this finding [48, 49]. Other candidates for the mechanism of scission in budding yeast include phospholipid-mediated line tension [44, 50], mechanical instability [51], and friction mediated forces [52]. Each of these mechanisms would require the binding of curvature-sensing BAR domain proteins [31] as well as generation of tension at the membrane neck. Scission by dynamin too requires its ability to bind curved membranes [53] as well membrane tension [54, 55].

Finally, uncoating of the nascent internalized vesicles is required for them to mature and fuse to endosomes as well as to release the protein machinery for subsequent rounds of CME [3]. Uncoating appears to be controlled by three main processes: breakage of clathrin-clathrin interactions [56], direct phosphorylation of the endocytic machinery [57], and dephosphorylation of phosphoinositides [58, 59]. Crucially, the proteins underlying all three of these mechanisms are recruited only at the very end of the CME pathway principally through interactions with dynamin in mammalian cells [60], or with actin-binding proteins in budding yeast [61]. This late recruitment ensures that endocytic sites are not disassembled prematurely, but also ensures that the components of failed endocytic sites [9, 31, 50] are recycled for further attempts at productive CME.

1.2   Mechanical forces in CME

In recent years, it has come to be appreciated that CME involves not only the sequential recruitment of proteins to endocytic sites, but that these proteins perform mechanical work to deform the plasma membrane [62]. This work is done against a host of opposing forces via various mechanisms of membrane deformation.

Opposing forces

- **Membrane rigidity**: Though the plasma membrane is typically regarded as quite flexible on a cellular scale, it is quite rigid at the scale of endocytic sites [63]. This rigidity is a consequence of lipid tails being exposed to water on one leaflet of a highly curved membrane with head groups being compressed on the other [64], both of which are entropically unfavorable. Due to bending energy and surface area both being quadratic in the membrane curvature, the same amount of energy is required to form a closed vesicle of any size [65]. Thus, the endocytic machinery must at minimum overcome an energy barrier that scales linearly with the bending rigidity of the bilayer. Reducing the stiffness of the membrane has been shown to increase the rate of CME in live cells [66].

- **Membrane tension**: To form an endocytic vesicle, membrane must be drawn into the endocytic bud against the mechanical tension in the plasma membrane. This tension is an energy per unit area that is essentially a measure of how exposed the phospholipid tails are to the surrounding aqueous environment [67]. Thus, mechanically stretching the membrane and increasing the area per lipid will increase this energy per unit area [68]. An additional source of "apparent" membrane tension, so called because it cannot be separated from the bilayer tension in typical mechanical measurements of membrane tension arises from the energy per unit area of membrane-cytoskeleton attachments [69]. The work that must be done against tension is linear in the both the tension and the area of the vesicle [51]. Experimental treatments known to increase the tension of the plasma membrane or of synthetic giant vesicles have been shown to inhibit deformation by clathrin coats [29, 70] as well as to stall CME under certain conditions [71].

- **Turgor pressure**: All cells have a pressure differential across their membranes due to the chemical potential arising from differing solute concentrations between the cytoplasm and the extracellular space [72]. Some organisms, like plants and fungi, actively maintain a high turgor pressure across their plasma membrane that is supported by their cell walls [73, 74]. Thus, turgor pressure is typically regarded as the dominant opposing force to membrane deformation in plants and fungi [75]. Because the energy of forming a vesicle against turgor pressure scales with the volume of the vesicle, whereas its receptor-bound cargo-carrying capacity presumably scales with the area of the vesicle, high turgor pressure in fungi and plants likely also explains the relatively small sizes of their endocytic vesicles [5].

- **Cargo crowding**: Steric crowding of cargo on the extracellular face of the plasma membrane represents a final entropic barrier that must be overcome to form an endocytic vesicle [76]. It is likely that cargo composition and density is thus limited by the ability of endocytic adaptors to bind and cluster their cargo at endocytic sites. It has been shown that reduction of the number of adaptors that bind bulky cargos results in smaller endocytic pits and faster dynamics while the reverse is true for the reduction of the number of adaptors that bind smaller cargos [23].

Mechanisms of membrane deformation

- **Indirect scaffolding by clathrin**: Clathrin has a tendency to self-assemble into closed, curved structures *in vitro*, and into even smaller, more regular cages in the presence of adaptor proteins [4]. It is believed that this preferred curvature is transduced to the plasma membrane to deform the membrane by binding adaptor proteins clustered at endocytic [27]. However, the fact that the clathrin-binding domainds of most clathrin adaptors are located in very flexible regions [77] makes it unclear how clathrin coat assembly would directly induce membrane curvature. I think it

rather more likely that clathrin serves primarily as a scaffold that clusters and concentrates other endocytic proteins that are capable of bending the membrane by other means. The high turnover rate of clathrin at endocytic sites [78] suggests a model in which clathrin triskelia rapidly bind and unbind to facilitate plasticity in the shape of the lattice while perhaps stabilizing and locking in curvature through more favorable clathrin-clathrin interactions [79] as curvature is produced via other mechanisms.

- **Amphipathic helix insertion**: A number of endocytic proteins bind the plasma membrane via the insertion of an amphipatic helix into the bilayer [62]. It has been proposed that insertion of a domain into the outer leaflet of the membrane would favor the production of curvature at sites of CME [80]. While this is a plausible mechanism for curvature production and likely makes some contribution, its impact has been estimated to been substantially lower than that of other curvature-generating mechanisms [76].

- **Direct scaffolding by BAR domain containing proteins**: BAR domain containing proteins form banana-shaped dimers that bind lipid bilayers via positive charge on one face or additionally via insertion of N-terminal amphipathic helices [81]. The characteristic curvature of different types of BAR domain proteins confers an ability to "sense" and preferentially bind membranes whose curvature matches their own [82]. These dimers also typically have end-to-end or side-by-side interactions that favor their assembly into helical arrays [83]. At high enough concentrations, they are capable of tubulating membranes both *in vitro* [84] and *in vivo* (achieved via overexpression) [82]. However, the cytosolic concentrations of these proteins is typically not as high has those required to tubulate membranes *in vitro* [85]. This relatively low concentration suggests that their curvature sensing capabilities are more important, potentially for stabilizing curvature [51], clustering certain lipid species [86], or positioning the recruitment or action of other membrane deformation mechanisms [87].

- **Steric crowding**: Steric pressure generated by the forced crowding of membrane-bound proteins is capable of generating curvature as a path to increase the space available to each protein and thus their entropy [88]. This effect is proportional to the size and density of the clustered proteins [89], and is especially potent for proteins with large intrinsically disordered domains, which have large hydroscopic radii [90]. A sizable fraction of endocytic proteins, including adaptor proteins and BAR domain proteins contain such intrinsically disordered domains [91, 92]. Thus, my favorite model for how the endocytic coat deforms the plasma membrane is that clathrin concentrates these bulky proteins at endocytic sites which then bend to relieve their steric crowding.

- **Actin assembly and myosin motor activity**: Forces from actin assembly and myosin motor activity are absolutely required for productive CME in budding yeast [8, 10]. The picture is less clear in mammalian cells, though it is clear that actin assembly can become essential under high membrane tension conditions [29].

- **Dynamin mechanochemical acitivity**: Dynamin GTPase activity is essential for scission in mammalian cells [53], whereas the picture in yeast is less clear [31, 48]. In any case, dynamin alone is capable of tubulating lipid bilayers as well as mediating scission [93]. It is been shown that dynamin forms helices, which constrict upon the completion of a GTP hydrolysis cycle [47]. Constriction can lead to scission at sites of high curvature [54] or membrane tension [94] both of which would cause packing defects in the bilayer that would tend to favor formation of a hemifission intermediate [45]. The lack of absolute necessity for dynamin in budding yeast suggests that its mechanochemical function may not have been the original CME scission mechanism, but perhaps has evolved to increase endocytic efficiency. However, this argument is somewhat undermined by the fact that dynamin is necessary for CME in plants [95], which are evolutionarily more distant from metazoans than fungi [96].

1.3 Robustness and efficiency of CME

CME is a highly robust process that can accomodate a number of pertubations to the protein machinery as well as challenging mechanical environments. In particular, many CME proteins in budding yeast, encompassing nearly the whole endocytic pathway [9, 22, 31], have been shown to be nonessential for productive vesicle internalization. This speaks to the presumed functional redundancy within modules of proteins [7]. The only truly essential functions carried out by the CME machinery in budding yeast appear to be recruitment of Arp2/3 complex NPFs to endocytic sites [37], actin binding by proteins embedded in the coat [8], and membrane anchoring and motor activity by myosin [10, 38]. In mammals, clathrin and AP2 both seem to be essential [97, 98], and functional dynamin is required for scission [53]. The host of other endocytic proteins thus seem mostly to ensure the robustness and efficiency of CME.

The machinery of CME is also highly flexible, as evidenced by the wide range of sizes of endocytic vesicles across different organisms [5]. This flexibility also manifests in the fact that CME is hijacked by many pathogens [99], some of which are substantially larger than typical clathrin coated pits [100], for entry into the cell. This plasticity ensures that CME can function across different cell types, mechanical environments, and can take in a wide array of cargos [5].

Underpinning all of these observations is that CME is very efficient both from a mechanical as well as an energetic standpoint. In wild-type budding yeast under laboratory conditions, nearly 100% of all endocytic sites successfully internalize [8]. This is despite the fact that the failure of one, or even 75% of endocytic sites is not lethal [31]. Additionally, rather than continuing to let a catastrophically failed endocytic site persist, actin assembly triggers the eventual disassembly of the endocytic coat [61], allowing it to be recycled for future rounds of assembly. Furthermore, the extended and variable residence times of early endocytic proteins [8, 12, 16], along with some evidence that cargo may play a role in gating the progression to later stages [15], suggests a model in which sites of CME must pass

through some form of cargo checkpoint before progressing to membrane deformation [101]. Maximizing efficiency of cargo uptake on a per site basis seems like a commonsense strategy to reduce the overall energy expenditure on CME.

In mammalian cells, the situation is somewhat more complicated, though the high conservation of the endocytic machinery between yeast and mammals [3] suggests similar general principles might apply. One particular source of controversy in the field is whether CME is as efficient in terms of internalization as is seen in yeast. Evidence from some studies points to the existence of "abortive" endocytic sites that disassemble before reaching later stages [102]. This is contradicted by a report that endocytic sites that acquire both clathrin and AP2 progress to completion the vast majority of the time [103]. This seeming disparity could be reconciled if an additional, perhaps cargo mediated, regulation step occurs to stabilize nascent endocytic sites.

The observation that CME is both mechanically robust as well as highly efficient in terms of progression through the pathway leads to some as yet unanswered questions: Is there a set of general principles that confers robustness to CME, even under mechanically challenging conditions? How is progression through the CME pathway regulated, and can the manner of this regulation give any insight into how the high efficiency of the process is maintained? In my graduate studies, I have sought to answer these two questions using a combination of mathematical modeling and quantitative imaging.

References

1. Kaksonen, M., Toret, C. P. & Drubin, D. G. Harnessing actin dynamics for clathrin-mediated endocytosis. *Nature reviews Molecular cell biology* **7,** 404–414 (2006).

2. Boettner, D. R., Chi, R. J. & Lemmon, S. K. Lessons from yeast for clathrin-mediated endocytosis. *Nature cell biology* **14,** 2 (2012).

3. Kaksonen, M. & Roux, A. Mechanisms of clathrin-mediated endocytosis. *Nature Reviews Molecular Cell Biology* **19,** 313 (2018).

4. Kirchhausen, T., Owen, D. & Harrison, S. C. Molecular structure, function, and dynamics of clathrin-mediated membrane traffic. *Cold Spring Harbor perspectives in biology* **6,** a016725 (2014).

5. McMahon, H. T. & Boucrot, E. Molecular mechanism and physiological functions of clathrin-mediated endocytosis. *Nature reviews Molecular cell biology* **12,** 517 (2011).

6. Bitsikas, V., Corrêa Jr, I. R. & Nichols, B. J. Clathrin-independent pathways do not contribute significantly to endocytic flux. *Elife* **3,** e03970 (2014).

7. Merrifield, C. J. & Kaksonen, M. Endocytic accessory factors and regulation of clathrin-mediated endocytosis. *Cold Spring Harbor perspectives in biology* **6,** a016733 (2014).

8. Kaksonen, M., Sun, Y. & Drubin, D. G. A pathway for association of receptors, adaptors, and actin during endocytic internalization. *Cell* **115,** 475–487 (2003).

9. Kaksonen, M., Toret, C. P. & Drubin, D. G. A modular design for the clathrin-and actin-mediated endocytosis machinery. *Cell* **123,** 305–320 (2005).

10. Sun, Y., Martin, A. C. & Drubin, D. G. Endocytic internalization in budding yeast requires coordinated actin nucleation and myosin motor activity. *Developmental cell* **11,** 33–46 (2006).

11. Taylor, M. J., Perrais, D. & Merrifield, C. J. A high precision survey of the molecular dynamics of mammalian clathrin-mediated endocytosis. *PLoS biology* **9,** e1000604 (2011).

12. Stimpson, H. E., Toret, C. P., Cheng, A. T., Pauly, B. S. & Drubin, D. G. Early-arriving Syp1p and Ede1p function in endocytic site placement and formation in budding yeast. *Molecular biology of the cell* **20,** 4640–4651 (2009).

13. Merrifield, C. J., Feldman, M. E., Wan, L. & Almers, W. Imaging actin and dynamin recruitment during invagination of single clathrin-coated pits. *Nature cell biology* **4,** 691 (2002).

14. Newpher, T. M., Smith, R. P., Lemmon, V. & Lemmon, S. K. In vivo dynamics of clathrin and its adaptor-dependent recruitment to the actin-based endocytic machinery in yeast. *Developmental cell* **9,** 87–98 (2005).

15. Carroll, S. Y. *et al.* Analysis of yeast endocytic site formation and maturation through a regulatory transition point. *Molecular biology of the cell* **23,** 657–668 (2012).

16. Peng, Y. *et al.* Casein kinase 1 promotes initiation of clathrin-mediated endocytosis. *Developmental cell* **32,** 231–240 (2015).

17. Roth, T. F. & Porter, K. R. Yolk protein uptake in the oocyte of the mosquito Aedes aegypti. L. *The Journal of cell biology* **20,** 313–332 (1964).

18. Kirchhausen, T. Clathrin. *Annual review of biochemistry* **69,** 699–727 (2000).

19. Heuser, J. Three-dimensional visualization of coated vesicle formation in fibroblasts. *The Journal of cell biology* **84,** 560–583 (1980).

20. Musacchio, A. *et al.* Functional organization of clathrin in coats: combining electron cryomicroscopy and X-ray crystallography. *Molecular cell* **3,** 761–770 (1999).

21. Payne, G. S., Baker, D., van Tuinen, E. & Schekman, R. Protein transport to the vacuole and receptor-mediated endocytosis by clathrin heavy chain-deficient yeast. *The Journal of Cell Biology* **106,** 1453–1461 (1988).

22. Brach, T., Godlee, C., Moeller-Hansen, I., Boeke, D. & Kaksonen, M. The initiation of clathrin-mediated endocytosis is mechanistically highly flexible. *Current Biology* **24,** 548–554 (2014).

23. Miller, S. E. *et al.* CALM regulates clathrin-coated vesicle size and maturation by directly sensing and driving membrane curvature. *Developmental cell* **33,** 163–175 (2015).

24. Dambournet, D. *et al.* Genome-edited human stem cells expressing fluorescently labeled endocytic markers allow quantitative analysis of clathrin-mediated endocytosis during differentiation. *J Cell Biol* **217,** 3301–3311 (2018).

25. Sorkin, A. Cargo recognition during clathrin-mediated endocytosis: a team effort. *Current opinion in cell biology* **16,** 392–399 (2004).

26. Carroll, S. Y. *et al.* A yeast killer toxin screen provides insights into a/b toxin entry, trafficking, and killing mechanisms. *Developmental cell* **17,** 552–560 (2009).

27. Dannhauser, P. N. & Ungewickell, E. J. Reconstitution of clathrin-coated bud and vesicle formation with minimal components. *Nature cell biology* **14,** 634 (2012).

28. Park, R. J. *et al.* Dynamin triple knockout cells reveal off target effects of commonly used dynamin inhibitors. *J Cell Sci* **126,** 5305–5312 (2013).

29. Boulant, S., Kural, C., Zeeh, J.-C., Ubelmann, F. & Kirchhausen, T. Actin dynamics counteract membrane tension during clathrin-mediated endocytosis. *Nature cell biology* **13,** 1124 (2011).

30. Yarar, D., Waterman-Storer, C. M. & Schmid, S. L. A dynamic actin cytoskeleton functions at multiple stages of clathrin-mediated endocytosis. *Molecular biology of the cell* **16,** 964–975 (2005).

31. Kishimoto, T. *et al.* Determinants of endocytic membrane geometry, stability, and scission. *Proceedings of the National Academy of Sciences* **108,** E979–E988 (2011).

32. Idrissi, F.-Z., Blasco, A., Espinal, A. & Geli, M. I. Ultrastructural dynamics of proteins involved in endocytic budding. *Proceedings of the National Academy of Sciences* **109,** E2587–E2594 (2012).

33. Galletta, B. J., Chuang, D. Y. & Cooper, J. A. Distinct roles for Arp2/3 regulators in actin assembly and endocytosis. *PLoS biology* **6,** e1 (2008).

34. Kübler, E. & Riezman, H. Actin and fimbrin are required for the internalization step of endocytosis in yeast. *The EMBO journal* **12,** 2855–2862 (1993).

35. Skau, C. T. *et al.* Actin filament bundling by fimbrin is important for endocytosis, cytokinesis, and polarization in fission yeast. *Journal of Biological Chemistry* **286,** 26964–26977 (2011).

36. Merrifield, C. J., Qualmann, B., Kessels, M. M. & Almers, W. Neural Wiskott Aldrich Syndrome Protein (N-WASP) and the Arp2/3 complex are recruited to sites of clathrin-mediated endocytosis in cultured fibroblasts. *European journal of cell biology* **83,** 13–18 (2004).

37. Sun, Y., Leong, N. T., Wong, T. & Drubin, D. G. A Pan1/End3/Sla1 complex links Arp2/3-mediated actin assembly to sites of clathrin-mediated endocytosis. *Molecular biology of the cell* **26,** 3841–3856 (2015).

38. Lewellyn, E. B. *et al.* An engineered minimal WASP-myosin fusion protein reveals essential functions for endocytosis. *Developmental cell* **35,** 281–294 (2015).

39. Engqvist-Goldstein, Å. E. *et al.* The actin-binding protein Hip1R associates with clathrin during early stages of endocytosis and promotes clathrin assembly in vitro. *The Journal of cell biology* **154,** 1209–1224 (2001).

40. Pedersen, R. T. & Drubin, D. G. Type I myosins anchor actin assembly to the plasma membrane during clathrin-mediated endocytosis. *J Cell Biol* **218,** 1138–1147 (2019).

41. Mund, M. *et al.* Systematic nanoscale analysis of endocytosis links efficient vesicle formation to patterned actin nucleation. *Cell* **174,** 884–896 (2018).

42. Schöneberg, J. *et al.* Lipid-mediated PX-BAR domain recruitment couples local membrane constriction to endocytic vesicle fission. *Nature communications* **8,** 15873 (2017).

43. Daste, F. *et al.* Control of actin polymerization via the coincidence of phosphoinositides and high membrane curvature. *J Cell Biol* **216,** 3745–3765 (2017).

44. Liu, J., Kaksonen, M., Drubin, D. G. & Oster, G. Endocytic vesicle scission by lipid phase boundary forces. *Proceedings of the National Academy of Sciences* **103,** 10277–10282 (2006).

45. Kozlovsky, Y. & Kozlov, M. M. Membrane fission: model for intermediate structures. *Biophysical journal* **85,** 85–96 (2003).

46. Marks, B. *et al.* GTPase activity of dynamin and resulting conformation change are essential for endocytosis. *Nature* **410,** 231 (2001).

47. Zhang, P. & Hinshaw, J. E. Three-dimensional reconstruction of dynamin in the constricted state. *Nature cell biology* **3,** 922 (2001).

48. Smaczynska-de Rooij, I. I. *et al.* A role for the dynamin-like protein Vps1 during endocytosis in yeast. *J Cell Sci* **123,** 3496–3506 (2010).

49. Palmer, S. E. *et al.* A dynamin-actin interaction is required for vesicle scission during endocytosis in yeast. *Current Biology* **25,** 868–878 (2015).

50. Liu, J., Sun, Y., Drubin, D. G. & Oster, G. F. The mechanochemistry of endocytosis. *PLoS biology* **7,** e1000204 (2009).

51. Walani, N., Torres, J. & Agrawal, A. Endocytic proteins drive vesicle growth via instability in high membrane tension environment. *Proceedings of the National Academy of Sciences* **112,** E1423–E1432 (2015).

52. Simunovic, M. *et al.* Friction mediates scission of tubular membranes scaffolded by BAR proteins. *Cell* **170,** 172–184 (2017).

53. Antonny, B. *et al.* Membrane fission by dynamin: what we know and what we need to know. *The EMBO journal* **35,** 2270–2284 (2016).

54. Roux, A. *et al.* Membrane curvature controls dynamin polymerization. *Proceedings of the National Academy of Sciences* **107,** 4141–4146 (2010).

55. Morlot, S. *et al.* Membrane shape at the edge of the dynamin helix sets location and duration of the fission reaction. *Cell* **151,** 619–629 (2012).

56. Fotin, A. *et al.* Structure of an auxilin-bound clathrin coat and its implications for the mechanism of uncoating. *Nature* **432,** 649 (2004).

57. Smythe, E. & Ayscough, K. R. The Ark1/Prk1 family of protein kinases. *EMBO reports* **4,** 246–251 (2003).

58. Rusk, N. *et al.* Synaptojanin 2 functions at an early step of clathrin-mediated endocytosis. *Current Biology* **13,** 659–663 (2003).

59. Sun, Y., Carroll, S., Kaksonen, M., Toshima, J. Y. & Drubin, D. G. PtdIns (4, 5) P2 turnover is required for multiple stages during clathrin-and actin-dependent endocytic internalization. *The Journal of cell biology* **177,** 355–367 (2007).

60. Lee, D.-w., Wu, X., Eisenberg, E. & Greene, L. E. Recruitment dynamics of GAK and auxilin to clathrin-coated pits during endocytosis. *J Cell Sci* **119,** 3502–3512 (2006).

61. Cope, M. J. T., Yang, S., Shang, C. & Drubin, D. G. Novel protein kinases Ark1p and Prk1p associate with and regulate the cortical actin cytoskeleton in budding yeast. *The Journal of cell biology* **144,** 1203–1218 (1999).

62. Johannes, L., Wunder, C. & Bassereau, P. Bending "on the rocks" – a cocktail of biophysical modules to build endocytic pathways. *Cold Spring Harbor perspectives in biology* **6,** a016741 (2014).

63. Dimova, R. Recent developments in the field of bending rigidity measurements on membranes. *Advances in colloid and interface science* **208,** 225–234 (2014).

64. Seifert, U. Configurations of fluid membranes and vesicles. *Advances in physics* **46,** 13–137 (1997).

65. Helfrich, W. Elastic properties of lipid bilayers: theory and possible experiments. *Zeitschrift für Naturforschung C* **28,** 693–703 (1973).

66. Pinot, M. *et al.* Polyunsaturated phospholipids facilitate membrane deformation and fission by endocytic proteins. *Science* **345,** 693–697 (2014).

67. Rangamani, P., Agrawal, A., Mandadapu, K. K., Oster, G. & Steigmann, D. J. Interaction between surface shape and intra-surface viscous flow on lipid membranes. *Biomechanics and modeling in mechanobiology* **12,** 833–845 (2013).

68. Evans, E. A., Waugh, R. & Melnik, L. Elastic area compressibility modulus of red cell membrane. *Biophysical Journal* **16,** 585–595 (1976).

69. Diz-Muñoz, A., Fletcher, D. A. & Weiner, O. D. Use the force: membrane tension as an organizer of cell shape and motility. *Trends in cell biology* **23,** 47–53 (2013).

70. Saleem, M. *et al.* A balance between membrane elasticity and polymerization energy sets the shape of spherical clathrin coats. *Nature communications* **6,** 6249 (2015).

71. Ferguson, J. P. *et al.* Mechanoregulation of clathrin-mediated endocytosis. *J Cell Sci* **130,** 3631–3636 (2017).

72. Scher-Zagier, J. K. & Carlsson, A. E. Local turgor pressure reduction via channel clustering. *Biophysical journal* **111,** 2747–2756 (2016).

73. Winship, L. J., Obermeyer, G., Geitmann, A. & Hepler, P. K. Under pressure, cell walls set the pace. *Trends in plant science* **15,** 363–369 (2010).

74. Basu, R., Munteanu, E. L. & Chang, F. Role of turgor pressure in endocytosis in fission yeast. *Molecular biology of the cell* **25,** 679–687 (2014).

75. Dmitrieff, S. & Nédélec, F. Membrane mechanics of endocytosis in cells with turgor. *PLoS computational biology* **11,** e1004538 (2015).

76. Stachowiak, J. C., Brodsky, F. M. & Miller, E. A. A cost–benefit analysis of the physical mechanisms of membrane curvature. *Nature cell biology* **15,** 1019 (2013).

77. Kelly, B. T. *et al.* AP2 controls clathrin polymerization with a membrane-activated switch. *Science* **345,** 459–463 (2014).

78. Avinoam, O., Schorb, M., Beese, C. J., Briggs, J. A. & Kaksonen, M. Endocytic sites mature by continuous bending and remodeling of the clathrin coat. *Science* **348,** 1369–1372 (2015).

79. Den Otter, W. K. & Briels, W. J. The generation of curved clathrin coats from flat plaques. *Traffic* **12,** 1407–1416 (2011).

80. Ford, M. G. *et al.* Curvature of clathrin-coated pits driven by epsin. *Nature* **419,** 361 (2002).

81. Simunovic, M., Voth, G. A., Callan-Jones, A. & Bassereau, P. When physics takes over: BAR proteins and membrane curvature. *Trends in cell biology* **25,** 780–792 (2015).

82. Peter, B. J. *et al.* BAR domains as sensors of membrane curvature: the amphiphysin BAR structure. *Science* **303,** 495–499 (2004).

83. Simunovic, M., Srivastava, A. & Voth, G. A. Linear aggregation of proteins on the membrane as a prelude to membrane remodeling. *Proceedings of the National Academy of Sciences* **110,** 20396–20401 (2013).

84. Gallop, J. L. *et al.* Mechanism of endophilin N-BAR domain-mediated membrane curvature. *The EMBO journal* **25,** 2898–2910 (2006).

85. Mim, C. *et al.* Structural basis of membrane bending by the N-BAR protein endophilin. *Cell* **149,** 137–145 (2012).

86. Zhao, H. *et al.* Membrane-sculpting BAR domains generate stable lipid microdomains. *Cell reports* **4,** 1213–1223 (2013).

87. Takei, K., Slepnev, V. I., Haucke, V. & De Camilli, P. Functional partnership between amphiphysin and dynamin in clathrin-mediated endocytosis. *Nature cell biology* **1,** 33 (1999).

88. Stachowiak, J. C. *et al.* Membrane bending by protein–protein crowding. *Nature cell biology* **14,** 944 (2012).

89. Derganc, J. & Čopič, A. Membrane bending by protein crowding is affected by protein lateral confinement. *Biochimica et Biophysica Acta (BBA)-Biomembranes* **1858,** 1152–1159 (2016).

90. Busch, D. J. *et al.* Intrinsically disordered proteins drive membrane curvature. *Nature communications* **6,** 7875 (2015).

91. Snead, W. T. *et al.* Membrane fission by protein crowding. *Proceedings of the National Academy of Sciences* **114,** E3258–E3267 (2017).

92. Zeno, W. F. *et al.* Synergy between intrinsically disordered domains and structured proteins amplifies membrane curvature sensing. *Nature communications* **9,** 4152 (2018).

93. Sweitzer, S. M. & Hinshaw, J. E. Dynamin undergoes a GTP-dependent conformational change causing vesiculation. *Cell* **93,** 1021–1029 (1998).

94. Roux, A., Uyhazi, K., Frost, A. & De Camilli, P. GTP-dependent twisting of dynamin implicates constriction and tension in membrane fission. *Nature* **441,** 528 (2006).

95. Chen, X., Irani, N. G. & Friml, J. Clathrin-mediated endocytosis: the gateway into plant cells. *Current opinion in plant biology* **14,** 674–682 (2011).

96. Wang, D. Y.-C., Kumar, S. & Hedges, S. B. Divergence time estimates for the early history of animal phyla and the origin of plants, animals and fungi. *Proceedings of the Royal Society of London. Series B: Biological sciences* **266,** 163–171 (1999).

97. Perrais, D. & Merrifield, C. J. Dynamics of endocytic vesicle creation. *Developmental cell* **9,** 581–592 (2005).

98. Mitsunari, T. *et al.* Clathrin adaptor AP-2 is essential for early embryonal development. *Molecular and cellular biology* **25,** 9318–9323 (2005).

99. Cossart, P. & Helenius, A. Endocytosis of viruses and bacteria. *Cold Spring Harbor perspectives in biology* **6,** a016972 (2014).

100. Cureton, D. K., Massol, R. H., Saffarian, S., Kirchhausen, T. L. & Whelan, S. P. Vesicular stomatitis virus enters cells through vesicles incompletely coated with clathrin that depend upon actin for internalization. *PLoS pathogens* **5,** e1000394 (2009).

101. Layton, A. T. *et al.* Modeling vesicle traffic reveals unexpected consequences for Cdc42p-mediated polarity establishment. *Current Biology* **21,** 184–194 (2011).

102. Aguet, F., Antonescu, C. N., Mettlen, M., Schmid, S. L. & Danuser, G. Advances in analysis of low signal-to-noise images link dynamin and AP2 to the functions of an endocytic checkpoint. *Developmental cell* **26,** 279–291 (2013).

103. Hong, S. H., Cortesio, C. L. & Drubin, D. G. Machine-learning-based analysis in genome-edited cells reveals the efficiency of clathrin-mediated endocytosis. *Cell reports* **12,** 2121–2130 (2015).

Chapter 2

Design principles for robust vesiculation in clathrin-mediated endocytosis

2.1 Introduction

Clathrin-mediated endocytosis (CME), an essential cellular process in eukaryotes, is an archetypical example of a membrane deformation process that takes as input multiple variables such as membrane bending, tension, protein-induced spontaneous curvature and actin-mediated forces, and generates vesicular morphologies as its output [1]. Though more than 60 different protein species act in a coordinated manner during CME [2], we can distill this process into a series of mechanochemical events where a feedback between the biochemistry of the protein machinery and the mechanics of the plasma membrane and the actin cytoskeleton control endocytic patch topology and morphology [3, 4].

In Figure 2.1, I outline the main steps that lead to bud formation. Despite the complexity of CME, a variety of experimental approaches have served to identify the governing principles of bud formation in CME. I have identified a few key features from recent experiments that govern bud formation and have summarized the main results below.

- **Protein-induced spontaneous curvature**: A critical step in CME is the assembly of a multicomponent protein coat that clusters cargo and bends the membrane into a budded morphology. Clathrin assembles into a lattice-like cage on the membrane with the assistance of adaptor proteins that directly bind lipids [6, 7]. This assembly is generally thought to act as a scaffold that imposes its curvature on the underlying membrane [8]. Recent work suggests that other components of the coat can also contribute to membrane bending through scaffolding by F-BAR domains, amphipathic helix insertion into the bilayer, and adaptor protein crowding [6, 9–11]. Crowding of cargo molecules on the outer leaflet of the plasma membrane opposes invagination of the membrane [11, 12]; we can think of this effect as simply a negative contribution
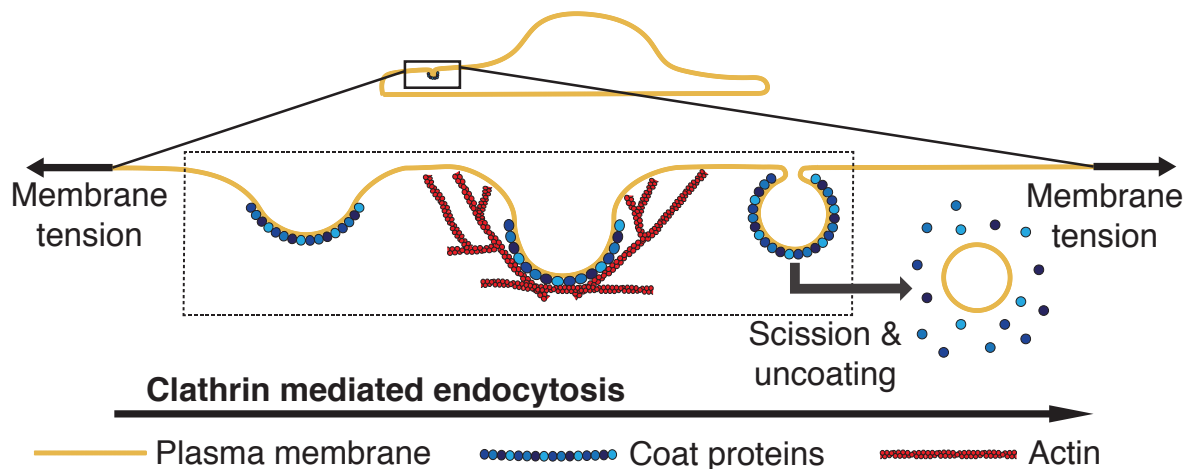
Figure 2.1: Schematic depiction of the main mechanical steps in clathrin-mediated endocytosis. A multi-component protein coat forms on the plasma membrane and causes the membrane to bend inwards, forming a shallow pit. As the coat matures, the membrane becomes deeply invaginated to form an open, U-shaped pit before constricting to form a closed, Ω-shaped bud. The bud subsequently undergoes scission to form an internalized vesicle and the coat is recycled. Actin polymerization is thought to provide a force, $\mathbf{f}$, to facilitate these morphological changes, particularly at high membrane tensions [5]. Our study is focused on understanding the impact of membrane tension on the morphological changes effected by the coat and actin polymerization, as indicated by the dashed box.

to the curvature of the coat. The contributions from each of these membrane bending mechanisms can be combined into a single measure of the curvature generating capability of the coat, or spontaneous curvature, with an effective strength that depends on its composition, density and area coverage [13, 14].

- **Membrane properties (moduli)**: The bending modulus, or rigidity, of the plasma membrane is a material property of the lipid bilayer describing its resistance to bending, and is determined by its composition [15]. This bending rigidity is generally thought to be the primary opposing force to membrane deformations [16]. Supporting this idea, a decrease in the bending rigidity of the plasma membrane by incorporation of polyunsaturated phospholipids was found to stimulate an uptake of transferrin, a hallmark of increased endocytic dynamics [17].

- **Membrane tension**: The plasma membrane of animal cells is under tension as a result of in-plane stresses in the bilayer and connections between the membrane and the underlying actomyosin cortex [18, 19]. It has been demonstrated *in vitro* that membrane tension opposes deformations to the membrane by curvature-generating proteins [20]. *In vivo*, elevated tension in combination with actin inhibitors causes clathrin-coated pits (CCPs) to exhibit longer lifetimes and increased the number of long-lived, presumably stalled, pits [5]. Under these conditions, open, U-shaped pits were found to be enriched as compared to closed, Ω-shaped pits when visualized by

electron microscopy [5, 21]. Similar observations have been made in a reconstituted system where purified coat proteins were able to substantially deform synthetic lipid vesicles under low tension but were stalled at shallow, U-shaped pits at a higher tension [22]. Additionally, membrane tension has been shown to induce disassembly of caveolae [23] as well as flattening of exocytic vesicles following fusion to the plasma membrane [24].

- **Force from actin polymerization**: It has long been appreciated that actin polymerization is an essential component in the CME pathway in yeast [25], presumably due to the high turgor pressure in this organism [26, 27]. In recent years, it has become clear that actin plays an important role in mammalian CME in conditions of high membrane tension [5] and to uptake large cargos like virus particles [28, 29].

From these studies, we can conclude that there are multiple variables that control the budding process, and are particularly dependent on the cell type and specific process. In whole cells, many different variables are at play simultaneously. There remain substantial challenges associated with identifying the separate contributions from each of these factors through experimental approaches. The diffraction-limited size of CCPs (~ 100 nm) makes it currently impossible to directly image the morphology of the membrane in situ in living cells. The temporal regularity of yeast CME has allowed for the visualization of time-resolved membrane shapes in this organism using correlative fluorescence and electron microscopy [30, 31]. However, this approach is quite difficult to use in mammalian cells because of the wide distribution of CCP lifetimes [32, 33]. Additionally, current techniques are only capable of measuring global tension [19, 34, 35], making it nearly impossible to determine how local membrane tension impacts the progression of membrane deformation at a given CCP. Beyond this, it is difficult to perturb the composition and tension of the plasma membrane in a controlled and quantitative way.

Reconstitution of membrane budding *in vitro* allows for control of lipid and protein composition as well as membrane tension [8, 22, 36]. However, coat area is an uncontrolled variable in these studies, and explicitly varying the spontaneous curvature would be challenging because the connection between individual molecular mechanisms of curvature generation and spontaneous curvature is not fully understood. Additionally, controlled application of force from actin polymerization at single sites of membrane budding has not yet been possible.

For these reasons, I chose to pursue a computational approach that allowed me to explore how each of the factors that governs budding contributes to morphological progression of membrane budding, when varied in isolation or in various combinations.

Mathematical modeling has proven to be a powerful approach to describe observed shapes of membranes in a wide variety of contexts, from shapes of red blood cells to shape transformations of vesicles [13, 37]. In recent years, mathematical modeling has provided insight into various aspects of membrane deformation in number of budding phenomena including domain-induced budding, caveolae, ESCRTs, and CME [38–40]. For example, Liu et al.

showed that a line tension at a lipid phase boundary could drive scission in yeast [3, 41], while Walani et al. showed that scission could be achieved via snapthrough transition at high membrane tension [42]. These studies and others [27, 43, 44] have demonstrated the utility of membrane modeling approaches for studying CME. However, none have systematically explored how the various parameters described above come together to determine the success or failure of budding.

In this chapter, I seek to answer the following questions: How does membrane tension affect the morphological progression of endocytic pits? How do the various mechanisms of membrane bending interact to overcome the effects of high tension and form buds? What are the design principles for robust vesiculation?

2.2   Model description

Assumptions

1. The lipid bilayer is modeled as a two-dimensional differentiable manifold endowed with mechanical properties. Helfrich proposed a model that treats the manifold as a thin elastic shell. The bending behavior of the membrane is captured by an energy functional that depends only on the manifold's local curvatures [13]. This model and its variants are valid for radii of curvatures much larger than the membrane thickness. I will assume that the Helfrich energy is sufficient to describe the membrane during clathrin-mediated endocytosis, since an endocytic vesicle is roughly 50 nm in radius [12].

2. The membrane is assumed to be at mechanical equilibrium at all times. Because clathrin-mediated endocytosis occurs over a timescale of tens of seconds [2, 5, 32, 33, 45], this assumption is valid [3, 27]. I do not include explicit time dependence arising from the viscosity of the bilayer or the surrounding fluid or due to lipid and protein diffusion. This is a focus of future work.

3. The lipid bilayer is assumed to be incompressible/inextenisble, based on a large stretch modulus [46]. This constraint is introduced using a Lagrange multiplier γ (see Table 2.1 for notation).

4. Protein adsorption on the membrane (*i.e.* the clathrin coat) is represented using spontaneous curvature (C). Since I am modeling the membrane as a single manifold, the notion of intrinsic curvature due to different lipids or proteins interacting with each leaflet is represented by this term [13, 47, 48].

5. For ease of computation, I assumed that endocytic pit is rotationally symmetric. This allowed me to obtain solutions capturing the whole budding process with a relatively simple parameterization of the surface.

Equilibrium equations

Here I present a concise derivation of the equilibrium equations for biological membranes. Detailed derivations are presented in [47, 49, 50].

The local force balance, based on the conservation of linear momentum, and in the absence of inertia is

$$\mathbf{div}\ \boldsymbol{\sigma} + p\mathbf{n} = \mathbf{f}. \tag{2.1}$$

Here, $\mathbf{div}$ denotes the surface divergence, $\boldsymbol{\sigma}$ are the stress vectors, p is the pressure difference across the membrane, $\mathbf{n}$ is the surface normal, and $\mathbf{f}$ is the externally applied force. The surface stresses can be expressed as

$$\boldsymbol{\sigma}^\alpha = \mathbf{T}^\alpha + S^\alpha \mathbf{n}, \tag{2.2}$$

and the surface divergence is expressed as

$$\mathbf{div}\ \boldsymbol{\sigma} = \boldsymbol{\sigma}^\alpha_{;\alpha} = (\sqrt{a})^{-1}(\sqrt{a}\boldsymbol{\sigma}^\alpha)_{,\alpha}. \tag{2.3}$$

$()_{;\alpha}$ denotes the covariant derivative. It should be noted that $\mathbf{T}^\alpha$ and S^α need to be constitutively determined. In this case, if $F(H, K; x^\alpha)$ is the elastic energy density per unit mass of the surface [49, 50], then S^α and the individual components of the $\mathbf{T}^\alpha$ are given by

$$\mathbf{T}^\alpha = T^{\beta\alpha}\mathbf{a}_\beta \quad \text{with} \quad T^{\beta\alpha} = \sigma^{\beta\alpha} + b^\beta_\mu M^{\mu\alpha}, \quad \text{and} \quad S^\alpha = -M^{\alpha\beta}_{;\beta}, \tag{2.4}$$

where

$$\sigma^{\beta\alpha} = \rho(\frac{\partial F}{\partial a_{\alpha\beta}} + \frac{\partial F}{\partial a_{\beta\alpha}}) \quad \text{and} \quad M^{\beta\alpha} = \frac{1}{2}\rho(\frac{\partial F}{\partial b_{\alpha\beta}} + \frac{\partial F}{\partial b_{\beta\alpha}}), \tag{2.5}$$

see [50] for a full derivation. For an elastic membrane that responds to out-of-plane bending and is area incompressible, the general form for the free energy density per unit mass can be rewritten as

$$F(\rho, H, K; x^\alpha) = \bar{F}(H, K; x^\alpha) - \gamma(x^\alpha, t)/\rho, \tag{2.6}$$

where $\gamma(x^\alpha, t)$ is a Lagrange multiplier required to implement the constraint $\rho(x^\alpha, t)$ is constant or the local area dilation $J = 1$, H and K are the mean and Gaussian curvatures respectively. Substituting $W = \rho\bar{F}$ and invoking the definitions of the mean and Gaussian curvatures, $H = \frac{1}{2}a^{\alpha\beta}b_{\alpha\beta}$ and $K = \frac{1}{2}\varepsilon^{\alpha\beta}\varepsilon^{\lambda\mu}b_{\alpha\lambda}b_{\beta\mu}$, in terms of the induced metric and curvature tensors $a^{\alpha\beta} = (a_{\alpha\beta})^{-1}$ and $b^{\alpha\beta} = a^{\alpha\lambda}a^{\beta\mu}b_{\lambda\mu}$, respectively, Eq. (2.6) can be rewritten as

$$\begin{aligned} \sigma^{\alpha\beta} &= (\lambda + W)a^{\alpha\beta} - (2HW_H + 2\kappa W_K)a^{\alpha\beta} + W_H\tilde{b}^{\alpha\beta}, \\ M^{\alpha\beta} &= \frac{1}{2}W_H a^{\alpha\beta} + W_K\tilde{b}^{\alpha\beta}, \end{aligned} \tag{2.7}$$

where

$$\lambda = -(\gamma + W). \tag{2.8}$$

Using Eqs. (2.7), (2.4) and (2.2), the equations of motion Eq. (2.1) can then be reduced to

$$p + \mathbf{f} \cdot \mathbf{n} = \Delta(\frac{1}{2}W_H) + (W_K)_{;\alpha\beta}\tilde{b}^{\alpha\beta} + W_H(2H^2 - K) + 2H(KW_K - W) - 2\lambda H, \quad (2.9)$$

and

$$N^{\beta\alpha}_{;\alpha} - S^\alpha b^\beta_\alpha = -(\gamma_{,\alpha} + W_K K_{,\alpha} + W_H H_{,\alpha})a^{\beta\alpha} = (\partial W/\partial x^\alpha_{|\exp} + \lambda_{,\alpha})a^{\beta\alpha} = 0, \quad (2.10)$$

Here $\Delta(\cdot) = (\cdot)_{;\alpha\beta}a^{\alpha\beta}$ is the surface Laplacian and $()_{|\exp}$ represents the explicit derivative with respect to θ^α.

Helfrich energy elastic model

For a lipid-bilayer membrane, we write the local energy density as a modified form of the Helfrich energy

$$W = \kappa(\theta^\alpha)\left[H - C(\theta^\alpha)\right]^2 + \kappa_G(\theta^\alpha)K, \quad (2.11)$$

where $C\,(\theta^\alpha)$ is the spontaneous curvature that can depend on the coordinates. This energy function differs from the standard Helfrich energy by a factor of 2, with the net effect being that our value for the bending modulus, κ, is twice that of the standard bending modulus typically encountered in the literature [13].

The equations of motion (2.9) and (2.10) for an elastic membrane reduce to

$$\Delta\left[\kappa\,(H - C)\right] + 2H\Delta\kappa_G - (\kappa_G)_{;\alpha\beta}\,b^{\alpha\beta} + 2\kappa\,(H - C)\left(2H^2 - K\right) - 2\kappa H\,(H - C)^2$$
$$= p + 2\lambda H + \mathbf{f} \cdot \mathbf{n}, \quad (2.12)$$

$$\underbrace{\lambda_{,\alpha}}_{\text{Gradient of surface tension}} = \underbrace{-\frac{\partial\kappa}{\partial\theta^\alpha}\,(H - C)^2}_{\text{bending moduluinduced variation}} + \underbrace{2\kappa\,(H - C)\frac{\partial C}{\partial\theta^\alpha}}_{\text{protein-induced variation}}$$
$$- \underbrace{\frac{\partial\kappa_G}{\partial\theta^\alpha}K}_{\text{Gaussian moduluinduced variation}} - \underbrace{\mathbf{f} \cdot \mathbf{a}_\alpha}_{\text{force induced variation}}, \quad (2.13)$$

In the absence of externally applied force $\mathbf{f}$ and for spatially homogeneous bending and Gaussian moduli, we recover the equations of motion for a heterogeneous membrane [47, 48].

$$\lambda_{,\alpha} = -\frac{\partial W}{\partial\theta^\alpha}|_{\exp} = 2\kappa(H - C)\frac{\partial C}{\partial\theta^\alpha}. \quad (2.14)$$

$$\kappa[\Delta(H - C) + 2(H - C)(H^2 + HC - K)] - 2\lambda H = p. \quad (2.15)$$

λ can be interpreted as the tension in a flat membrane [49, 50]. Furthermore, in the special case of zero spontaneous curvature and non-zero mean curvature, $\lambda = constant$ everywhere, see Eq. (2.13). This constant value of λ must be provided as an input parameter to solve the system of equations [50], and is widely interpreted to be surface tension in the literature [51]. A detailed interpretation of λ is given in [48].

Equations of motion in axisymmetric coordinates

Definitions

We define a surface of revolution (Figure 2.2)
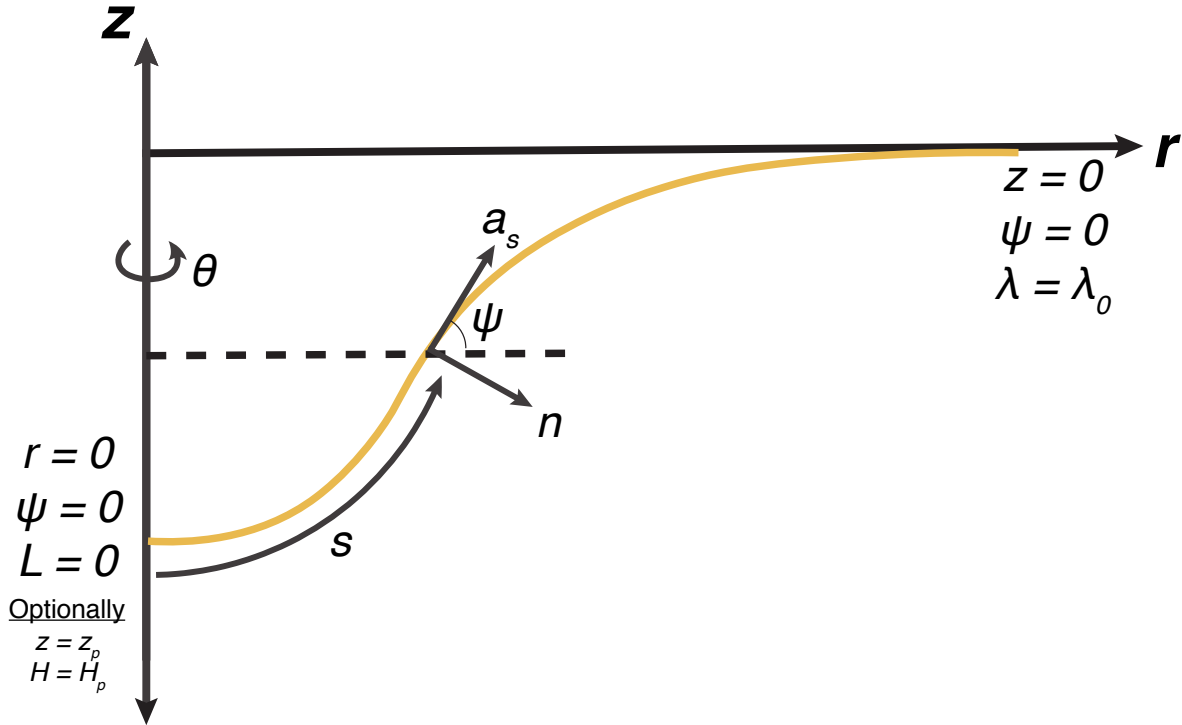
Figure 2.2: Schematic of the axisymmetric geometry adopted for the simulations as described in Section 2.2. The boundary conditions at the tip of the bud and the boundary of the patch were implemented as indicated. The optional boundary conditions (2.30) and (2.31) were used to obtain the value of applied force in actin-mediated inward-directed force (Figure 2.12B) and constriction force (Figure 2.12D) simulations, respectively (see Section 2.2).

$$\mathbf{r}\left(s,\theta\right) = r(s)\mathbf{e}_r\left(\theta\right) + z(s)\mathbf{k} \tag{2.16}$$

where s is the arc-length along the curve, $r(s)$ is the radius from axis of revolution, $z(s)$ is the elevation from a base plane and $(\mathbf{e}_r, \mathbf{e}_\theta, \mathbf{k})$ form the coordinate basis. Since $(r')^2 + (z')^2 = 1$, we can define an angle ψ such that

$$\mathbf{a}_s = \cos\psi\,\mathbf{e}_r + \sin\psi\,\mathbf{k}, \quad \mathbf{n} = -\sin\psi\,\mathbf{e}_r + \cos\psi\,\mathbf{k} \tag{2.17}$$

are the unit tangent and normal vectors, respectively, and

$$r'(s) = \cos\psi, \quad z'(s) = \sin\psi \tag{2.18}$$

parametrize the surface. The tangential (κ_ν) and transverse (κ_t) curvatures are given by

$$\kappa_\nu = \psi', \quad \kappa_t = r^{-1}\sin\psi \tag{2.19}$$

and the mean (H) and Gaussian (K) curvatures

$$H = \frac{1}{2}\left(\kappa_\nu + \kappa_t\right) \tag{2.20}$$

$$K = \kappa_\nu\kappa_t = H^2 - \left(H - r^{-1}\sin\psi\right)^2. \tag{2.21}$$

Rearranging Eq. (2.20) with Eq. (2.19) yields the differential equation for ψ,

$$r\psi'(s) = 2rH - \sin\psi. \tag{2.22}$$

Equilibrium equations

Let L be given by

$$L = \frac{1}{2\kappa}r\left(W_H\right)' = \frac{1}{\kappa}r\left[\kappa\left(H - C\right)\right]', \tag{2.23}$$

allowing us to obtain a first-order differential equation for the mean curvature,

$$H'(s) = r^{-1}L + C'(s) - \frac{\kappa'(s)}{\kappa}\left(H - C\right). \tag{2.24}$$

Using Eq. (2.23) in Eq. (2.12) we obtain

$$\Delta\left[\kappa\left(H - C\right)\right] = r^{-1}\left\{\left[\kappa\left(H - C\right)\right]'\right\}' = r^{-1}\left[\kappa L\right]' = r^{-1}\left(\kappa'L + \kappa L'\right). \tag{2.25}$$

Evaluating $2H\Delta\kappa_G - (\kappa_G)_{;\alpha\beta}\,b^{\alpha\beta}$ in the axisymmetric geometry we obtain

$$2H\Delta\kappa_G - (\kappa_G)_{;\alpha\beta}\, b^{\alpha\beta} = \kappa_G{}''r^{-1}\sin\psi + \kappa_G{}'r^{-1}\cos\psi\left(2H - r^{-1}\sin\psi\right). \tag{2.26}$$

Inserting Eq. (2.25) and (2.26) into Eq. (2.12) and rearranging we obtain a first-order differential equation for L,

$$r^{-1}L'(s) = \frac{p}{\kappa} + \frac{\mathbf{f}\cdot\mathbf{n}}{\kappa} + 2H\left[(H-C)^2 + \frac{\lambda}{\kappa}\right] - 2(H-C)\left[H^2 + \left(H - r^{-1}\sin\psi\right)^2\right]$$

$$- \frac{\kappa'(s)}{\kappa}r^{-1}L - \frac{\kappa_G{}''(s)}{\kappa}r^{-1}\sin\psi - \frac{\kappa_G{}'(s)}{\kappa}r^{-1}\cos\psi\left(2H - r^{-1}\sin\psi\right). \tag{2.27}$$

Finally, Eq. (2.13) becomes

$$\lambda'(s) = -\kappa'(s)\left(H-C\right)^2 + 2\kappa\left(H-C\right)C'(s) - \kappa_G{}'(s)K - \mathbf{f}\cdot\mathbf{a}_s. \tag{2.28}$$

The system of equations to be solved to obtain the shapes of the membrane are Eqs. (2.18), (2.22), (2.24), (2.27), and (2.28).

Boundary conditions

In order to solve this system of equations (Eqs. (2.18), (2.22), (2.24), (2.27), and (2.28)), we need to provide six boundary conditions. We consider an axisymmetric circular patch of membrane (see Figure 2.2). At the center of the patch, $s = 0^+$, we require: 1) the distance from the axis of symmetry be 0, 2) $\psi = 0$ to ensure continuous differentiability of the surface, and 3) $L = 0$ due to reflection symmetry. At the boundary of the patch, $s = S$, we require 1) that the membrane not lift off and therefore $Z = 0$, 2) $\psi = 0$ to ensure continuous differentiability with the flat surrounding membrane, and 3) λ is prescribed. These conditions can be summarized as

$$R\left(0^+\right) = 0, \quad L\left(0^+\right) = 0, \quad \psi\left(0^+\right) = 0, \tag{2.29a}$$

$$Z\left(S\right) = 0, \quad \psi\left(S\right) = 0, \quad \lambda\left(S\right) = \lambda_0. \tag{2.29b}$$

In cases relating to the actin-mediated force (Figure 2.12A), we prescribe the displacement of the of the tip, and calculate the force needed to maintain the prescribed displacement. I implemented this additional boundary condition as

$$Z\left(0^+\right) = Z_p. \tag{2.30}$$

Similarly, for actin-mediated constriction (Figure 2.12C), we prescribe the mean curvature at the bud tip and calculate the force required to maintain this curvature. This boundary condition is implemented as

$$H\left(0^+\right) = H_p. \tag{2.31}$$

Dimensionless variables

In order to perform the numerical computations, I non-dimensionalized the system by introducing two positive constants, R_0 and κ_0, and defining the following dimensionless variables.

$$t \equiv s/R_0, \quad x \equiv r/R_0, \quad y \equiv z/R_0, \quad h \equiv HR_0, \quad c \equiv CR_0, \quad l \equiv LR_0,$$
$$\widetilde{\lambda} \equiv \lambda R_0{}^2/\kappa_0, \quad \widetilde{p} \equiv pR_0{}^3/\kappa_0, \quad \widetilde{\mathbf{f}} \equiv \mathbf{f}R_0{}^3/\kappa_0, \quad \widetilde{\kappa} \equiv \kappa/\kappa_0, \quad g = KR_0{}^2, \quad \widetilde{\kappa_G} \equiv \kappa_G/\kappa_0. \tag{2.32}$$

In terms of Eq. (2.32), the system of equations, Eqs. (2.18), (2.22), (2.24), (2.27), and (2.28), become

$$\dot{x} = \cos\psi, \quad \dot{y} = \sin\psi, \quad x\dot{\psi} = 2xh - \sin\psi, \quad \dot{h} = x^{-1}l + \dot{c} - \frac{\dot{\widetilde{\kappa}}}{\widetilde{\kappa}}(h-c) \tag{2.33a}$$

$$x^{-1}\dot{l} = \frac{\widetilde{p}}{\widetilde{\kappa}} + \frac{\widetilde{\mathbf{f}}\cdot\mathbf{n}}{\widetilde{\kappa}} + 2h\left[(h-c)^2 + \frac{\widetilde{\lambda}}{\widetilde{\kappa}}\right] - 2(h-c)\left[h^2 + \left(h - x^{-1}\sin\psi\right)^2\right]$$
$$- \frac{\dot{\widetilde{\kappa}}}{\widetilde{\kappa}}x^{-1}l - \frac{\dot{\widetilde{\kappa_G}}}{\widetilde{\kappa}}x^{-1}\sin\psi - \frac{\dot{\widetilde{\kappa_G}}}{\widetilde{\kappa}}x^{-1}\cos\psi\left(2h - x^{-1}\sin\psi\right), \tag{2.33b}$$

$$\dot{\widetilde{\lambda}} = -\dot{\widetilde{\kappa}}(h-c)^2 + 2\widetilde{\kappa}(h-c)\dot{c} - \dot{\widetilde{\kappa_G}}g - \dot{\widetilde{\mathbf{f}}}\cdot\mathbf{a_s}. \tag{2.33c}$$

The boundary conditions, Eq. (2.29) become

$$x\left(0^+\right) = 0, \quad l\left(0^+\right) = 0, \quad \psi\left(0^+\right) = 0 \tag{2.34a}$$
$$\psi\left(T\right) = 0, \quad y\left(T\right) = 0, \quad \widetilde{\lambda}\left(T\right) = \widetilde{\lambda}_0, \tag{2.34b}$$

where $T = S/R_0$ is the total dimensionless arc-length. The boundary conditions imposed to solve for unknown applied force, Eqs. (2.30) and (2.31), become

$$y\left(0^+\right) = y_p, \quad h\left(0^+\right) = h_p. \tag{2.35}$$

Area dependence

Arc-length to area dependence

In axisymmetry there is a one-to-one correspondence between arc-length and area, which allows us to express the system of equations as a function of area instead of arc-length. This is because

$$a(s) = 2\pi\int_0^s r(t)\mathrm{d}t \quad\Longrightarrow\quad \frac{\mathrm{d}a}{\mathrm{d}s} = 2\pi r. \tag{2.36}$$

This method has the advantage of prescribing the total membrane area rather than the arc length as the simulation domain. Using Eq. (2.36), we convert Eqs. (2.18), (2.22), (2.24), (2.27), and (2.28) into

$$2\pi r\, r'(a) = \cos\psi, \quad 2\pi r\, z'(a) = \sin\psi, \quad 2\pi r^2 \psi'(a) = 2rH - \sin\psi, \tag{2.37a}$$

$$2\pi r^2 H'(a) = L + 2\pi r^2 C'(a) - 2\pi r^2 \frac{\kappa'(a)}{\kappa}(H - C) \tag{2.37b}$$

$$\begin{aligned}
2\pi L'(a) = {}& \frac{p}{\kappa} + \frac{\mathbf{f}\cdot\mathbf{n}}{\kappa} + 2H\left[(H-C)^2 + \frac{\lambda}{\kappa}\right] - 2(H-C)\left[H^2 + \left(H - r^{-1}\sin\psi\right)^2\right] \\
& - 2\pi\frac{\kappa'(a)}{\kappa}L - 4\pi^2 r\frac{\kappa_G{}''(a)}{\kappa}\sin\psi - 2\pi\frac{\kappa_G{}'(a)}{\kappa}\cos\psi\left(2H - r^{-1}\sin\psi\right)
\end{aligned}$$
$$\tag{2.37c}$$

$$2\pi r\lambda'(a) = -2\pi r\kappa'(a)(H-C)^2 + 4\pi r\kappa(H-C)C'(a) - 2\pi r\kappa_G{}'(a)K - \mathbf{f}\cdot\mathbf{a_s}, \tag{2.37d}$$

The boundary conditions, Eqs. (2.29) and (2.30) are remain unchanged except for the limits at which they are applied.

$$R\left(0^+\right) = 0, \quad L\left(0^+\right) = 0, \quad \psi\left(0^+\right) = 0, \tag{2.38a}$$

$$\psi\left(A\right) = 0, \quad Z\left(A\right) = 0, \quad \lambda\left(A\right) = \lambda_0, \tag{2.38b}$$

where $A = 2\pi\int_0^S r(t)\mathrm{d}t$ is the total area of the membrane patch. The displacement and mean curvature conditions are

$$Z\left(0^+\right) = Z_p, \quad H\left(0^+\right) = H_p. \tag{2.39}$$

Dimensionless variables

Using the two positive constants, R_0 and κ_0, we can define

$$\alpha \equiv \frac{a}{2\pi R_0{}^2}, \quad x \equiv r/R_0, \quad y \equiv z/R_0, \quad h \equiv HR_0, \quad c \equiv CR_0, \quad l \equiv LR_0,$$

$$\widetilde{\lambda} \equiv \lambda R_0{}^2/\kappa_0, \quad \widetilde{p} \equiv pR_0{}^3/\kappa_0, \quad \widetilde{\mathbf{f}} \equiv \mathbf{f}R_0{}^3/\kappa_0, \quad \widetilde{\kappa} \equiv \kappa/\kappa_0, \quad g = KR_0{}^2, \quad \widetilde{\kappa_G} \equiv \kappa_G/\kappa_0. \tag{2.40}$$

In terms of Eq. (2.40), the system of equations, Eq. (2.37), become

$$x\dot{x} = \cos\psi, \quad x\dot{y} = \sin\psi \quad x^2\dot{\psi} = 2xh - \sin\psi, \quad x^2\dot{h} = l + x^2\dot{c} - x^2\frac{\dot{\widetilde{\kappa}}}{\widetilde{\kappa}}(h-c) \tag{2.41a}$$

$$\dot{l} = \frac{\widetilde{p}}{\widetilde{\kappa}} + \frac{\widetilde{\mathbf{f}}\cdot\mathbf{n}}{\widetilde{\kappa}} + 2h\left[(h-c)^2 + \frac{\widetilde{\lambda}}{\widetilde{\kappa}}\right] - 2(h-c)\left[h^2 + \left(h - x^{-1}\sin\psi\right)^2\right]$$

$$-\frac{\dot{\widetilde{\kappa}}}{\widetilde{\kappa}}l - x\frac{\ddot{\widetilde{\kappa_G}}}{\widetilde{\kappa}}\sin\psi - \frac{\dot{\widetilde{\kappa_G}}}{\widetilde{\kappa}}\cos\psi\left(2h - x^{-1}\sin\psi\right) \tag{2.41b}$$

$$\dot{\widetilde{\lambda}} = -\dot{\widetilde{\kappa}}(h-c)^2 + 2\widetilde{\kappa}(h-c)\dot{c} - \dot{\widetilde{\kappa}_G}g - x^{-1}\widetilde{\mathbf{f}}\cdot\mathbf{a_s}, \tag{2.41c}$$

and the boundary conditions, Eq. (2.38) and Eq, (2.39), become

$$x\left(0^+\right) = 0, \quad l\left(0^+\right) = 0, \quad \psi\left(0^+\right) = 0 \tag{2.42a}$$

$$y\left(\alpha_{max}\right) = 0, \quad \psi\left(\alpha_{max}\right) = 0, \ \widetilde{\lambda}\left(\alpha_{max}\right) = \widetilde{\lambda}_0, \tag{2.42b}$$

$$y\left(0^+\right) = y_p \quad h\left(0^+\right) = h_p. \tag{2.42c}$$

where $\alpha_{max} = \frac{A}{2\pi R_0{}^2}$ is the total dimensionless membrane area.

2.3 Simulation Methods

Computations were performed using MATLAB® (Mathworks, Natick, MA) using the routine 'bvp4c', a boundary value problem solver.

- The membrane patch was initialized to be a flat disk with a radius of $R = 400\,\text{nm}$.

  - The exception to this was for the simulations involving the creation of the phase diagram, Figure 2.10. In this case, the initial radius of the disk was set such that the arc-length of the domain was twice that needed for a bud of radius $R = 1/C_0$, where C_0 is the spontaneous curvature of the coat.

- The mesh points on the domain were chosen such that they were (initially) equally spaced along the arc-length with a spacing of $0.5\,\text{nm}$. To obtain convergence, the solver was allowed to increase the number of mesh points by up to a factor of 100, with the final solution evaluated on the original mesh.

- Subsequently, the area (or arc-length) of the coat (with fixed spontaneous curvature) or the spontaneous curvature of the coat (with fixed coat area) were progressively increased, with each solution in this sequence used in the solver as the initial guess for the subsequent computation.
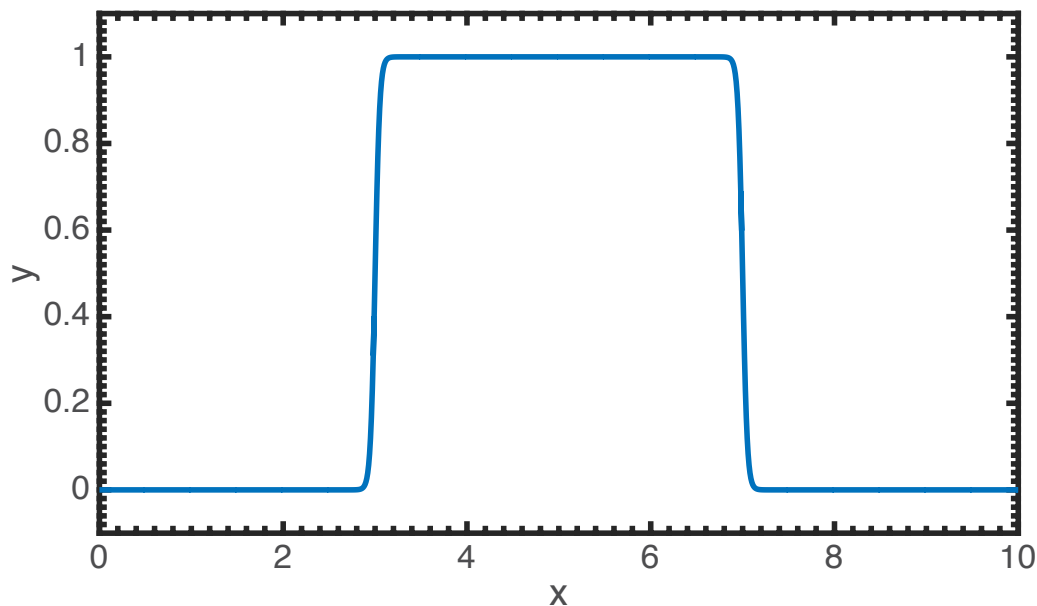
Figure 2.3: A hyperbolic tangent functional form was used to implement heterogeneous membrane properties. As an example, $y = \frac{1}{2} \left[\tanh(\gamma(x-3)) - \tanh(\gamma(x-7)) \right]$ is plotted with $\gamma = 20$. The sharp transitions were ideal for specifying the boundaries of the coated region or regions of applied force, and the smoothness of the tanh function allowed for straightforward implementation into the numerical scheme.

- To ensure sharp but smooth transitions at the boundaries of the coat and regions of applied force, these regions were specified using a hyperbolic tangent function (Figure 2.3).

- Simulations using the area-dependent equations (2.41): Figures 2.4, 2.11, 2.12, 2.13, 2.5, and 2.7

  - This was the preferred method for solving the ODEs as the area of the membrane domain is kept constant throughout the entire simulation, meaning that the boundaries of the domain stayed relatively more constant than in the arclength parametrization.

  - Despite this preference, we show in Figure 2.6 that the area of the membrane patch makes essentially no difference on the observed shapes of the membrane as long as the domain is sufficiently large, ensuring that either surface parametrization is valid and the solutions directly comparable.

  - Additionally, this parametrization is much more convenient in terms of directly specifying the coat area as well as the area of applied force. The applied force case is especially important as the applied force is really a force per unit area,

or effective pressure (see Eq. (2.12)), and the total magnitude of the force is obtained by integrating the force per unit area over the applied area.

- Simulations using the arc-length-dependent equations (2.33): Figures 2.8A and 2.10

  - Arc-length dependence was convenient for "coat-growing" simulations in the case of intermediate membrane tension as this formulation allowed for the instability to be smoothly traversed by simply increasing the arc-length coverage by the coat.

  - This is because it is possible for the arc-length covered by the coat to increase while the area coverage of the coat simultaneously decreases if the membrane becomes much more highly curved in the coated region.

  - This is exactly what happens for the so-called *unstable solutions* in Figure 2.8. These solutions cannot be accessed by the solver simply by adjusting the area of the coat; the next solution will always fall on one of the two *stable solution* branches. However, these unstable solutions are readily accessible simply by increasing the arc-length coverage of the coat, conveniently tracing out the entire solution space.

- Simulations with an applied force: Figures 2.12, 2.13, and 2.15

  - Rather than prescribing the force to obtain a displacement, we took advantage of the ability of the 'bvp4c' solver to calculate values of unknown parameters given an initial guess and an additional boundary condition.

  - For the inward directed forces (Figures 2.12B and 2.13A&B), this was achieved by specifying the z-position of the tip of the bud, Eq. (2.39). For simplicity, the force was applied uniformly across the coat.

  - For constricting forces (Figure 2.12D and 2.13C&D), this was achieved by specifying the mean curvature at the tip of the bud Eq. (2.39). For simplicity, the applied force was applied on a band of the membrane immediately bordering the coat.

2.4 Radius of a vesicle from energy minimization

We seek to identify an analytical expression for the radius - and hence area - of a spherical vesicle subject to a spontaneous curvature C_0 and membrane tension λ_0. From Helfrich [13] we have the bending energy of a sphere,

$$E_{\text{sphere}} = 4\pi\kappa \left(1 - RC_0\right)^2 . \tag{2.43}$$

The total energy, when factoring in the membrane tension is then

$$E_{\text{tot}} = 4\pi\kappa \left(1 - RC_0\right)^2 + 4\pi R^2 \lambda. \tag{2.44}$$

By taking $\partial E_{\text{tot}}/\partial R = 0$ and solving for the radius of the sphere we find

$$R = \frac{\kappa_0 C_0}{\lambda + \kappa_0 C_0^2}. \tag{2.45}$$

As a sanity check, when we set the membrane tension equal to zero $(\lambda = 0)$, we obtain

$$R(\lambda = 0) = \frac{1}{C_0}. \tag{2.46}$$

As expected, the radius matches the preferred radius of curvature.

Thus, the expected area of the sphere is just $A_{\text{sphere}} = 4\pi R^2$, which is a function of the bending modulus κ, spontaneous curvature C_0 and membrane tension λ_0. As seen in Figures 2.10B&C, this expression matches the area of vesicles obtained by increasing coat area for Ves > 1.

2.5 Tables

Table 2.1: Notation used in the model

Notation	Description	Units
W	Local energy per unit area	pN/nm
H	Mean curvature of the membrane	nm^{-1}
K	Gaussian curvature of the membrane	nm^{-2}
C	Prescribed spontaneous curvature	nm^{-1}
θ^α	Parameters describing the surface, $\alpha \in \{1,2\}$	
A_{coat}	Area covered by the coat	nm^2
$\mathbf{r}$	Position vector	
$\mathbf{n}$	Normal to the membrane surface	unit vector
$\mathbf{a}_\alpha$	Basis vectors describing the tangent plane, $\alpha \in \{1,2\}$	
γ	Lagrange multiplier for the incompressibility constraint	pN/nm
λ	Membrane tension, $-(W + \gamma)$	pN/nm
p	Pressure difference across the membrane	pN/nm^2
$\mathbf{f}$	Applied force per unit area	pN/nm^2
κ	Bending modulus	pN·nm
κ_G	Gaussian modulus	pN·nm
s	Arc-length	nm
S	Total arc-length of the membrane patch	nm
θ	Azimuthal angle	
r	Radial distance	nm
z	Elevation from base plane	nm
$\mathbf{e}_r$	Radial basis vector	unit vector
$\mathbf{e}_\theta$	Azimuthal basis vector	unit vector
$\mathbf{k}$	Altitudinal basis vector	unit vector
$\mathbf{a}_s$	Tangent to the membrane surface in the radial direction	unit vector
ψ	Angle between $\mathbf{e}_r$ and $\mathbf{a}_s$	

Table 2.2: Notation used in the model (continued)

Notation	Description	Units
κ_ν	Tangential curvature	nm^{-1}
κ_t	Transverse curvature	nm^{-1}
L	Shape equation variable	nm^{-1}
Z_p	Prescribed displacement at the pole	nm
H_p	Prescribed mean curvature at the pole	nm^{-1}
t	Dimensionless arc-length	
x	Dimensionless radial distance	
y	Dimensionless height	
h	Dimensionless mean curvature	
c	Dimensionless spontaneous curvature	
l	Dimensionless L	
$\widetilde{\lambda}$	Dimensionless membrane tension	
$\widetilde{p}$	Dimensionless transmembrane pressure	
$\widetilde{\mathbf{f}}$	Dimensionless force per unit area	
$\widetilde{\kappa}$	Dimensionless bending rigidity	
T	Total dimensionless arc-length	
y_p	Dimensionless prescribed pole displacement	
h_p	Dimensionless prescribed pole mean curvature	
a	Membrane area	nm^2
A	Total area of membrane patch	nm^2
α	Dimensionless membrane area	
α_{max}	Total dimensionless area	

Table 2.3: Parameters used in the model

Parameter	Significance	Value	Reference
λ_0	Membrane tension range	$10^{-4} - 1$ pN/nm	[16, 35, 52]
κ	Bending rigidity of bare membrane	320 pN $\cdot$ nm	[16]
C_0	Preferred curvature of coat	1/50 nm^{-1}	[12, 16]
R_0	Non-dimensionalization length	20 nm	

2.6 Results

Membrane tension controls bud formation by curvature-generating coats

In order to understand how membrane tension affects the morphology of a coated membrane, we performed two sets of calculations. In the first set, we studied the effect of varying coat area and membrane tension on membrane budding in the absence of external forces from the actin network. Simulations were performed by increasing the area of a curvature-generating coat at the center of an initially flat patch of membrane. We maintained the spontaneous curvature of the coat to be constant as $C_0 = 0.02\,\mathrm{nm}^{-1}$ in the coated region with a sharp transition at the boundary between the coated and bare membrane (implemented via hyperbolic tangent functions, Figure 2.3). The membrane tension was varied by setting the value of λ at the boundary of the membrane patch, which corresponds to the tension in the surrounding membrane reservoir.

High membrane tension ($0.2\,\mathrm{pN/nm}$) inhibits deformation of the membrane by the protein coat (Figure 2.4A, upper row). As the area of the coated region (A_{coat}) increases, the membrane remains nearly flat, and the size of the coated region can grow arbitrarily large without any substantial deformation (Figure 2.5). The spontaneous curvature of the coat is simply unable to overcome the additional resistance provided by the high membrane tension. In contrast, at low membrane tension ($0.002\,\mathrm{pN/nm}$), increasing the coat area causes a smooth evolution from a shallow to deep U-shape to a closed, Ω-shaped bud. (Figure 2.4A, lower row). We stopped the simulations when the membrane is within 5 nm of touching at the neck, at which point bilayer fusion resulting in vesicle scission is predicted to occur spontaneously [41, 53]. These morphological changes are similar to those observed in clathrin-mediated endocytosis [54] and do not depend on the size of the membrane patch (Figure 2.6).

Since increasing coat area alone could not overcome the tension effects of the membrane, we asked if increasing the spontaneous curvature of the coat overcomes tension-mediated resistance to deformation. To answer this question, we performed simulations in which the spontaneous curvature of the coat increases while the area covered by the coat remains constant at approximately the surface area of a typical clathrin coated vesicle, $A_{\mathrm{coat}} = 20,106\,\mathrm{nm}^2$[54]. As before, high membrane tension (Figure 2.4B, upper row) prevents deformation of the membrane by the coat. Even increasing the spontaneous curvature to a value of $0.04\,\mathrm{nm}^{-1}$, corresponding to a preferred radius of curvature of 25 nm and twice the value used the coat growing simulations, does not produce a closed bud (Figure 2.7). In the case of low membrane tension (Figure 2.4B, lower row), a progressive increase in the coat spontaneous curvature causes a smooth evolution from a shallow to deep U-shape to a closed, Ω-shaped bud. The similarity between the membrane morphologies in Figure 2.4A and 2.4B indicates that the interplay between spontaneous curvature, coat area, and membrane tension is a governs membrane budding.
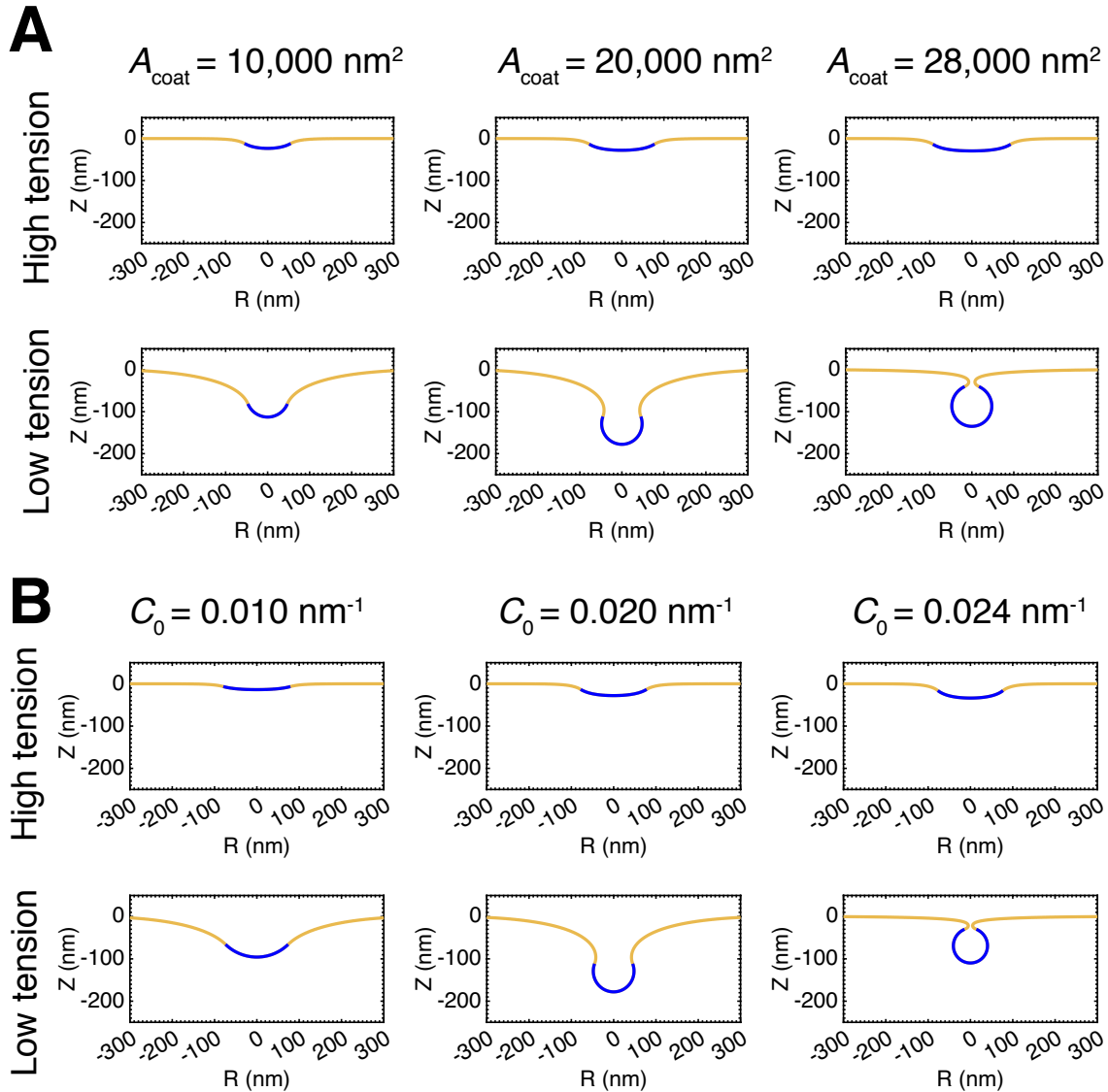
Figure 2.4: Membrane tension inhibits the ability of curvature generating coats to induce budding. **(A)** Profile views of membrane morphologies generated by simulations in which the area of a curvature-generating coat progressively increases, covering more of the bare membrane. The curvature-generating capability, or spontaneous curvature, of the coat is set at $C_0 = 0.02\,\text{nm}^{-1}$, corresponding to a preferred radius of curvature of 50 nm [12]. *Upper row:* High membrane tension, $\lambda_0 = 0.2\,\text{pN/nm}$. The membrane remains nearly flat as the area of the coat increases. *Lower row:* Low membrane tension, $\lambda_0 = 0.002\,\text{pN/nm}$. Addition of coat produces a smooth evolution from a flat membrane to a closed bud. **(B)** Membrane profiles for simulations with a constant coat area in which the spontaneous curvature of the coat progressively increases. The area of the coat is $A_{\text{coat}} = 20{,}106\,\text{nm}^2$. *Upper row:* High membrane tension, $\lambda_0 = 0.2\,\text{pN/nm}$. The membrane remains nearly flat with increasing spontaneous curvature. *Lower row:* Low membrane tension, $\lambda_0 = 0.002\,\text{pN/nm}$. Increasing the spontaneous curvature of the coat induces a smooth evolution from a flat membrane to a closed bud.
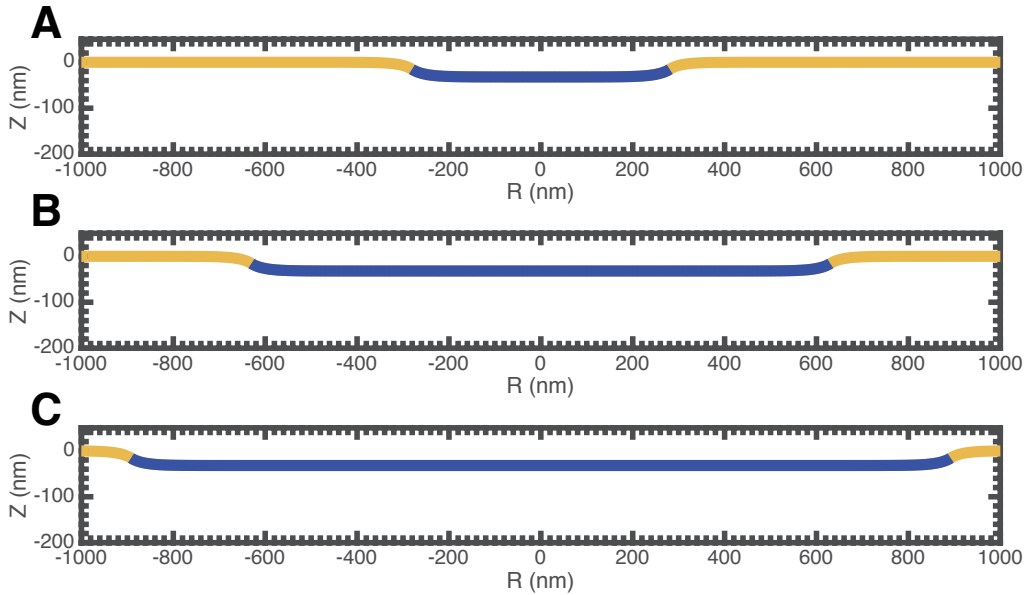
Figure 2.5: High membrane tension, $\lambda_0 = 0.2\,\mathrm{pN/nm}$, $C_0 = 0.02\,\mathrm{nm}^{-1}$. At high membrane tension, the coat can grow arbitrarily large without causing a substantial deformation of the membrane. **(A)** $A_{\mathrm{coat}} = 251{,}327\,\mathrm{nm}^2$, **(B)** $A_{\mathrm{coat}} = 1{,}256{,}637\,\mathrm{nm}^2$, **(C)** $A_{\mathrm{coat}} = 2{,}513{,}274\,\mathrm{nm}^2$

Transition from U- to Ω-shaped buds occurs via instability at intermediate membrane tensions

Experimentally measured membrane tensions in mammalian cells typically fall between the high and low tension regimes presented in Figure 2.4 [52]. At an intermediate, physiologically relevant value of membrane tension (0.02 pN/nm), increasing the area of the coat causes substantial deformation of the membrane (Figure 2.8A). However, the transition from an open to a closed bud is no longer smooth. Figure 2.8A shows a bud just before (dashed line) and after (solid line) a small amount of area is added to the coat. This small change in area causes the bud to "snap" closed to an Ω-shaped morphology. This situation is known as a *snapthrough instability*, and similar instabilities have been observed in other recent membrane modeling studies [27, 42]. We emphasize that these are two equilibrium shapes of the membrane, and the exact dynamical transition between these states (i.e. intermediate unstable shapes and timescale) is not modeled here.

To visualize why this abrupt transition should occur, Figure 2.8B plots the mean curvature at the tip of the bud as a function of the area of the coat. In comparison to the high and low membrane tension cases (Figure 2.9), there are two branches of equilibrium shapes of the membrane. The lower and upper branches represent "open" and "closed" morphologies of the bud, respectively. The marked solutions indicate the two morphologies depicted in Figure 2.8A. The open bud in Figure 2.8A is at the end of the open bud solution branch,
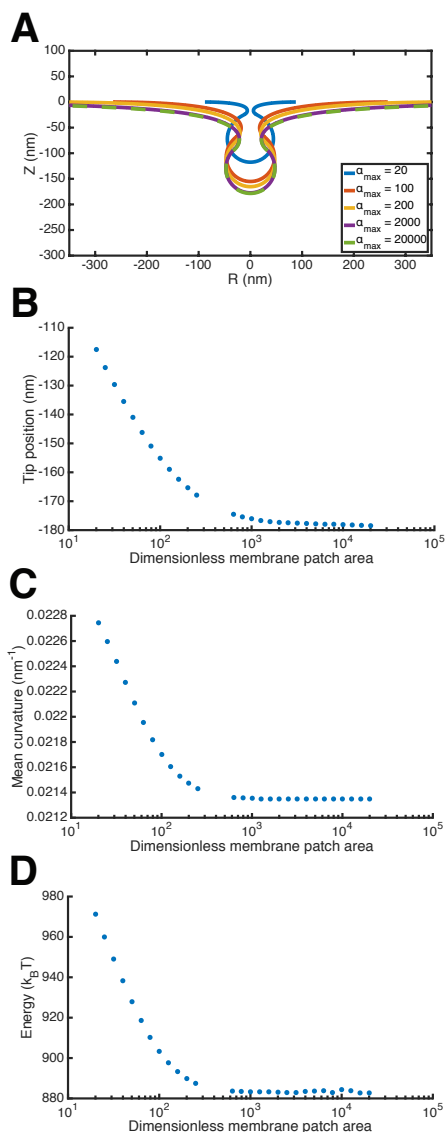
Figure 2.6: The size of the membrane patch has essentially no effect on the observed deformations of the membrane as long as it is sufficiently large. **(A)** Membrane profiles for identical coat areas and differing total patch areas. $\lambda_0 = 0.002\,\text{pN/nm}$, $A_{\text{coat}} = 25,133\,\text{nm}^2$, $C_0 = 0.02\,\text{nm}^{-1}$. The deformations are identical for very large membrane patches. **(B-D)** Z-position of the bud tip, mean curvature of the bud tip, and energy to deform the membrane, respectively, as a function of the dimensionless area of the membrane patch. The deformation of the membrane is sensitive to small membrane patches, but is essentially identical beyond $\alpha_{\text{max}} \approx 200$, particularly in terms of the tip mean curvature and the deformation energy.
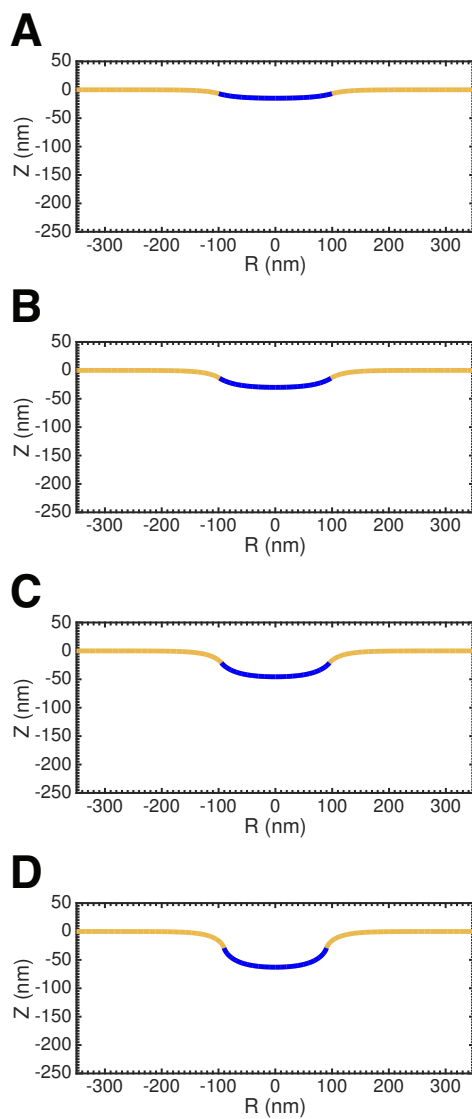
Figure 2.7: Increasing the spontaneous curvature of the coat at high membrane tensions does not produce closed buds. $A_{\text{coat}} = 31,416\,\text{nm}^2$, $\lambda_0 = 0.2\,\text{pN/nm}$. **(A)** $C_0 = 0.01\,\text{nm}^{-1}$ **(B)** $C_0 = 0.02\,\text{nm}^{-1}$ **(C)** $C_0 = 0.03\,\text{nm}^{-1}$ **(D)** $C_0 = 0.04\,\text{nm}^{-1}$
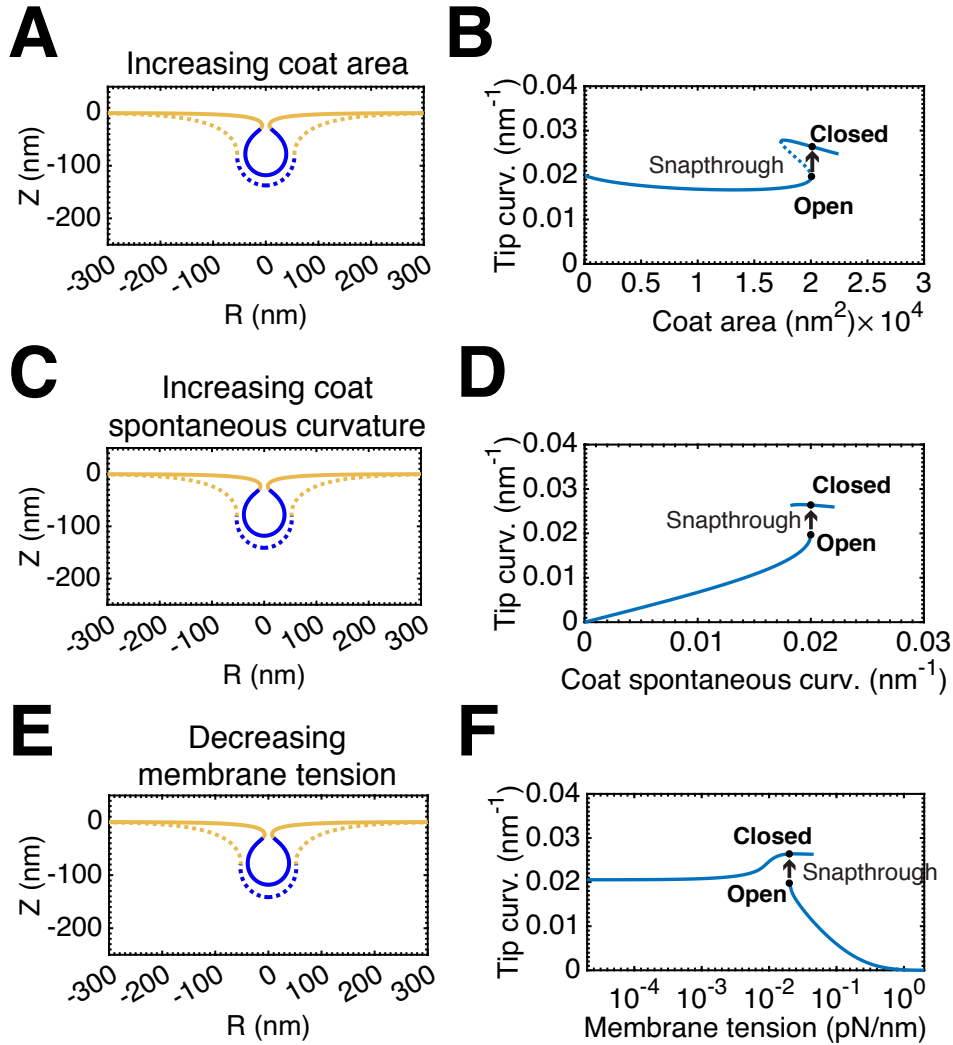
Figure 2.8: A snapthrough instability exists at intermediate, physiologically relevant [52], membrane tensions, $\lambda_0 = 0.02\,\text{pN/nm}$. **(A)** Membrane profiles showing bud morphology before (dashed line, $A_{\text{coat}} = 20{,}065\,\text{nm}^2$) and after (solid line, $A_{\text{coat}} = 20{,}105\,\text{nm}^2$) addition of a small amount of area to the coat, $C_0 = 0.02\,\text{nm}^{-1}$. **(B)** Mean curvature at the tip of the bud as a function of the coat area. There are two stable branches of solutions of the equilibrium membrane shape equations. The lower branch consists of open, U-shaped buds while the upper branch consists of closed, Ω-shaped buds. The dashed portion of the curve indicates "unstable" solutions that are not accessible by simply increasing and decreasing the area of the coat. The marked positions on the curve denote the membrane profiles shown in (A). The transition between these two shapes is a snapthrough instability, in which the bud "snaps" closed upon a small addition to area of the coat. **(C)** Bud morphologies before (dashed line) and after (solid line) a snapthrough instability with increasing spontaneous curvature, $A_{\text{coat}} = 20,106\,\text{nm}^2$, $C_0 = 0.02\text{nm}^2$. **(D)** Mean curvature at the tip of the bud as a function of the spontaneous curvature of the coat. **(E)** Bud morphology before (dashed line) and after (solid line) a snapthrough instability with decreasing membrane tension, $A_{\text{coat}} = 20,106\,\text{nm}^2$, $C_0 = 0.02\text{nm}^2$, $\lambda_0 = 0.02\,\text{pN/nm}$. **(F)** Mean curvature at the tip of the bud as a function of the membrane tension.

so any addition of small area to the coat necessitates that the membrane adopt a closed morphology.
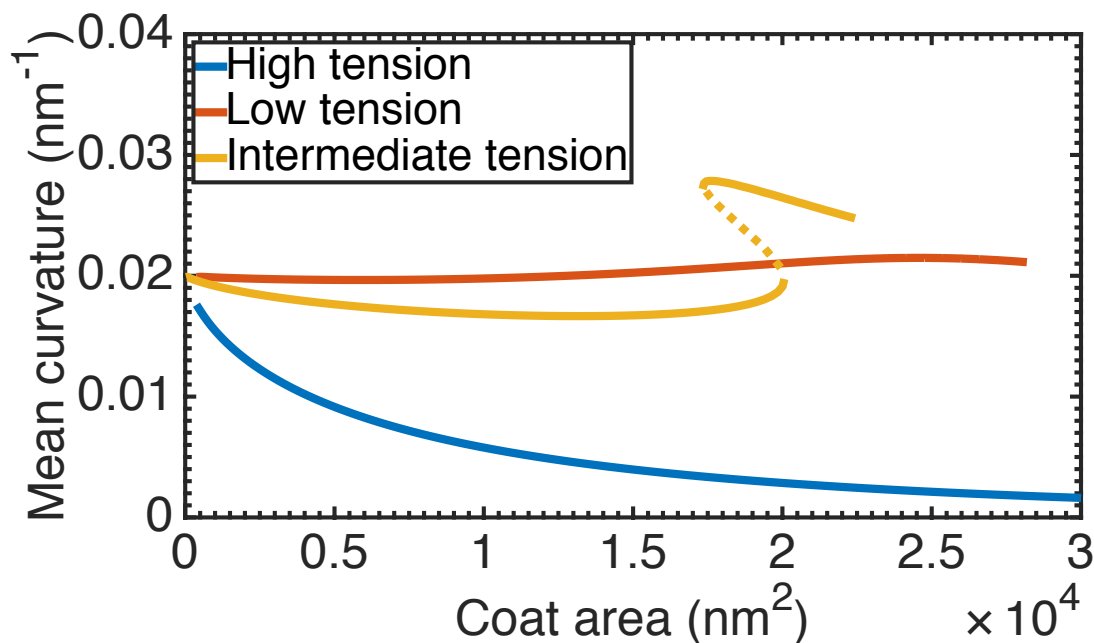
Figure 2.9: Mean curvature at the bud tip as a function of the area of the coat for the three different membrane tension cases. High membrane tension, $\lambda_0 = 0.2\,\text{pN/nm}$: The mean curvature at the bud tip drops to nearly $0\,\text{nm}^{-1}$ as the size of the coat increases and the membrane stays essentially flat at the center of the patch (Figure 2.4A-C). Low membrane tension, $\lambda_0 = 0.002\,\text{pN/nm}$: The mean curvature at the bud tip remains at approximately $0.02\,\text{nm}^{-1}$ as the size of the coat increases and the membrane adopts the spontaneous curvature of the coat (Figure 2.4D-F). Intermediate membrane tension, $\lambda_0 = 0.002\,\text{pN/nm}$: Reproduced from Figure 2.8B. The mean curvature at the bud tip is lower for open buds (lower solution branch) relative to the low tension case, indicating that tension is inhibiting curvature generation by the coat. In contrast, the curvature is higher in the closed buds (upper solution branch) relative to closed buds in the low tension case, showing that membrane tension serves to shrink the size (and hence increase the curvature) of closed buds.

This instability is also present for situations with increasing coat spontaneous curvature and constant coat area. Figure 2.8C shows membrane profiles before (dashed line) and after (solid line) a snapthrough transition triggered by an increase in spontaneous curvature. Figure 2.8D plots the mean curvature at the bud tip as a function of the coat spontaneous curvature. Similarly to Figure 2.8B, we observe that there are two branches of equilibrium membrane shapes.

Additionally, this instability is encountered when membrane tension is varied and the coat area and spontaneous curvature are maintained constant. Figure 2.8E shows membrane profiles before (dashed line) and after (solid line) a snapthrough transition triggered by a decrease in membrane tension. In Figure 2.8F we again see two solution branches in the plot

of mean curvature at the tip as a function of membrane tension indicating a discontinuous transition between open and closed buds as tension is varied.

The instability exists over a range of membrane tensions, coat areas, and spontaneous curvatures
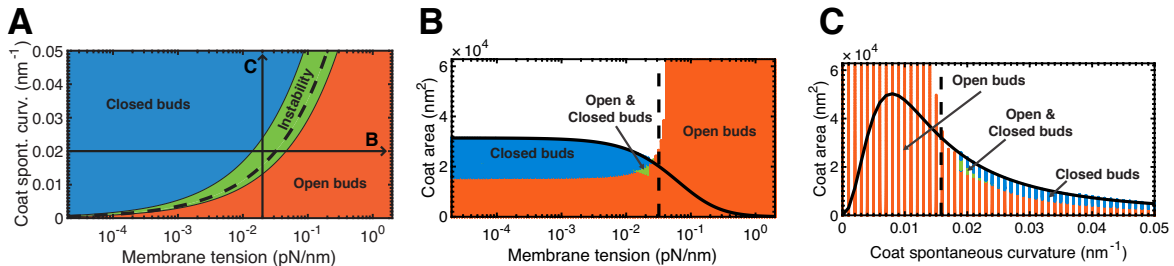
Figure 2.10: Bud morphology depends on bending rigidity, membrane tension, spontaneous curvature, and coat area. **(A)** Coat spontaneous curvature (C_0) vs. membrane tension (λ_0) phase diagram. The regions of the diagram are color coded according to the final shape of the membrane for coat "growing" simulations performed with the specified values for edge membrane tension and coat spontaneous curvature. Blue denotes closed, Ω-buds, Red denotes open, U-shaped pits, and Green are situations in which closed buds are obtained via a snapthrough transition. The snapthrough solutions cluster about the dashed line, Ves = 1, which separates the "high" and "low" membrane tension regimes (see main text). The lines labeled **B** & **C**, respectively, indicate the phase diagrams at right. **(B)** Coat area vs. membrane tension phase diagram, $C_0 = 0.02\,\mathrm{nm}^{-1}$. Blue denotes closed buds, red denotes open buds and green denotes parameters which have both open and closed bud solutions. The dashed line, Ves = 1, marks the transition from "low" to "high" membrane tension. The solid line represents the theoretical area of a sphere that minimizes the Helfrich energy at the specified membrane tension (see SI Appendix, Section 2.4). **(C)** Coat area vs. spontaneous curvature phase diagram, $\lambda_0 = 0.02\,\mathrm{pN/nm}$. The dashed line, Ves = 1, marks the transition between spontaneous curvatures that are capable and incapable of overcoming the membrane tension to form a closed bud. The solid line represents the theoretical area of a sphere that minimizes the Helfrich energy at the specified spontaneous curvature (see SI Appendix, Section 2.4).

Over what ranges of tension and spontaneous curvature does this snapthrough transition occur? First, to understand the nature of the transition between low and high membrane tension regimes, we performed simulations over several orders of magnitude of the membrane tension (10^{-4} to 1 pN/nm), encompassing the entire range of measured physiological tensions [52], as well as over a range of spontaneous curvatures of the coat (0 to 0.05 nm^{-1}), corresponding to preferred radii of curvature from 20 nm and up. Based on the results, we constructed a phase diagram summarizing the observed morphologies (Figure 2.10A). The blue region denotes a smooth evolution to a closed bud, the red region represents a failure to form a closed bud, and green region indicates a snapthrough transition from an open to a closed bud. This phase diagram clearly shows that the distinction between "low" and "high" membrane tension conditions depends on the magnitude of the spontaneous curvature of the coat.

These results can be understood by comparing the spontaneous curvature of the coat to the membrane tension and bending rigidity by studying the dimensionless quantity, $\text{Ves} = \frac{C_0}{2}\sqrt{\frac{\kappa}{\lambda}}$, hereafter termed the *vesiculation number*. The dashed line in Figure 2.10A corresponds to Ves = 1, which bisects the low (Ves > 1) and high tension (Ves < 1) results. The snapthrough results cluster about this line, marking the transition region between the high and low tension cases. Importantly, this demonstrates that the preferred radius of curvature of the coat, $1/C_0$, must be smaller than the "natural" length scale of the membrane, $\frac{1}{2}\sqrt{\kappa/\lambda}$ [27], for the coat to produce a closed bud in the absence of other mechanisms of curvature generation.

To study how the coat area affects the budding transition at a fixed spontaneous curvature, we varied spontaneous curvature and membrane tension for a fixed value of $C_0 = 0.02\,\text{nm}^{-1}$ (Figure 2.10B). We also varied coat area against coat spontaneous curvature for a fixed value of $\lambda_0 = 0.02\,\text{pN/nm}$ (Figure 2.10C). For the sake of presentation, we here define Ω-shaped buds as any in which there is any overhang on the membrane contour ($\psi > \pi/2$, Figure 2.2), and U-shaped buds have no overhang ($\psi <= \pi/2$). Blue denotes Ω-shaped buds, the red region represents U-shaped buds, and green region indicates coexisting solutions of U- and Ω-shaped buds. In each plot, the dashed line represents Ves = 1, and the solid line is the area of a sphere with the given spontaneous curvature and membrane tension that would minimize the free energy (see SI Appendix, Section 2.4). We see that for Ves << 1 (high tension, low spontaneous curvature) the coat area can be increased arbitrarily high without formation of an Ω- shaped bud. Conversely, for Ves >> 1 (low tension, high spontaneous curvature), buds progress smoothly progress from U- to Ω-shaped buds as coat area is increased. Additionally, the final area of the coat before termination of the simulation closely aligns with the predicted area from energy minimization (see SI Appendix, Section 2.4).

Increased coat rigidity smooths out the transition from open to closed buds

What properties of the membrane could be varied to overcome the instability at intermediate membrane tensions? Until now, we have taken the coat to have the same bending modulus as the bare membrane. The bending rigidity of clathrin-coated vesicles was estimated to be $\kappa_{\text{CCV}} = 285\,k_{\text{B}}T = 2280\,\text{pN}\cdot\text{nm}$ from atomic force microscopy measurements [55]. Increasing the rigidity of the coated region to be $\kappa_{\text{coat}} = 2400\,\text{pN}\cdot\text{nm}$, 7.5$\times$ the rigidity of the bare membrane $\kappa_{\text{coat}} = 320\,\text{pN}\cdot\text{nm}$, we conducted simulations at intermediate membrane tension ($\lambda_0 = 0.02\,\text{pN/nm}$) with increasing coat area at constant spontaneous curvature (Figure 2.11A) and with increasing spontaneous curvature at constant area (Figure 2.11C). Comparing the plots of bud tip mean curvature as a function of coat area Figure (2.11B) and spontaneous curvature (Figure 2.11D), to those of the earlier simulations (Figures 2.8B and 2.8D, respectively), we see that there is now only a single branch of membrane shapes, indicating a smooth evolution from open, U-shaped buds to closed, Ω-shaped buds. We can understand these results by considering the vesiculation number. By increasing κ_{coat}, we are
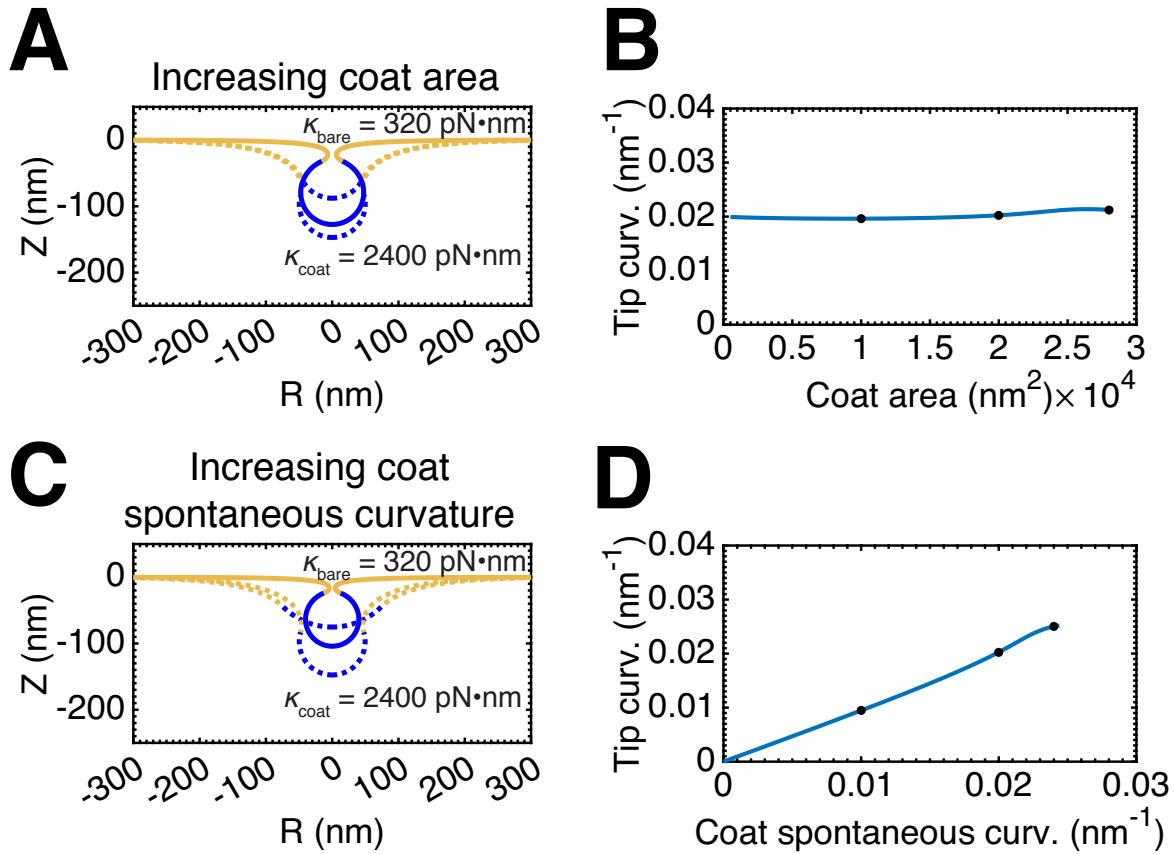
Figure 2.11: The snapthrough instability at physiological tension, $\lambda_0 = 0.02\,\mathrm{pN/nm}$, is abolished when the bending rigidity of the coat is increased relative to the bare membrane, $\kappa_{\mathrm{bare}} = 320\,\mathrm{pN \cdot nm}$, $\kappa_{\mathrm{coat}} = 2400\,\mathrm{pN \cdot nm}$. **(A)** Membrane profiles showing a smooth progression of bud morphologies as the area of the coat is increased ($A_{\mathrm{coat}} = 10,000\,\mathrm{nm}^2$, $20,000\,\mathrm{nm}^2$, $28,000\,\mathrm{nm}^2$), $C_0 = 0.02\,\mathrm{nm}^{-1}$. **(B)** Mean curvature at the bud tip as a function of the area of the coat. The marked positions denote the membrane profiles shown in (A). There is now only a single branch of solutions (as compared to Figure 2.8B), indicating a smooth evolution from a flat membrane to a closed bud. **(C)** Membrane profiles showing a smooth progression of bud morphologies as spontaneous curvature of the coat is increased ($C_0 = 0.01\mathrm{nm}^{-1}, 0.02\mathrm{nm}^{-1}, 0.024\mathrm{nm}^{-1}$), $A_{\mathrm{coat}} = 20,106\,\mathrm{nm}^2$. **(D)** Mean curvature at the bud tip as a function of the spontaneous curvature of the coat showing a single branch of solutions (compare to Figure 2.8D).

increasing the value of the vesiculation number and are in effect shifting the phase space of bud morphologies toward the low tension regime.

Force from actin polymerization can mediate the transition from a U- to Ω-shaped bud

What other mechanisms of force generation enable the cell to avoid the instability? Experiments have demonstrated that CME is severely affected by a combination of elevated tension and actin inhibition [5, 32]. To examine whether a force from actin polymerization is sufficient to induce a transition from open to closed bud morphologies, we modeled the force from actin polymerization in two orientations since the ultrastructure of the actin cytoskeleton at CME sites in live cells, and hence the exact orientation of the applied force, is currently unknown.

In the first candidate orientation, illustrated schematically in Figure 2.12A, actin polymerizes in a ring at the base of the pit with the network attached to the coat (via the actin-binding coat proteins Hip1R in mammals and its homologue Sla2 in yeast [56]). This geometric arrangement serves to redirect the typical compressive force from actin polymerization [57–59] into a net inward force on the bud and an outward force on the ring at the base of the invagination. This is analogous to the force from actin polymerization in yeast CME [31]. In the calculations, we take the force intensity to be homogeneously applied to the coated region, and the force intensity at the base is set such that the net applied force on the membrane integrates to zero. We find that an applied inward force of 15 pN on the bud is sufficient to drive the membrane from an open to closed configuration (Figure 2.12B). This force is well within the capability of a polymerizing branched actin network [60].

In the second orientation, actin assembles in a collar at the base, directly providing a constricting force (Figure 2.12C), as suggested by the results of Collins et al. [61]. In the calculations, we take this force intensity to be oriented perpendicular to the membrane and applied homogeneously to a region immediately adjacent to the coat. This orientation produces a small vertical force on the membrane that is implicitly balanced by a force at the boundary of the domain through the boundary condition $Z = 0$ nm. This counter force could easily be provided by the attachment of the underlying actin cortex to the plasma membrane [62]. Application of this constriction force is also sufficient to induce a smooth transition from U- to Ω-shaped buds with < 1 pN of applied force (Figure 2.12D).

A combination of increased coat rigidity and actin polymerization ensures robust vesiculation at high membrane tension

Since both increased coat rigidity and force from actin polymerization are sufficient to induce a smooth transition from open to closed buds at intermediate tension, we asked whether these prescriptions alone or in combination are sufficient to overcome high membrane tension to produce closed buds. In Figure 2.13A, we see that application of the inward directed
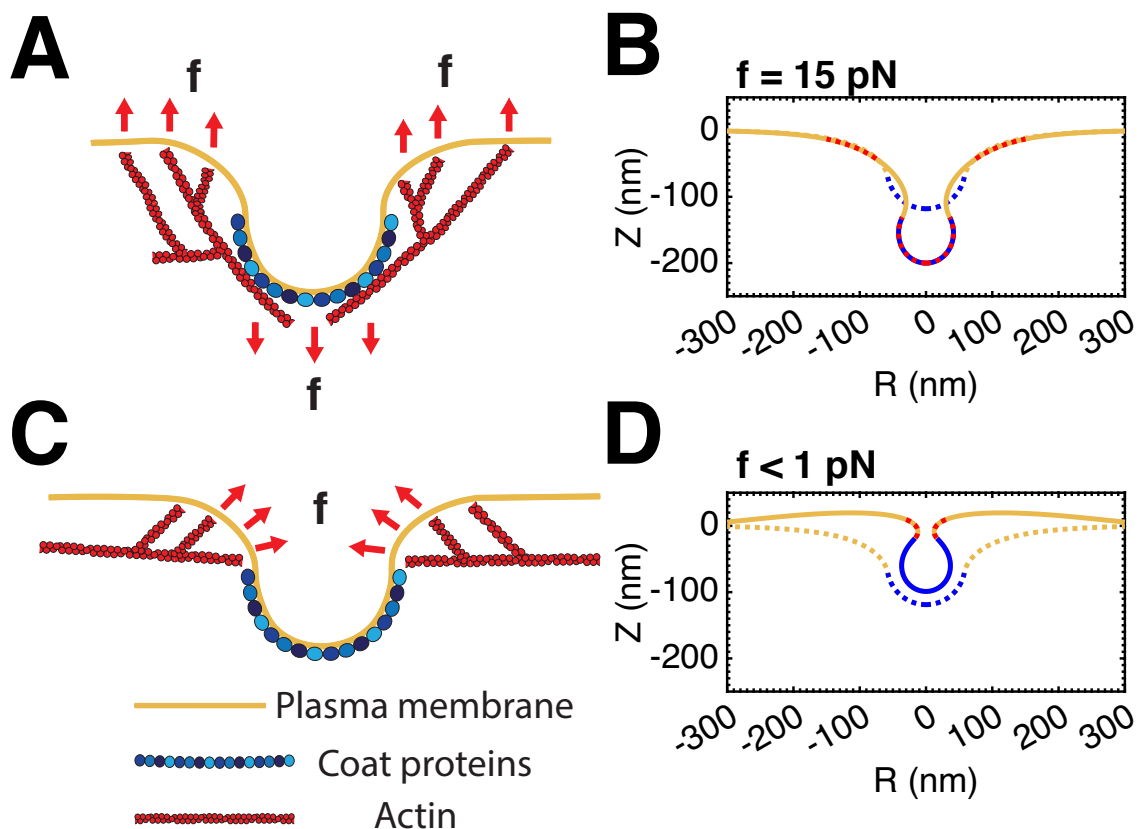
Figure 2.12: A force from actin assembly can mediate the transition from a U- to Ω-shaped bud, avoiding the instability at intermediate membrane tension, $\lambda_0 = 0.02\,\mathrm{pN/nm}$. Two orientations of the actin force were chosen based on experimental evidence from yeast [31] and mammalian [61] cells. **(A)** Schematic depicting actin polymerization in a ring at the base of the pit with the network attached to the coat, causing a net inward force on the bud. **(B)** At constant coat area, $A_{\mathrm{coat}} = 17,593\,\mathrm{nm}^2$, and spontaneous curvature, $C_0 = 0.02\,\mathrm{nm}^{-1}$, a force (red dash) adjacent to the coat drives the shape transition from a U-shaped (dashed line) to Ω-shaped bud (solid line). The force intensity was homogeneously applied to the entire coat, and the force intensity at the base of the pit was set such that the total force on the membrane integrates to zero. The final applied inward force on the bud was $\mathbf{f} = 15\,\mathrm{pN}$, well within the capability of a polymerizing actin network [60]. **(C)** Schematic depicting actin assembly in a collar at the base, directly providing a constricting force. [61] **(D)** A constricting force (red dash) localized to the coat drives the shape transition from a U-shaped (dashed line) to Ω-shaped bud (solid line), $A_{\mathrm{coat}} = 17,593\,\mathrm{nm}^2$, $C_0 = 0.02\,\mathrm{nm}^{-1}$. The force intensity was homogeneously applied perpendicular to the membrane to an area of $5,027\,\mathrm{nm}^2$ immediately adjacent to the coated region. The final applied force on the membrane was $\mathbf{f} < 1\,\mathrm{pN}$.

force (as in Figure 2.12A) causes the membrane to deform from its initially flat morphology (dashed line) to a tubulated morphology (solid line). This final morphology is not especially reminiscent of CME, and the force required is now 60 pN which would require several dozen free actin filament plus ends, which may not be realistic for one endocytic site. Increasing the bending rigidity of the coat alone is also insufficient to produce a closed bud (Figure 2.13B, dashed line). However, this increased rigidity in combination with force from actin polymerization is sufficient to induce a transition to an Ω-shaped bud (solid line). Increasing membrane rigidity reduces the magnitude of the applied force by a factor of three to 20 pN, which is more biologically reasonable. In Figure 2.13C , we see that application of the constricting force (as in Figure 2.12C) is sufficient to induce a transition to a closed bud (solid line) from the initial flat morphology (dashed line). However, the magnitude of the applied force is now 160 pN, which is unrealistically high given the small area to which the force must be applied. Instead, by increasing the rigidity of the coat in combination with this actin force, we again obtain a closed bud (Figure 2.13D), but now the required force has been reduced by an order of magnitude to 16 pN.

2.7 Discussion

In this study, we have investigated the role of membrane tension in governing the morphological landscape of CME and found that a combination of membrane tension and protein-induced spontaneous curvature governs the morphology of the endocytic pit (Figures 2.4). Additionally, we found that at intermediate membrane tensions, the bud must go through a snapthrough to go from an open to closed configuration (Figure 2.8). A key result from this work is that the vesiculation number can be used to identify the regimes of tension and curvature-mediated effects that separate the closed and open bud morphologies (Figure 2.10). Finally, we found that a modeling force generated by actin polymerization in CME can mediate the transition between open and closed buds at physiologically relevant membrane tensions (Figure 2.12). We believe that these results can explain and provide insight into the observations of a number of recent experimental studies.

Boulant et al. [5] found that hypoosmotic shock and treatment with jasplakinolide (an actin stabilizing drug) has a severe inhibitory effect on CME in polarized MDCK and BSC-1 cells, while treatment with jasplakinolide alone did not affect CME dynamics. In light of our findings, it probable that the high tension induced by hypoosmotic shock resulted in a regime where the coat alone is insufficient to produce closed buds. The observed overabundance of U-shaped, presumably stalled, pits is consistent with a situation in which the membrane tension is in the snapthrough or high tension regime and coat assembly is unable to deform the membrane into a closed bud shape. Thus, under conditions of hypoosmotic shock it seems that a force exerted by the actin cytoskeleton, as in Figure 2.12, is necessary form a closed bud.

Saleem et al [22] used micropipette experiments to control the tension in the membrane of giant unilamellar vesicles (GUVs) to which they added purified coat components. We

Figure 2.13: A combination of increased coat rigidity and force from actin polymerization ensures robust vesiculation, even at high membrane tension, $\lambda_0 = 0.2\,\mathrm{pN/nm}$, $C_0 = 0.02\,\mathrm{nm}^{-1}$. **(A)** Application of the inward directed actin force (as in Figure 2.12A) induces tubulation, but not vesiculation, at high tension. **(B)** Increasing the stiffness of the coat alone is insufficient to overcome high membrane tension (dashed line). However, increasing the coat stiffness enables the applied force to induce vesiculation and decreases the magnitude of the force required by a factor of 3. **(C)** Application of the constricting actin force (as in Figure 2.12C) is sufficient to induce vesiculation, even at high tension. The magnitude of the applied force required is likely unrealistically high in a biologically relevant setting. **(D)** Increasing the coat stiffness decreases the force required to induce vesiculation by an order of magnitude.

calculated the vesiculation number for the membrane tensions ($\approx 0.5 - 3\,\mathrm{pN/nm}$) set by micropipette aspiration to be less than 1 over a wide range of spontaneous curvatures, indicating a high membrane tension regime in their set up. Thus, our model is consistent with their observations of shallow buds observed in isotonic conditions. One result that our model cannot explain is the lack of any clathrin assembly observed under hypotonic conditions. It is possible that at extremely high membrane tensions the coat is simply unable to stay bound to the membrane at the extremely flat morphology that would be expected.

Avinoam et al. found that the size of the coat does not change substantially during membrane deformation in CME [54]. This is in contrast to the canonical view that the clathrin coat should directly impose its preferred curvature on the underlying membrane [8]. There are two possible explanations for this observation in the context of our study. One is
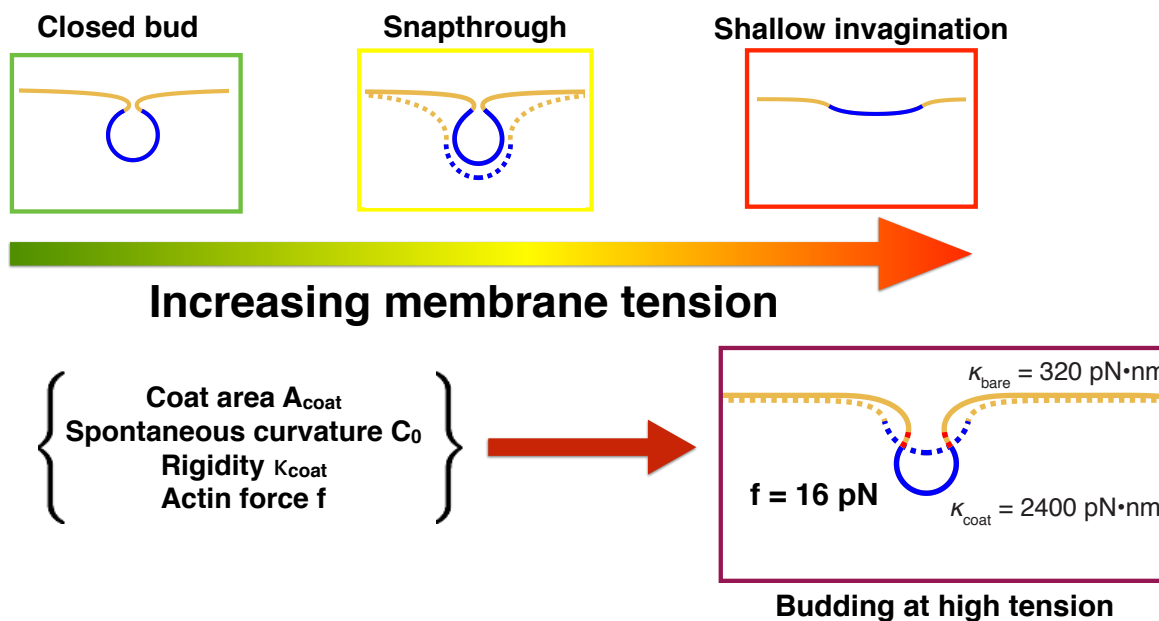
Figure 2.14: Design principles for robust vesiculation. The rigidity of the plasma membrane as well as the membrane tension resist budding by curvature-generating coats. In the low tension regime, as defined by the vesiculation number, increasing the coat area or spontaneous curvature is sufficient to induce a smooth e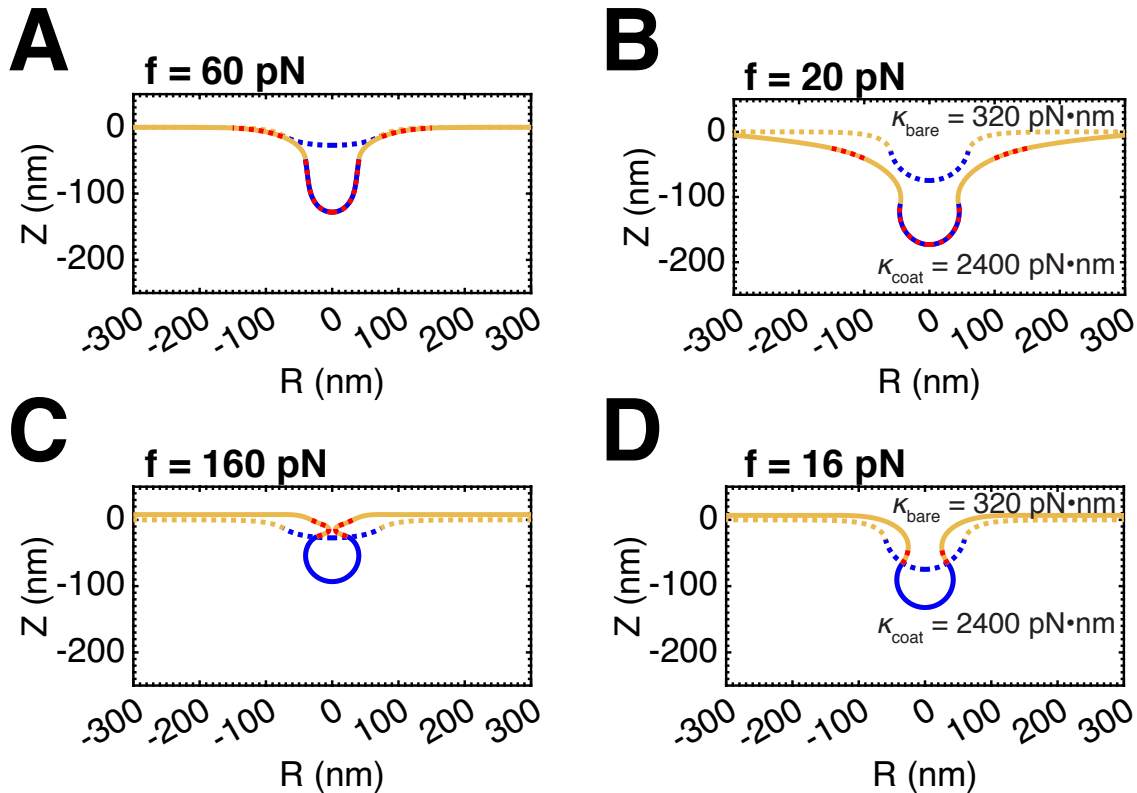volution from a flat membrane to a closed bud. A combination of increased coat rigidity and force from actin polymerization is necessary to ensure robust vesiculation in the high membrane tension regime.

that the membrane tension is too high for the coat to deform the membrane, so that other mechanisms of curvature generation (e.g. actin polymerization or BAR domain-induced curvature) are necessary to remodel the membrane. The second is that the coat undergoes a "maturation" process that progressively increases its spontaneous curvature, and hence its capability to bend the membrane, as in Figure 2.4B. The observation that actin inhibition causes substantial defects in CME in this cell type [32] is consistent with the hypothesis that the membrane tension could be elevated in this cell type, though this would need to be confirmed experimentally. Thus, it is possible that the observation that the size of the clathrin coat is constant during the budding process might be specific to SK-MEL-2 cells and in particular on the typical membrane tension of this cell line.

Our results also build on previous models that have been used to study CME. We have shown here that membrane deformation at high tension can be achieved by coupling increased coat rigidity and actin-mediated forces (Figure 2.13). Walani et al. also explored budding at high tension and predicted that an actin-force-driven snapthrough instability could drive scission in yeast CME [42]. However, this instability is a consequence of the exact implementation of the actin force (Figure 2.15), and so its physiological relevance is unclear.

Other models have assumed that the proteins exert a spherical cap and a line tension

A

B

C

D
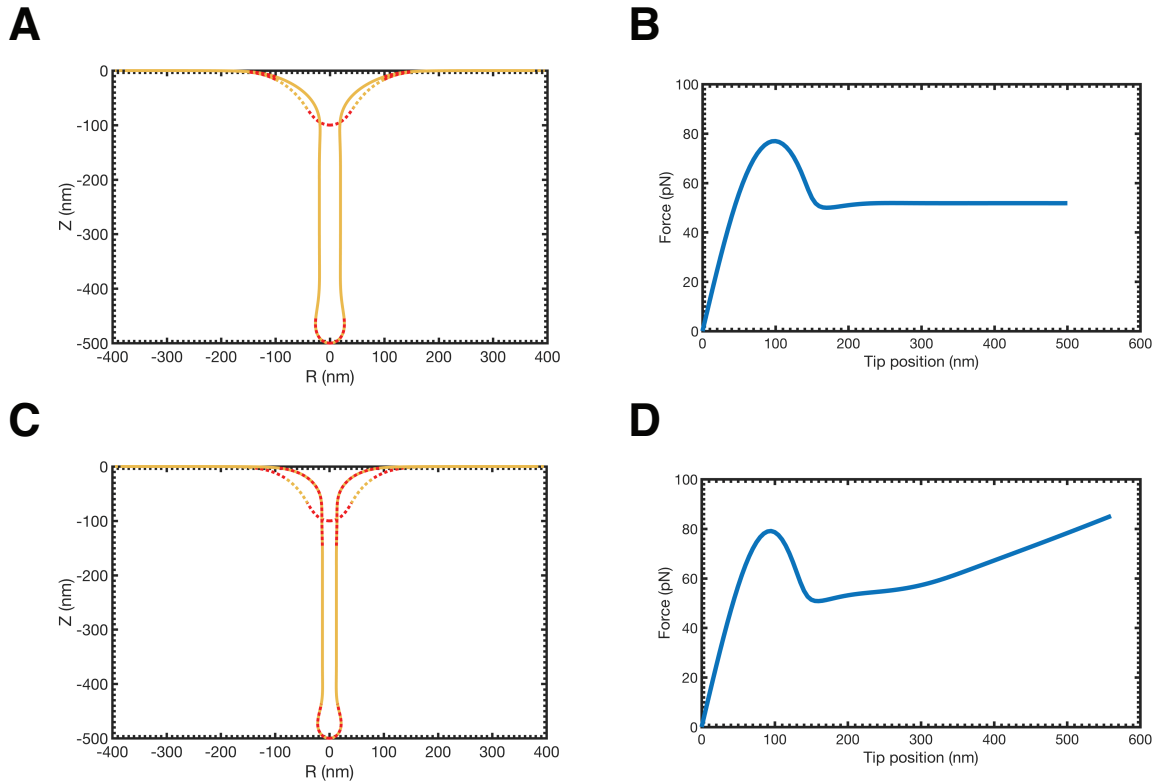
Figure 2.15: Comparison of actin ring forces as implemented in this study and by Walani et al. [42], $\lambda_0 = 0.2\,\mathrm{pN/nm}$. **(A)** Membrane profiles showing morphology before (dashed line, $Z_p = -100\,\mathrm{nm}$) and after (solid line, $Z_p = -500\,\mathrm{nm}$) tubulation with constant inner and outer radii ($R_{\mathrm{inner}} = 100\,\mathrm{nm}$ and $R_{\mathrm{outer}} = 150\,\mathrm{nm}$) for the ring of upward directed force at the base of the invagination. This implementation of the actin force was used in Figures 2.12B and 2.13A&B. **(B)** Applied force as a function of the tip displacement. Force initially increases with increasing depth of the invagination, but remains constant after tubulation. This behavior is also observed in the absence of a ring force [42, 51]. **(C)** Membrane morphology before (dashed line, $Z_p = -100\,\mathrm{nm}$) and after (solid line, $Z_p = -500\,\mathrm{nm}$) tubulation. The ring force is applied such that it is always applied between $A_{\mathrm{inner}} = 31,416\,\mathrm{nm}^2$ $A_{\mathrm{outer}} = 70,686\,\mathrm{nm}^2$ in the area-dependent parametrization (Section 2.2). Rather than being fixed at a ring with inner and outer radii$R_{\mathrm{inner}} = 100\,\mathrm{nm}$ and $R_{\mathrm{outer}} = 150\,\mathrm{nm}$, the ring tracks the same area of the membrane as it is pulled into the tube. The net effect of this is to limit the amount of membrane that can enter the tube. We believe that the counter force in Walani et al. [42] was implemented in this manner. **(D)** Applied force as a function of the tip displacement. Force initially increases with increasing depth of the invagination, decreases upon tubulation, and subsequently increases as the length of the tube increases, leading to a snapthrough instability with increasing force, as found by Walani et al. This instability is occurs independent of the membrane tension or the presence of a curvature-generating coat (data not shown). The physiological relevance of this implementation of the actin force and the snapthrough instability that results is unclear for two reasons: 1) It is unclear whether actin or other proteins at the base of the invagination would limit the ability of the membrane to flow into the invagination as implicitly assumed by this implementation, and 2) Because force from actin polymerization is a reaction force established through a Brownian ratchet mechanism, it is not clear that the snapthrough would occur, though the increase in the stress in the bilayer as the tube extends certainly could cause rupture, as hypothesized by Walani et al.

to form a bud [22, 39, 63]. Here we obtain buds as a result of protein-induced spontaneous curvature where the final radius of the bud depends on the membrane tension (Figure 2.10B; Section 2.4). Line tension was not explicitly accounted for in our model since we used a smooth function to model the interface representing the heterogeneity of the membrane (Figure 2.3). Line tension captures the energy of an interface, but by smoothing out this interface to a continuum with a sharp transition we are able to construct a single model for multiple domains.

Another aspect of heterogeneous membrane properties that we explored was variation in the Gaussian modulus between the coated and bare membrane, which has been demonstrated both theoretically [64] and experimentally [38] to affect the location of the phase boundary in the neck of phase-separated vesicles. In addition to affecting the location of the boundary relative to the neck, we found that variation in the Gaussian modulus has a profound effect on the progression of budding. Increasing the Gaussian modulus of the coat relative to the bare membrane inhibits budding, while decreasing it can smooth out the instability at intermediate membrane tension (Figure 2.16). While interesting, until more is known about how the lipid and protein composition at endocytic sites affects the Gaussian modulus, it is unclear what relevance these results have in CME.

One aspect of CME not explicitly addressed by this study is that the endocytic machinery includes curvature-generating proteins outside of the coat proteins and the actin machinery. In particular, recent modeling studies have demonstrated that cyclindrical curvature induced by BAR-domain proteins can play an important role in reducing the force requirement for productive CME in yeast [27, 42]. However, CME is still productive in 50% of events even with complete knockout of the endocytic BAR-domain proteins in this organism [65], while actin assembly is absolutely required [25, 26]. Additionally, in mammalian cells a large percentage of CCPs were found to stall at high membrane tension when actin is inhibited [5] despite the fact that the BAR-domain proteins were presumably unaffected. These results suggest that while curvature generated by BAR-domain proteins may help to facilitate productive CME, force from actin assembly seems to be most important in challenging mechanical environments.

Model predictions

Our model makes several experimentally testable predictions.

- There is conflicting evidence as to whether actin is an essential component of the endocytic machinery in mammalian cells [5, 21, 32]. We predict that CME in cell types with higher membrane tensions (i.e. Ves < 1) will be sensitive to perturbations to actin dynamics. Similarly, a reduction in membrane tension might relieve the necessity for actin polymerization in cells types where it has been found to be important for productive CME. A systematic study of the membrane tension in different cell types along with the sensitivity of CME to actin inhibitors will provide a strong test of the model and potentially clarify the role of actin in CME in mammalian cells.
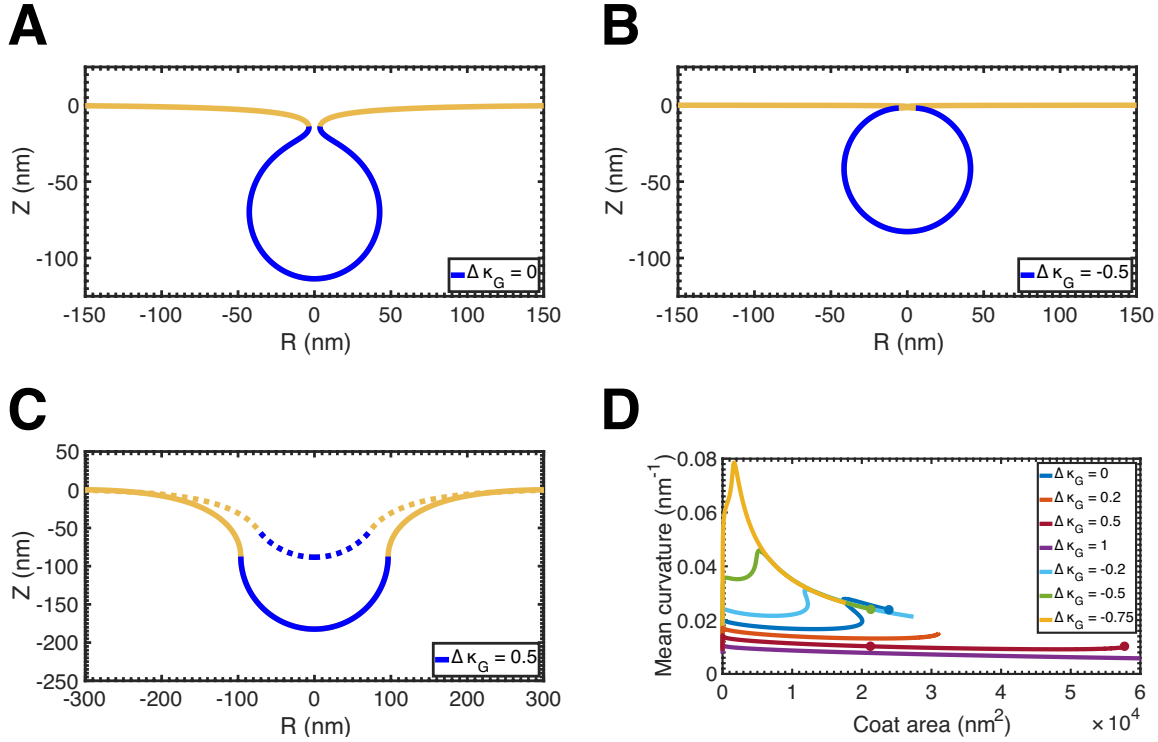
Figure 2.16: Effect of Gaussian modulus variation on membrane budding via increasing coat area, $\lambda_0 = 0.2\,\mathrm{pN/nm}$. We define $\Delta\kappa_G \equiv \left(\kappa_{G,\mathrm{coat}} - \kappa_{G,\mathrm{bare}}\right)/\kappa_0$ as the difference in the Gaussian modulus between the coated and bare membrane normalized by the bending modulus. **(A)** Membrane morphology in which there is no difference between the Gaussian modulus in the coated region and in the bare membrane, $A_{\mathrm{coat}} = 23{,}859\,\mathrm{nm}^2$. The boundary between the coated region and the bare membrane lies at the bud neck. **(B)** Membrane morphology in which the Gaussian modulus is lower in the coated region than in the bare membrane, $A_{\mathrm{coat}} = 21{,}278\,\mathrm{nm}^2$. The boundary between the coat and the bare membrane does not reach the bud neck, even for a vanishing neck radius. This is in agreement with the findings of Jülicher and Lipowsky [64]. **(C)** Membrane morphology in which the Gaussian modulus is higher in the coated region than in the bare membrane (dashed line, $A_{\mathrm{coat}} = 21{,}278\,\mathrm{nm}^2$; solid line, $A_{\mathrm{coat}} = 57{,}733\,\mathrm{nm}^2$). Note the difference in the axes as compared to (A) and (B). Closed buds do not form for typical ranges of coat area, though a deep U-shaped bud was present at the end of the solution branch (see (D)). This indicates that an additional solution branch of closed bud solutions may exist, but we were unable to obtain any closed bud solutions by our numerical scheme (see SOM Section 2.3). **(D)** Mean curvature at the bud tip as a function of coat area for several values of $\Delta\kappa_G$. The marked positions indicate the membrane profiles shown in (A), (B), and (C). Increasing the Gaussian modulus of the coated region relative to the bare membrane inhibits bud formation at typical coat areas, whereas decreasing the coat Gaussian modulus relative to the bare membrane can abolish the snapthrough transition otherwise present at intermediate membrane tension.

- Reduction in the spontaneous curvature of the clathrin coat will have severe effects on CME dynamics at elevated membrane tension. A recent study by Miller et al. showed that depletion of the endocytic adaptor proteins AP2 and CALM resulted in smaller and larger CCPs, respectively [12]. This effect was attributed to the presence of a curvature-driving amphipathic helix in CALM and the fact that AP2 typically recruits bulkier cargos than CALM, which translates in our framework into a reduction of the coat spontaneous curvature upon CALM depletion. We predict that CME in cells depleted of CALM will be more sensitive to increase in membrane tension (and/or actin inhibition) than in cells depleted of AP2 because successful budding is predicted to be a function of both membrane tension and spontaneous curvature (Figure 2.10).

- Reduction in the stiffness of the coat will inhibit its ability to bend membranes, especially at elevated membrane tension. This effect could be directly tested in a reconstitution system similar to that of Saleem et al. [22] in the presence or absence of clathrin light chains which have been shown to modulate the stiffness of the clathrin lattice [66].

Limitations of the model

Despite the agreement with experimental data and generation of model predictions, we acknowledge some limitations of our model. Our model is valid only for large length scale deformations, since the Helfrich energy is valid over length scales much larger than the thickness of the bilayer [13]. Further, we have assumed mechanical equilibrium for the membrane and future efforts will focus on including dynamics of the membrane. And finally, spontaneous curvature is one term that gathers many aspects of membrane bending while ignoring exact molecular mechanisms (protein insertion into the bilayer versus crowding). While it is effective for representing the energy changes to the membrane due to protein interaction, detailed models will be needed to explicitly capture the different mechanisms.

Conclusions

Reductionist approaches in cell biology, while very powerful in identifying univariate behavior, can be limited in their conclusions because processes like CME are controlled by multiple variables. Using a "systems" approach, we have investigated a multivariate framework that identifies the fundamental design principles of budding. Despite the inherent complexities of protein-induced budding, we found that coat area, coat spontaneous curvature, bending moduli, and actin-mediated forces are general factors that can contribute to robust vesiculation against opposing forces like membrane tension.

Though we have primarily focused on budding in the context CME, our findings are general to any budding process. For example, it has been shown that membrane deformation by COPI coats is also inhibited by membrane tension [36] and that rigidity of the COPII coat is essential for export of bulky cargos [67]. Since the membranes of the endoplasmic

reticulum and the Golgi are also under tension [68], we expect that the shape evolution of buds from these organelles is also determined by a balance of the coat spontaneous curvature, bending rigidity and membrane tension. Other membrane invaginations are also presumably governed by a similar set of physical parameters. For example, caveolae have been proposed to act as a membrane reservoir that buffers changes in membrane tension by disassembling upon an increase in membrane tension [23]. A similar framework to the one used in this study might provide some insight into the morphology and energetics of membrane buffering by caveolae. Moving forward, more detailed measurements of both the membrane tension within cells and the spontaneous curvature of various membrane-bending proteins will be essential to verify and extend the results presented here.

References

1. Johannes, L., Wunder, C. & Bassereau, P. Bending "on the rocks" – a cocktail of biophysical modules to build endocytic pathways. *Cold Spring Harbor perspectives in biology* **6,** a016741 (2014).

2. Taylor, M. J., Perrais, D. & Merrifield, C. J. A high precision survey of the molecular dynamics of mammalian clathrin-mediated endocytosis. *PLoS biology* **9,** e1000604 (2011).

3. Liu, J., Sun, Y., Drubin, D. G. & Oster, G. F. The mechanochemistry of endocytosis. *PLoS biology* **7,** e1000204 (2009).

4. Liu, J., Sun, Y., Oster, G. F. & Drubin, D. G. Mechanochemical crosstalk during endocytic vesicle formation. *Current opinion in cell biology* **22,** 36–43 (2010).

5. Boulant, S., Kural, C., Zeeh, J.-C., Ubelmann, F. & Kirchhausen, T. Actin dynamics counteract membrane tension during clathrin-mediated endocytosis. *Nature cell biology* **13,** 1124 (2011).

6. Kirchhausen, T., Owen, D. & Harrison, S. C. Molecular structure, function, and dynamics of clathrin-mediated membrane traffic. *Cold Spring Harbor perspectives in biology* **6,** a016725 (2014).

7. McMahon, H. T. & Boucrot, E. Molecular mechanism and physiological functions of clathrin-mediated endocytosis. *Nature reviews Molecular cell biology* **12,** 517 (2011).

8. Dannhauser, P. N. & Ungewickell, E. J. Reconstitution of clathrin-coated bud and vesicle formation with minimal components. *Nature cell biology* **14,** 634 (2012).

9. Ford, M. G. *et al.* Curvature of clathrin-coated pits driven by epsin. *Nature* **419,** 361 (2002).

10. Stachowiak, J. C. *et al.* Membrane bending by protein–protein crowding. *Nature cell biology* **14,** 944 (2012).

11. Busch, D. J. *et al.* Intrinsically disordered proteins drive membrane curvature. *Nature communications* **6,** 7875 (2015).

12. Miller, S. E. *et al.* CALM regulates clathrin-coated vesicle size and maturation by directly sensing and driving membrane curvature. *Developmental cell* **33,** 163–175 (2015).

13. Helfrich, W. Elastic properties of lipid bilayers: theory and possible experiments. *Zeitschrift für Naturforschung C* **28,** 693–703 (1973).

14. Lipowsky, R. Spontaneous tubulation of membranes and vesicles reveals membrane tension generated by spontaneous curvature. *Faraday discussions* **161,** 305–331 (2013).

15. Dimova, R. Recent developments in the field of bending rigidity measurements on membranes. *Advances in colloid and interface science* **208,** 225–234 (2014).

16. Stachowiak, J. C., Brodsky, F. M. & Miller, E. A. A cost–benefit analysis of the physical mechanisms of membrane curvature. *Nature cell biology* **15,** 1019 (2013).

17. Pinot, M. *et al.* Polyunsaturated phospholipids facilitate membrane deformation and fission by endocytic proteins. *Science* **345,** 693–697 (2014).

18. Hochmuth, F., Shao, J.-Y., Dai, J. & Sheetz, M. P. Deformation and flow of membrane into tethers extracted from neuronal growth cones. *Biophysical journal* **70,** 358–369 (1996).

19. Diz-Muñoz, A., Fletcher, D. A. & Weiner, O. D. Use the force: membrane tension as an organizer of cell shape and motility. *Trends in cell biology* **23,** 47–53 (2013).

20. Shi, Z. & Baumgart, T. Membrane tension and peripheral protein density mediate membrane shape transitions. *Nature communications* **6** (2015).

21. Yarar, D., Waterman-Storer, C. M. & Schmid, S. L. A dynamic actin cytoskeleton functions at multiple stages of clathrin-mediated endocytosis. *Molecular biology of the cell* **16,** 964–975 (2005).

22. Saleem, M. *et al.* A balance between membrane elasticity and polymerization energy sets the shape of spherical clathrin coats. *Nature communications* **6,** 6249 (2015).

23. Sinha, B. *et al.* Cells respond to mechanical stress by rapid disassembly of caveolae. *Cell* **144,** 402–413 (2011).

24. Wen, P. J. *et al.* Actin dynamics provides membrane tension to merge fusing vesicles into the plasma membrane. *Nature communications* **7,** 12604 (2016).

25. Kaksonen, M., Sun, Y. & Drubin, D. G. A pathway for association of receptors, adaptors, and actin during endocytic internalization. *Cell* **115,** 475–487 (2003).

26. Basu, R., Munteanu, E. L. & Chang, F. Role of turgor pressure in endocytosis in fission yeast. *Molecular biology of the cell* **25,** 679–687 (2014).

27. Dmitrieff, S. & Nédélec, F. Membrane mechanics of endocytosis in cells with turgor. *PLoS computational biology* **11,** e1004538 (2015).

28. Cureton, D. K., Massol, R. H., Saffarian, S., Kirchhausen, T. L. & Whelan, S. P. Vesicular stomatitis virus enters cells through vesicles incompletely coated with clathrin that depend upon actin for internalization. *PLoS pathogens* **5,** e1000394 (2009).

29. Piccinotti, S., Kirchhausen, T. & Whelan, S. P. Uptake of rabies virus into epithelial cells by clathrin-mediated endocytosis depends upon actin. *Journal of virology* **87,** 11637–11647 (2013).

30. Kukulski, W., Schorb, M., Kaksonen, M. & Briggs, J. A. Plasma membrane reshaping during endocytosis is revealed by time-resolved electron tomography. *Cell* **150,** 508–520 (2012).

31. Picco, A., Mund, M., Ries, J., Nedelec, F. & Kaksonen, M. Visualizing the functional architecture of the endocytic machinery. *Elife* **4,** e04535 (2015).

32. Grassart, A. *et al.* Actin and dynamin2 dynamics and interplay during clathrin-mediated endocytosis. *J Cell Biol* **205,** 721–735 (2014).

33. Aguet, F., Antonescu, C. N., Mettlen, M., Schmid, S. L. & Danuser, G. Advances in analysis of low signal-to-noise images link dynamin and AP2 to the functions of an endocytic checkpoint. *Developmental cell* **26,** 279–291 (2013).

34. Dai, J. & Sheetz, M. P. Mechanical properties of neuronal growth cone membranes studied by tether formation with laser optical tweezers. *Biophysical journal* **68,** 988–996 (1995).

35. Dai, J., Sheetz, M. P., Wan, X. & Morris, C. E. Membrane tension in swelling and shrinking molluscan neurons. *Journal of Neuroscience* **18,** 6681–6692 (1998).

36. Manneville, J.-B. *et al.* COPI coat assembly occurs on liquid-disordered domains and the associated membrane deformations are limited by membrane tension. *Proceedings of the National Academy of Sciences* **105,** 16946–16951 (2008).

37. Seifert, U. Configurations of fluid membranes and vesicles. *Advances in physics* **46,** 13–137 (1997).

38. Baumgart, T., Das, S., Webb, W. W. & Jenkins, J. T. Membrane elasticity in giant vesicles with fluid phase coexistence. *Biophysical journal* **89,** 1067–1080 (2005).

39. Sens, P. & Turner, M. S. Theoretical model for the formation of caveolae and similar membrane invaginations. *Biophysical journal* **86,** 2049–2057 (2004).

40. Różycki, B., Boura, E., Hurley, J. H. & Hummer, G. Membrane-elasticity model of Coatless vesicle budding induced by ESCRT complexes. *PLoS computational biology* **8,** e1002736 (2012).

41. Liu, J., Kaksonen, M., Drubin, D. G. & Oster, G. Endocytic vesicle scission by lipid phase boundary forces. *Proceedings of the National Academy of Sciences* **103,** 10277–10282 (2006).

42. Walani, N., Torres, J. & Agrawal, A. Endocytic proteins drive vesicle growth via instability in high membrane tension environment. *Proceedings of the National Academy of Sciences* **112,** E1423–E1432 (2015).

43. Carlsson, A. E. & Bayly, P. V. Force generation by endocytic actin patches in budding yeast. *Biophysical journal* **106,** 1596–1606 (2014).

44. Zhang, T., Sknepnek, R., Bowick, M. & Schwarz, J. On the modeling of endocytosis in yeast. *Biophysical journal* **108,** 508–519 (2015).

45. Doyon, J. B. *et al.* Rapid and efficient clathrin-mediated endocytosis revealed in genome-edited mammalian cells. *Nature cell biology* **13,** 331 (2011).

46. Rawicz, W., Olbrich, K., McIntosh, T., Needham, D. & Evans, E. Effect of chain length and unsaturation on elasticity of lipid bilayers. *Biophysical journal* **79,** 328–339 (2000).

47. Agrawal, A. & Steigmann, D. J. Modeling protein-mediated morphology in biomembranes. *Biomechanics and modeling in mechanobiology* **8,** 371 (2009).

48. Rangamani, P., Mandadap, K. K. & Oster, G. Protein-induced membrane curvature alters local membrane tension. *Biophysical journal* **107,** 751–762 (2014).

49. Rangamani, P., Agrawal, A., Mandadapu, K. K., Oster, G. & Steigmann, D. J. Interaction between surface shape and intra-surface viscous flow on lipid membranes. *Biomechanics and modeling in mechanobiology* **12,** 833–845 (2013).

50. Steigmann, D. Fluid films with curvature elasticity. *Archive for Rational Mechanics and Analysis* **150,** 127–152 (1999).

51. Derényi, I., Jülicher, F. & Prost, J. Formation and interaction of membrane tubes. *Physical review letters* **88,** 238101 (2002).

52. Sens, P. & Plastino, J. Membrane tension and cytoskeleton organization in cell motility. *Journal of Physics: Condensed Matter* **27,** 273103 (2015).

53. Kuzmin, P. I., Zimmerberg, J., Chizmadzhev, Y. A. & Cohen, F. S. A quantitative model for membrane fusion based on low-energy intermediates. *Proceedings of the National Academy of Sciences* **98,** 7235–7240 (2001).

54. Avinoam, O., Schorb, M., Beese, C. J., Briggs, J. A. & Kaksonen, M. Endocytic sites mature by continuous bending and remodeling of the clathrin coat. *Science* **348,** 1369–1372 (2015).

55. Jin, A. J., Prasad, K., Smith, P. D., Lafer, E. M. & Nossal, R. Measuring the elasticity of clathrin-coated vesicles via atomic force microscopy. *Biophysical journal* **90,** 3333–3344 (2006).

56. Kaksonen, M., Toret, C. P. & Drubin, D. G. Harnessing actin dynamics for clathrin-mediated endocytosis. *Nature reviews Molecular cell biology* **7,** 404–414 (2006).

57. Van Oudenaarden, A. & Theriot, J. A. Cooperative symmetry-breaking by actin polymerization in a model for cell motility. *Nature cell biology* **1,** 493–499 (1999).

58. Giardini, P. A., Fletcher, D. A. & Theriot, J. A. Compression forces generated by actin comet tails on lipid vesicles. *Proceedings of the National Academy of Sciences* **100,** 6493–6498 (2003).

59. Burroughs, N. & Marenduzzo, D. Nonequilibrium-driven motion in actin networks: comet tails and moving beads. *Physical review letters* **98,** 238302 (2007).

60. Bieling, P. *et al.* Force feedback controls motor activity and mechanical properties of self-assembling branched actin networks. *Cell* **164,** 115–127 (2016).

61. Collins, A., Warrington, A., Taylor, K. A. & Svitkina, T. Structural organization of the actin cytoskeleton at sites of clathrin-mediated endocytosis. *Current Biology* **21,** 1167–1175 (2011).

62. Dai, J. & Sheetz, M. P. Membrane tether formation from blebbing cells. *Biophysical journal* **77,** 3363–3370 (1999).

63. Sens, P. & Turner, M. S. Budded membrane microdomains as tension regulators. *Physical Review E* **73,** 031918 (2006).

64. Jülicher, F. & Lipowsky, R. Shape transformations of vesicles with intramembrane domains. *Physical Review E* **53,** 2670 (1996).

65. Kishimoto, T. *et al.* Determinants of endocytic membrane geometry, stability, and scission. *Proceedings of the National Academy of Sciences* **108,** E979–E988 (2011).

66. Dannhauser, P. N. *et al.* Effect of clathrin light chains on the stiffness of clathrin lattices and membrane budding. *Traffic* **16,** 519–533 (2015).

67. Čopič, A., Latham, C. F., Horlbeck, M. A., D'Arcangelo, J. G. & Miller, E. A. ER cargo properties specify a requirement for COPII coat rigidity mediated by Sec13p. *Science* **335,** 1359–1362 (2012).

68. Upadhyaya, A. & Sheetz, M. P. Tension in tubulovesicular networks of Golgi and endoplasmic reticulum membranes. *Biophysical journal* **86,** 2923–2928 (2004).

Chapter 3

Quantitative evidence for an endocytic transition point revealed by systematic imaging of clathrin-mediated endocytosis in budding yeast

3.1 Introduction

Clathrin-mediated endocytosis (CME) is an essential process in eukaryotes involved in nutrient uptake, regulation of biochemical signaling pathways, and in plasma membrane homeostasis [1]. Over 60 different proteins have been identified to directly participate in CME [2]. Two-color live cell microscopy and functional studies have established both the relative timing and putative biophysical and/or biochemical roles of a large number of these proteins [3–6]. Many of these studies have been undertaken using the budding yeast, *Saccharomyces cerevisiae*, due to its simplicity and genetic tractability, and the fact that components of the endocytic machinery are largely conserved across eukaryotes [7–9].

Figure 3.1A illustrates the general process of CME in budding yeast. Initially, a set of early proteins (including Ede1, Syp1 and Hrr25), and early coat proteins (including clathrin, the adaptor protein complex AP2 of which Apl1 is a subunit, and Pal1) mark the site of a nascent endocytic pit [10–12]. After a variable length of time (of 30 sec to more than 4 min), a set of mid-coat (Sla2) and late-coat (Pan1, Sla1) proteins is recruited to the endocytic site [3]. Subsequently, proteins in the so-called WASP/Myosin module (Las17, Vrp1, Bzz1, Myo5) are recruited and nucleate (Arp2/3 complex, of which Arc15 is a subunit) assembly of a branched actin network, which includes a number of additional actin binding proteins (Sac6, Abp1) [4]. Force generated by actin assembly [3, 13] and potentially myosin motor activity [5, 14] invaginates the plasma membrane and generates curvature, triggering the

recruitment of proteins involved in the scission (Rvs167) of the endocytic vesicle from the plasma membrane [15]. Disassembly of the clathrin coat and the rest of the endocytic machinery is then mediated in part by proteins (Ark1) recruited by actin binding proteins [3, 16].

Despite our large and growing knowledge of the roles and timing of these CME proteins, how timing and order of events during progression through the endocytic pathway are controlled is less well-understood. In particular, the necessary and sufficient conditions for the steps of endocytic site initiation, the point at which the mid- and late-coat proteins are recruited, and initiation of actin assembly (annotated as "initiation", "transition point", and "actin nucleation" in Figure 3.1A) are not known.

Initiation is known to be highly flexible and robust in the sense that no single early or early-coat protein is essential for the formation of endocytic sites, including clathrin itself [4, 17]. In fact, CME still occurs in yeast lacking nearly all of the of early endocytic proteins, though protein cargo uptake is impaired [18]. The early and early-coat proteins appear to all arrive concurrently at endocytic sites [11, 12], but it is not clear what conditions cause endocytic sites to form in the first place.

The early stage of CME is sometimes called the "variable phase", so-called because the residence times of early proteins are highly variable [10–12]. By contrast, beginning with the recruitment of the mid- and late-coat proteins, the dynamics of protein recruitment to endocytic sites are generally thought to be quite regular [3, 4]. Consequently the late stage of CME is sometimes also referred to as the "regular phase". Though there is some evidence of roles for cargo sensing [11, 19] and ubiquitination of endocytic proteins [20] in mediating the transition from variable to regular dynamics, how and why the dynamics change at this transition is not known.

Actin nucleation and assembly at endocytic sites is controlled by a number of factors, most prominently activation of the Arp2/3 complex [3], which can be accomplished by a number of CME proteins including Las17 (budding yeast WASP), Pan1, Myo3 and Myo5 (type 1 myosins), and Abp1 [5, 21]. This apparent redundancy makes it difficult to determine what conditions cause actin to begin to assemble, though there is some evidence for a "switch-like" nucleation of actin assembly apparently dependent on Las17 copy number at the endocytic site [22]. Beyond the initial nucleation step for actin assembly, how the timing and extent of actin assembly is controlled is also unclear.

I set out to investigate the necessary and sufficient conditions for each of these steps. To do this, I performed systematic two-color live cell microscopy on nearly two dozen different yeast strains encompassing the entire pathway, measuring the residence times and maximum fluorescence intensities of proteins at thousands of endocytic sites. After finding unexpected variability in the lifetimes and abundances of proteins even in the "regular phase", I determined whether the lifetimes of these various proteins could tell me anything about the lifetimes or abundances of canonical proteins whose appearance signals the passage through each step I set out to investigate. My principal finding is that there is quantitative evidence for a true regulatory transition point between the early, "variable phase" and late, "regular phase" of CME.

3.2 Inherent variability in clathrin-mediated endocytosis revealed by systematic imaging

In order to examine the necessary and sufficient conditions for CME to progress through the stages of initiation, transition to regularity, and onset of actin assembly I undertook a systematic imaging approach. I acquired live-cell two-color total internal reflection fluorescence (TIRF) microscopy movies of nearly two dozen different strains of the budding yeast, *Saccharomyces cerevisiae* (see Tables 3.1 and 3.2), in which an endocytic protein of interest was tagged with GFP and a reporter protein for the various stages of progression through CME was tagged with a red fluorophore. I chose Ede1, a key component of the early endocytic module [10, 11], Sla1, a late-arriving coat protein [3], and Abp1, a reporter of endocytic actin networks in budding yeast [3], all of which are relatively abundant at endocytic sites (and hence bright), as reference proteins for initiation, transition to regularity, and actin assembly, respectively. TIRF microscopy was chosen in lieu of the lab's standard imaging modality of widefield microscopy of the medial focal plane of the yeast cells [3, 4] because TIRF has superior signal-to-noise as well as minimal photobleaching, though this comes at the cost of losing information about the internalization of the endocytic pit. The benefits of TIRF microscopy were especially important for faithfully detecting and tracking the early endocytic proteins which are both dimmer and have longer residence times at endocytic patches.

Endocytic sites are smaller than the diffraction limit of light, and so they appear as diffraction-limited spots when imaged by conventional fluorescence microscopy [3, 23]. Figure 3.1B depicts a representative montage of an endocytic site, in this case with Las17, the yeast WASP, as the GFP-tagged protein of interest arriving prior to Abp1-RFP and then disappearing as the endocytic pit internalizes and leaves the TIRF field [23]. I used the cmeAnalysis MATLAB package [24] to automatically track all of the endocytic sites in many fields of yeast cells. I then used custom MATLAB scripts to identify and associate green and red spots that were colocalized while rejecting sites that were too close to one another, and subsequently to extract their background-subtracted fluorescence intensity (See Materials and Methods, Section 3.5, for full details). The lower portion of Figure 3.1B plots the tracked location (centroid) of the green and red fluorescence for the endocytic site depicted in the montage, with the ● indicating the beginning of the track and the **x** marking the end.

Figure 3.1C plots the fluorescence intensity over time of the tracked endocytic site shown in Figure 3.1B. Vertical dashed lines indicate the start and end of the traces as determined by the automated tracking software. I define the time between the beginning and end of a trace as the "lifetime" as is standard in the literature [3], as well as the time between the start of the green and the red traces as the "time to arrival" of the red reporter protein. Rather than average the traces across many endocytic sites to obtain an average lifetime, time to arrival, or maximum intensity, I sought to use the inherent variability in endocytic sites to obtain new insights into the process.

Next, I wanted to determine whether this systematic imaging approach recapitulates
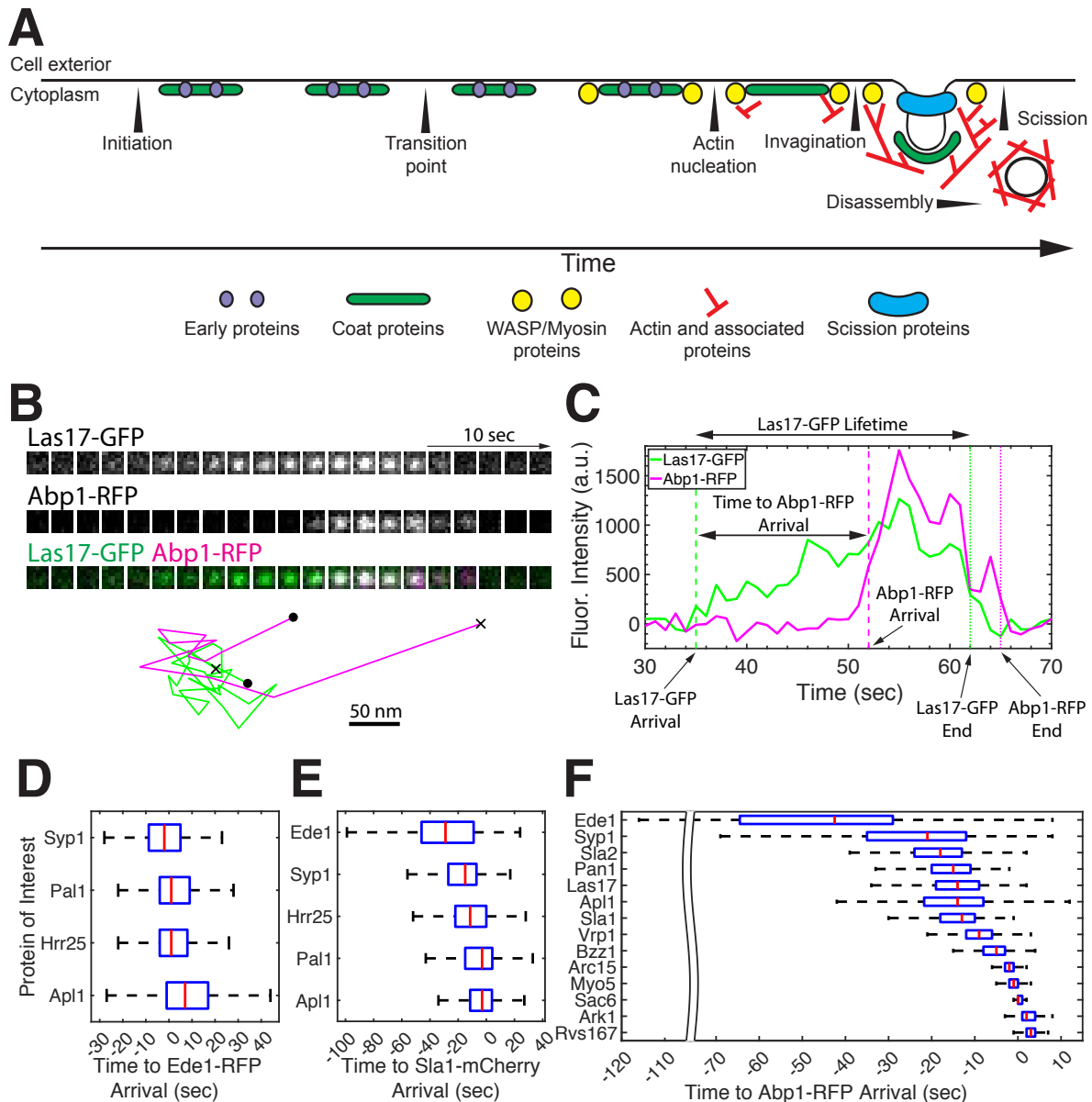
Figure 3.1: Systematic imaging of clathrin-mediated endocytosis in budding yeast recapitulates the canonical timeline. (A) Illustration of key steps in the clathrin-mediated endocytosis pathway in budding yeast. (B) Top: Montage of Las17-GFP, Abp1-RFP and a merge acquired by simultaneous live two-color TIRF microscopy of budding yeast. Bottom: Centroid position over time of the Las17-GFP (green) and Abp1-RFP (magenta) spots as depicted in the montage; ● - beginning, ✗ - end. (C) Fluorescence intensity vs. time for Las17-GFP and Abp1-RFP spots depicted in panel B. (D-F) Time from the appearance of the indicated GFP-tagged protein of interest to the appearance of D) Ede1-RFP, an early arriving protein, E) Sla1-mCherry, a late-coat protein and F) Abp1-RFP, an endocytic actin binding protein. For full numerical summaries of number of observations and time to arrival statistics, see Tables 3.3-3.5.

the canonical timeline [2] of endocytic protein arrival and residence time that has been established through sequential rounds of live-cell two color imaging by several groups across many studies. Using the "time to arrival" metric defined previously, I staged each of the GFP-tagged proteins of interest by their median time to arrival relative to Ede1-RFP (Figure 3.1D), Sla1-mCherry (Figure 3.1E), and Abp1-RFP (Figure 3.1F). As a positive control, I find that Sac6, the yeast fimbrin, an endocytic actin crosslinker [25], arrives at essentially the same time as Abp1, an endocytic actin-binding protein. Similarly, I find that the early proteins Syp1, Pal1, and Hrr25 arrive at approximately the same time as Ede1, though with substantial variability, as previously reported [11, 12]. One discrepancy with the literature I find is that Ede1 is found to be by far the earliest arriving protein when imaging Ede1-GFP with both Sla1-mCherry and Abp1-RFP. Another discrepancy is that Apl1-GFP is found to arrive with similar timing to later arriving proteins as opposed to the earliest arriving proteins when imaged with Abp1-RFP. I believe the most likely explanation for these discrepancies are their relative brightnesses, as discussed below, combined with the possibility that the automated detection and tracking may give different results from those previously obtained [11]. However, there are functional implications for CME if these data were to be confirmed by subsequent studies. Ede1 is known to play a key role in the establishment of endocytic sites and the localization of other early proteins [10], while AP2 (of which Apl1 is a subunit) is thought to primarily play a role in cargo selection [26]. It is possible that initiation and cargo selection in CME are separable processes not just functionally, but also in timing, which is supported by my data.

Otherwise, the relative timing of nearly all of the GFP-tagged proteins of interest is broadly recapitulated and some fine-grained differences are captured that are good tests of the robustness of this approach. For instance, I find that Arp2/3 complex (Arc15-GFP) precedes actin bundling (Sac6-GFP) ultimately followed by Ark1-GFP (recruited by Abp1 [16]) and Rvs167-GFP (recruited to curvature following deformation of the membrane by actin assembly [6, 27]). These timing data give me confidence that I can make further comparisons between lifetimes and intensities of the GFP-tagged proteins of interest which were imaged over many days and independent imaging sessions.

As a further check that my dataset is consistent with data obtained in previous studies, I plotted the lifetimes of each GFP-tagged protein of interest when it colocalized with Ede1-RFP (Figure 3.2A), Sla1-mCherry (Figure 3.2B), and Abp1-RFP (Figure 3.2C). The median lifetimes I obtained are indeed broadly consistent with published results, though in some cases slightly shorter [3, 4, 10–12]. The shorter lifetimes can be explained by the fact that disappearance of the fluorophore from the TIRF field does not necessarily indicate disassembly. Other imaging modalities can capture the full lifetime of proteins as the endocytic pit moves into the cell. In any case, the median lifetimes I report are consistent with those reported previously, so I am satisfied with the quality of data obtained through the automated tracking and cleaning procedure.

Given that that recruitment dynamics of the late-arriving proteins are often described as being quite "regular" [7, 10], I was somewhat surprised by the magnitude of the variability in the lifetimes of these proteins. One measure of variability is the coefficient of variation, which
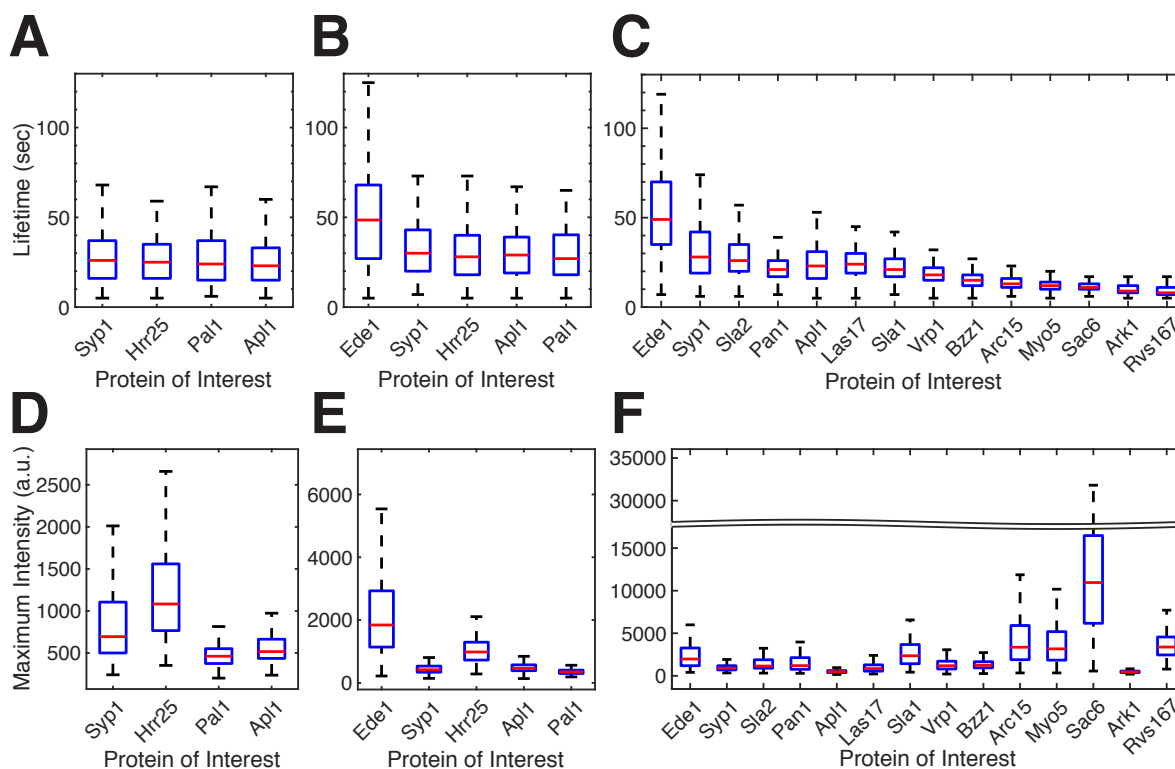
Figure 3.2: The lifetimes and relative fluorescence intensities of the GFP-tagged proteins of interest are consistent with published results. (A-C) Lifetime of the indicated GFP-tagged protein of interest when colocalized with A) Ede1-RFP, B) Sla1-mCherry, and C) Abp1-RFP. (D-E) Maximum fluorescence intensity of the indicated GFP-tagged protein of interest when colocalized with D) Ede1-RFP, E) Sla1-mCherry, and F) Abp1-RFP. For full numerical summaries of number of observations, lifetimes, and intensities, see Tables 3.6-3.17.

is simply the ratio of the standard devation to the mean [28]. By this measure, the standard deviation of the lifetimes of nearly all of the late-arriving proteins is approximately 30% of the mean lifetimes (see Table 3.8). This result appears to be consistent with previously reported lifetime data [3–5], suggesting that the purported "regularity" of late-stage CME is in the relative arrival timing of proteins as opposed to their lifetimes across different endocytic sites. My data do however confirm that the "variable", early stage of CME truly is more variable than the "regular" late stage. The coefficient of variation for the early-arriving proteins is approximately 50% (see Tables 3.6-3.8) as compared to the 30% of the late-arriving proteins, indicating that their truly is a transition in the recruitment dynamics of endocytic proteins. To summarize, these data show that both the early stage and the late stage of CME are inherently stochastic, at least in terms of protein lifetimes; only the extent of variability between the two stages differs.

Next, I plotted the maximum fluorescence intensity of each GFP-tagged protein of interest for spots colocalized with Ede1-RFP (Figure 3.2D), Sla1-mCherry (Figure 3.2E), and Abp1-RFP (Figure 3.2F). One caveat for these data is that, because they were acquired using

TIRF microscopy (where the illumination intensity of the laser falls off exponentially with
the distance from the coverslip [29]) and endocytic sites are not all equally close to the
coverslip (due to the curvature of the yeast cells and the fact that endocytic sites appear to
occur all over the cell cortex [4]), not all endocytic sites are illuminated to the same extent
and hence I would expect to see significant variability in the maximum intensity of different
endocytic sites.

Despite this caveat, these data are broadly consistent with measurements of protein copy
number at endocytic sites [6] as well as with my general impressions of the brightness of these
spots while imaging, the "eye test". Ede1 is clearly the most abundant early protein, with
the remaining early proteins being substantially lower in copy number. (Hrr25 is 3xGFP-
tagged, so this feature must be considered when making comparisons to this protein.) The
brightness of Ede1-GFP (and hence the ability to detect its presence) relative to the other
GFP-tagged proteins of interest may account for the fact that I observe Ede1 as the first
early-arriving protein when colocalized with Sla1-mCherry or Abp1-RFP (Figures 3.1E and
F, respectively), but not when Ede1 itself was the RFP-tagged reference protein (Figure
3.1D). Similarly, the relative dimness of Apl1-GFP relative to Syp1-GFP and the mid- and
late-arriving proteins could explain why I observe it arriving later than the other early
proteins in comparison to the arrival of Abp1-RFP (Figure 3.1F). The only discrepancy in
these data compared to that of Picco *et al* [6] is my slight undercounting of the Arp2/3
complex subunit Arc15 relative to the type-I myosin Myo5. This might be explained by
the fact that Myo5 is located at the base of endocytic pits as compared to actin assembly
which occurs all over the endocytic site [30], meaning that Myo5-GFP would be exposed
to a higher laser intensity on average than Arc15-GFP. Next, I wanted to examine whether
there was any relationship between the lifetimes of the GFP-tagged proteins of interest and
their maximum fluorescence intensity, which can be used as a proxy for the copy number of
that protein at the endocytic site [6, 31].

Figures 3.3A-C plot the maximum fluorescence intensity of all of the Ede1-GFP, Las17-
GFP, and Sac6-GFP spots against their lifetimes, where the color of the dots indicates
the density of data around each point. Ede1 is an early protein that is known to have a
highly variable lifetime [10], which I also find (Figure 3.3A). The maximum fluorescence
intensity also exhibits significant variability, which could be a consequence of imaging using
TIRF microscopy, as discussed previously. Though Las17 and Sac6 (Figure 3.3B and C,
respectively) are late-arriving endocytic proteins and thus part of the "regular" phase of
CME, I observe substantial variability in the lifetimes and the maximum intensities of both
proteins.

One might expect, given the highly interconnected nature of protein interactions of en-
docytic sites [32], that a longer lifetime would necessarily lead to a greater abundance of
all endocytic proteins. To test this, I performed linear fits to the maximum intensity and
lifetimes of each GFP-tagged protein of interest (see first column, Figures 3.6-3.10), shown
by the red lines. The R^2 of each fit can be interpreted as the percentage of the variabil-
ity in maximum intensity can be explained by the variation in lifetime [33]. For example,
Ede1-GFP (Figure 3.3A) has essentially no correlation between its maximum intensity and
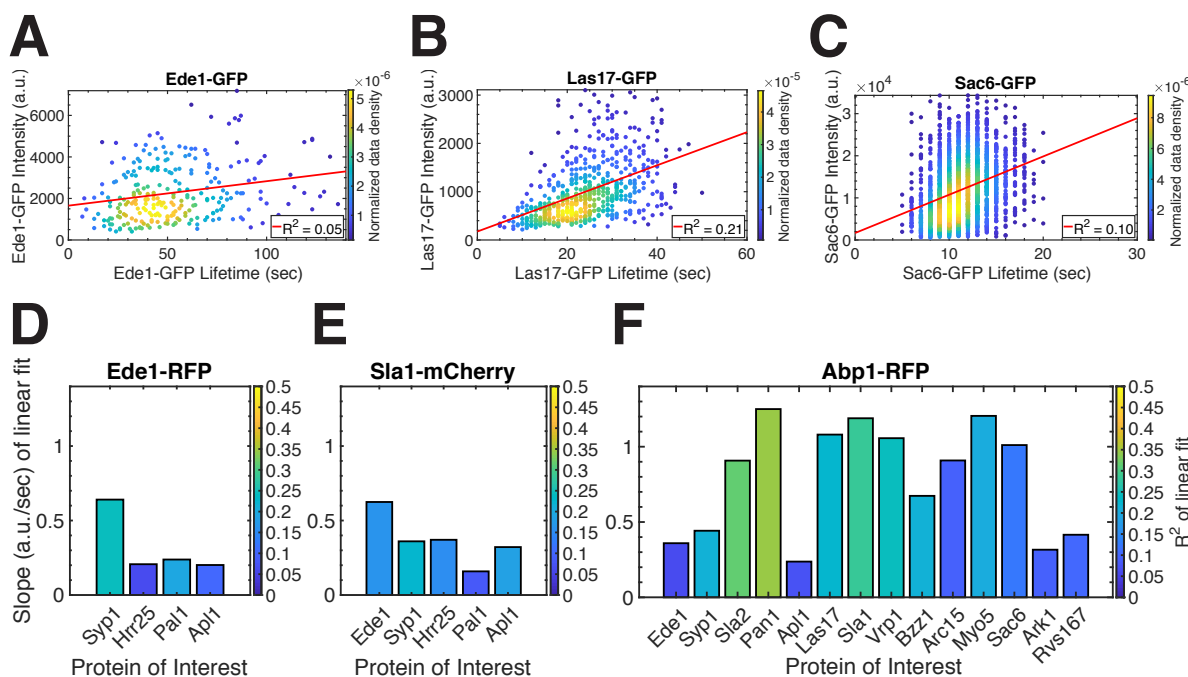
Figure 3.3: Correlations between endocytic protein lifetime and fluorescence intensity provide novel insights. (A-C) Scatterplots of maximum intensity vs. lifetime of A) Ede1-GFP, B) Las17-GFP, and C) Sac6-GFP. Color indicates the normalized data density in the neighborhood around each point. Red lines are linear fits to the data with the indicated R^2 values. (D-F) Summaries from performing linear fits to the maximum intensity of the indicated GFP-tagged proteins of interest vs. their lifetimes that were colocalized with D) Ede1-RFP, E) Sla1-mCherry, and F) Abp1-RFP. The bar height and color indicate the normalized slope and the R^2 of the fit, respectively. For full numerical summaries of number of observations, fit slopes and R^2, and 95% confidence intervals, see Tables 3.18-3.20.

lifetime, with an $R^2 = 0.05$. By contrast, Las17-GFP (Figure 3.3B) has a moderate positive correlation between lifetime and maximum intensity, $R^2 = 0.21$. In other words, endocytic sites where Las17 last longer on the cortex appear to gain more Las17 than those that are shorter lived. Lastly, Sac6-GFP (Figure 3.3C) has only a weak correlation between lifetime and intensity, $R^2 = 0.10$.

I can summarize the results of the fits for each GFP-tagged protein of interest by generating bar plots (Figures 3.3D-F) where the height and color of the bars indicate the normalized slope and R^2 of the fit, respectively. Figures 3.3D, 3.3E, and 3.3F represent data collected from GFP spots that colocalized with Ede1-RFP, Sla1-mCherry, and Abp1-RFP, respectively. The slopes of the fits were normalized by dividing the intensities and lifetimes of each protein by their respective medians prior to the fit which does not affect the R^2. This normalization was performed to control for the fact that longer-lived and dimmer proteins would inherently have a lower slope than shorter-lived and brighter proteins.

After this normalization, it is apparent that, while all of the proteins of interest have postive slopes, those of the mid- and late-coat proteins as well as those belonging to the

WASP/myosin and actin modules tend to have substantially higher slopes than those of the early and early-coat. This observation suggests a model in which nascent endocytic sites assemble to a fairly regular size whereas later arriving proteins continuously accumulate until disassembly is triggered. The low slopes and correlations of Ark1, a kinase recruited by Abp1 and involved in endocytic site disassembly, and Rvs167, a BAR-domain protein recruited to regions of high tubular curvature and involved in scission, indicate that their copy number at endocytic sites is not primarily dictated by their own residence times.

Comparisons of the fits for Ede1-GFP and Syp1-GFP across the two and three datasets for which they were observed, respectively, can give us an indication of the robustness of this method to detect meaningful differences. Though the slope and R^2 of the fits for Ede1-GFP vary across the two datasets, they remain fairly low in both, suggesting that the lifetime and copy number of Ede1 at endocytic sites is not well correlated. The discrepancy between the two fits might be explained by the difficulty of finding sites of colocalized Ede1-GFP and Abp1-RFP as compared to Sla1-mCherry since Ede1 typically begins to leave endocytic sites before actin has even begun to assemble [10]. In any case, the fits for Syp1-GFP are quite consistent across the three datasets with nearly identical R^2 values (see Tables 3.18-3.20), giving me confidence that this method gives fairly consistent and meaningful results. So, while Syp1-GFP lifetime and copy number seem to be moderately correlated as measured by R^2, the relationship is not very strong in the sense that the slope is still relatively low compared to the late-arriving proteins.

3.3   Quantitative evidence for a regulatory transition point

Having developed the ability to draw meaningful conclusions from correlations between the lifetimes and maximum intensities of the GFP-tagged proteins of interest, I looked to see whether their lifetimes have any predictive power on the lifetimes and abundances of the red fluorophore-tagged reference proteins.

First, I plotted the lifetimes of the red fluorophore-tagged reference proteins against the lifetime of the colocalized GFP-tagged proteins of interest (second column, Figures 3.6-3.10). Representative examples of Abp1-RFP lifetime vs. lifetimes of Ede1-GFP, Las17-GFP, and Sac6-GFP are shown in Figures 3.4A, B, and C, respectively. As above, the color of each dot represents the normalized data density, and the red line is the linear fit to the data with the indicated R^2 value. As with relative arrival time, Sac6-GFP serves as a positive control because Sac6-GFP and Abp1-RFP lifetimes are expected to be highly positively correlated; this is indeed the case. By comparison, Abp1-RFP lifetime is only moderately positively correlated with Las17-GFP lifetime and shows essentially no correlation with Ede1-GFP lifetime.

Figure 3.4D, E, and F summarize the results of fitting the lifetimes of Ede1-RFP, Sla1-mCherry, and Abp1-RFP, respectively to the lifetimes of the GFP-tagged proteins of interest.

Figure 3.4: Lifetime vs. lifetime correlations provide evidence for a regulatory transition point. (A-C) Scatterplots of the lifetimes of Abp1-RFP vs. the lifetimes of A) Ede1-GFP, B) Las17-GFP, and C) Sac6-GFP. Color indicates the normalized data density in the neighborhood around the point. Red lines are linear fits to the data with the indicated R^2 value. (D-F) Summaries of performing linear fits to the lifetimes of D) Ede1-RFP, E) Sla1-mCherry, and F) Abp1-RFP vs. the lifetimes of the indicated GFP-tagged proteins of interest. The bar height and color indicate the normalized slope and the R^2 of the fit, respectively. For full numerical summaries of number of observations, fit slopes and R^2, and 95% confidence intervals, see Tables 3.21-3.23.

As before, the bar height and color indicate the normalized slope and R^2 of the fits, respectively. Figure 3.4D shows that the lifetime of Ede1-RFP is well-correlated with those of the other early proteins, with perhaps the exception of Apl1-GFP. By contrast, the lifetime of Sla1-mCherry is not well-correlated with those of the early proteins, with only Apl1-GFP having a mild correlation (Figure 3.4E). As stated previously, Sac6-GFP is effectively a positive control because its lifetime should be nearly identical to that of Abp1-RFP as they are both markers of endocytic actin in budding yeast; I indeed find that their lifetimes are strongly correlated. Similarly, Abp1-RFP lifetime is also well-correlated to those of Arc15-GFP, an Arp2/3 subunit, and Myo5-GFP, an endocytic type 1 myosin, which, along with its paralog Myo3, is responsible for anchoring actin assembly to the membrane so it can provide force for invagination [34]. By contrast, Abp1-RFP lifetime does not correlate well with the lifetimes of the early, early-coat or mid-coat proteins. These observations tell me that how long proteins reside at endocytic sites before the transition point or before the WASP/myosin module is recruited by the Pan1-End3 complex [35] does not appear to have much bearing on how long the late coat or actin filaments are present.
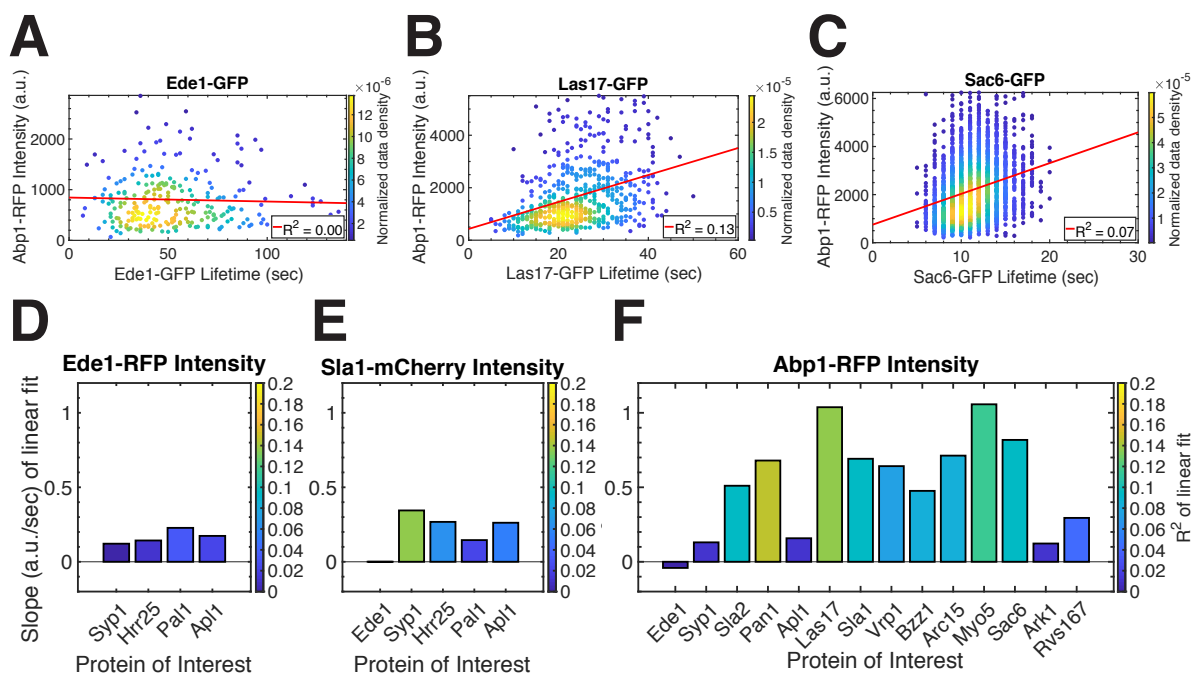
Figure 3.5: Correlations between reporter protein abundance and protein of interest lifetime provide further evidence for a regulatory transition point. (A-C) Scatterplots of the maximum intensities of Abp1-RFP vs. the lifetimes of A) Ede1-GFP, B) Las17-GFP, and C) Sac6-GFP. Colors indicates the normalized data density in the neighborhood around the point. Red lines are linear fits to the data with the indicated R^2 value. (D-F) Summaries from performing linear fits to the maximum intensity of D) Ede1-RFP, E) Sla1-mCherry, and F) Abp1-RFP vs. the lifetimes of the indicated GFP-tagged proteins of interest. The bar height and color indicate the normalized slope and the R^2 of the fit, respectively. For full numerical summaries of number of observations, fit slopes and R^2, and 95% confidence intervals, see Tables 3.24-3.26.

Next, I plotted the maximum fluorescence intensity of the red fluorophore-tagged reference proteins against the lifetimes of the colocalized GFP-tagged proteins of interest (third column, Figures 3.6-3.10). Figures 3.5A-C show representative examples of Abp1-RFP maximum intensity vs. lifetimes of Ede1-GFP, Las17-GFP, and Sac6-GFP, respectively. As with Abp1-RFP lifetime, the maximum intensity of Abp1-RFP is not correlated with Ede1-GFP lifetime. By contrast, Abp1-RFP maximum intensity is mildly, if somewhat weakly, correlated with both Las17-GFP and Sac6-GFP lifetime. It is not surprising that these correlations would be weaker than those of Abp1-RFP lifetime to protein of interest-GFP lifetime (Figures 3.4A-C). For one thing, the issue of apparent intensity of endocytic sites varying according to their position in the TIRF field is present here as well, which would obscure any trends I might expect to see. Secondly, because actin assembly at endocytic sites is controlled by a number of factors including activation of the Arp2/3 complex [3], myosin motor activity [5], and resistance to membrane internalization by turgor pressure [36, 37], it is not immediately apparent that the lifetime of any single endocytic proteins should correlate with the amount of actin assembly, and hence Abp1-RFP intensity. How-

ever, differences in the strengths of these correlations do suggest that I can draw potentially meaningful conclusions when the data are taken together.

Figures 3.5D, E and F summarize the results of fitting the maximum intensities of Ede1-RFP, Sla1-mCherry, and Abp1-RFP, respecti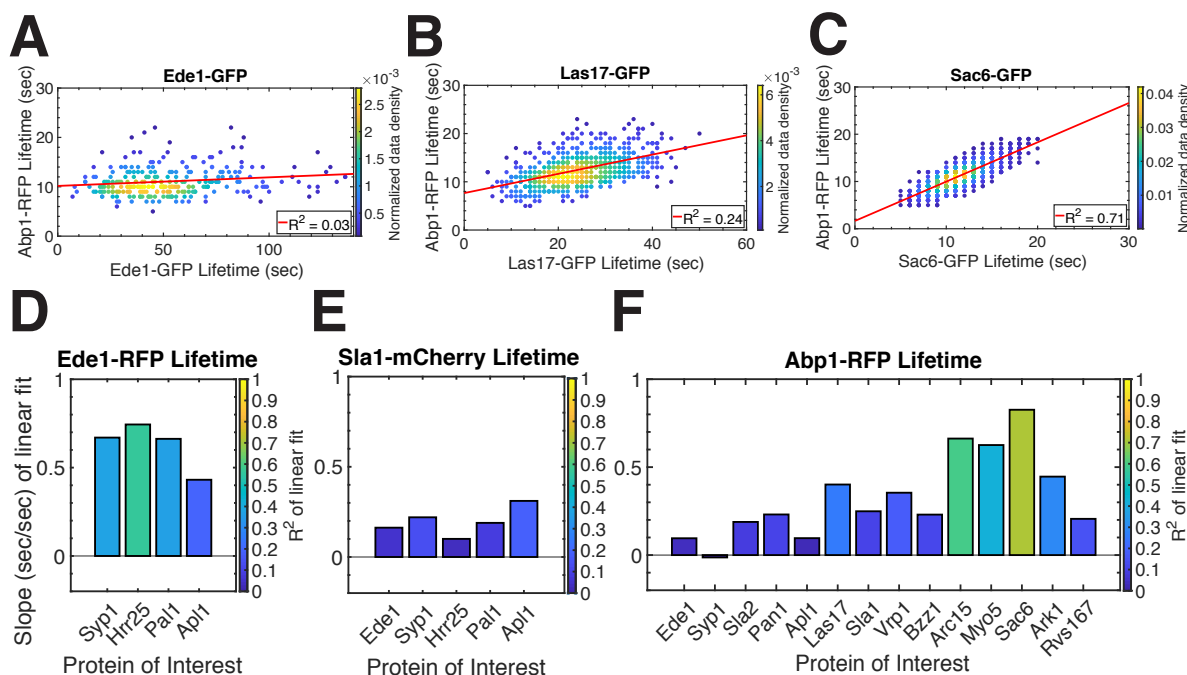vely, to the lifetimes of the GFP-tagged proteins of interest. As before, the bar height and color indicate the normalized slope and R^2 of the fits, respectively. Figure 3.5J shows that Ede1-RFP maximum intensity is not correlated with the lifetimes of any of the other early proteins. This result is consistent with the fact that the maximum intensity of Ede1-GFP was also not well correlated with its own lifetime (Figures 3.3E and F). The lifetime of Sla1-mCherry also does not appear to be well-correlated with the lifetimes of the early proteins, with the exception of Syp1-GFP which has a relatively high R^2 but still has a somewhat small slope (Figure 3.5E). Perhaps the most meaningful conclusions can be drawn from the correlations between Abp1-RFP maximum intensity and the GFP-tagged proteins of interest (Figure 3.5F). Somewhat surprisingly, the best correlation, in terms of both a high slope and relatively high R^2, was not to the lifetime of Sac6-GFP, but rather to those of Las17-GFP and Myo5-GFP. By contrast, the lifetimes of the early proteins Ede1, Syp1, and Apl1 showed no correlation with the extent of actin assembly. These data indicate that the lifetimes and probably the abundances of the early proteins do not have any bearing on the amount of actin that is assembled at endocytic sites.

Taken together, these data provide quantitative evidence for a regulatory transition point between the early stage and the late stage of CME.

3.4   Discussion

By systematically imaging GFP-tagged proteins throughout the CME pathway, I was able to generate and analyze a dataset that is both consistent with that of previous studies and provides new insights into the regulation of timing and abundance of proteins at endocytic sites.

Inherent variability of CME

There is substantially more variability in the lifetimes (and likely the abundances) of proteins at endocytic sites than is typically appreciated, especially in the so-called "regular phase" [7, 10]. This variability, along with the fact that nearly all endocytic sites in budding yeast are productive [15], supports the observation that CME is highly mechanically robust to various perturbations [4, 15, 36]. One question that I cannot answer here is whether the variability across lifetimes and abundances of all of the late stage CME proteins is correlated at individual endocytic sites over time. If so, such a correlation would suggest that this variability might be a caused by circumstances unique to each endocytic site, such as cargo composition, phosphorylation or ubiquitination states, patch size, etc. If not, this lack of correlation would imply that the variability is simply a result of stochastic recruitment of proteins to the endocytic site.

By examining the relationship between the lifetimes and maximum fluorescence intensities of the GFP-tagged proteins of interest, I found that the lifetimes of mid- and late-coat proteins, as well as those of the WASP/myosin module, correlate reasonably well with their maximum fluorescence intensity (Figure 3.3E). By contrast, the lifetimes and maximum intensities of the early and early-coat proteins are not well correlated (Figures 3.3D-F). I cannot say anything definitive about causality of lifetime vs. abundance, which could go either way; both could potentially be controlled by some other factor as well. However, it is clear that there is a quantitative difference between the recruitment dynamics of the early and late stages of CME that goes beyond previous observations that the lifetimes of early proteins are highly variable [10–12].

Initiation and transition from early to late stage CME

To my knowledge, this is the first report that the lifetimes of the early proteins are well-correlated with the lifetime of Ede1 (Figure 3.4), and thus presumably each other. This correlation implies that nascent endocytic sites contain a full complement of the early and early-coat proteins from their inception. The fact that the abundance of Ede1 as well as that of the other early and early-coat proteins does not appear to correlate with their lifetimes (Figures 3.3D-F and 3.5D) indicates that these early stage sites assemble and wait until something not captured by my analysis occurs that would trigger the recruitment of the mid-coat and subsequent late-arriving proteins. Furthermore, the lifetime of the early arriving proteins gives little if any insight into the recruitment dynamics (lifetime or abundance) of the late-coat protein Sla1 (Figures 3.4E and 3.5E). Taken together, these data suggest that something other than lifetime or protein abundance of "variable stage" endocytic sites dictates their progression to the "regular phase". Candidates for triggering the recruitment of the mid-coat proteins include the turnover dynamics of the early proteins, presence of cargo [11, 19], and the phosphorylation [2, 12] or ubiquitination state [20] of the early proteins.

Actin nucleation and assembly

It was initially surprising to me that Abp1-RFP maximum intensity correlated more strongly with Las17-GFP and Myo5-GFP lifetimes than the lifetime of Sac6-GFP, but this turns out to be a result that is consistent with what is known about the roles of these proteins at endocytic sites. Las17 and Myo3/Myo5 (together with verprolin) are the most potent Arp2/3 activators among the CME proteins [5], so one would expect that higher abundance of these proteins at CME sites would translate into a greater amount of actin assembly. The maximum intensity of both Las17-GFP and Myo5-GFP are fairly well correlated with their lifetimes (Figure 3.3F), and Las17 in particular arrives substantially before actin assembly begins (Figure 3.1F), giving it time to accumulate prior to nucleation. Thus, it appears that longer lifetimes of Arp2/3 activators leads to greater abundance of these activators at endocytic sites which results in greater actin assembly. By contrast, the maximum intensities of Arc15-GFP and Sac6-GFP are relatively less well correlated with their lifetimes, suggesting

that the rate of actin assembly is not equal across endocytic sites. This indicates that greater quantities of Arp2/3 activators leads not only to greater total actin assembly, but a higher rate of actin assembly, which it consistent with results from reconstitution studies [38].

Importantly, it is only the lifetimes of the mid-coat, late-coat and WASP/myosin module proteins that predict the kinetics of actin assembly, while the lifetimes of the early or early-coat proteins do not (Figures 3.4F and 3.5F). This observation reinforces the conclusion that kinetics and abundance of proteins recruited before the transition from early to late stage CME does not seem to have any bearing on these parameters after the transition.

Conclusions and outlook

Taken together, these data quantitatively substantiate the existence of a regulatory transition point between the early, or "variable", phase and the late, or "regular" phase of CME. Ongoing work has determined that this transition point is regulated at least in part by the presence or absence of cargo (see the PhD dissertation of Ross TA Pedersen). Thus, it seems that budding yeast maximize the efficiency of cargo uptake by CME by waiting for cargo to arrive at pre-assembled early endocytic sites before proceeding to the late stage.

Crucially, these results may provide insight into the regulation of CME in other organisms. For instance, clathrin and the endocytic adaptor AP2 are typically used as markers for sites of CME in mammalian cells [24, 39, 40], and both exhibit variable lifetimes [41]. Analysis of the correlation between the lifetimes and intensities of these early proteins in relation to late-arriving proteins, rather than presenting lifetimes alone or averaging many sites together [24, 40, 41], might yield similar insights to those presented here. Having endocytic sites wait for cargo to accumulate before proceeding to the membrane deformation stage for the sake of energetic efficiency is a plausible general design principle.

3.5 Materials and Methods

Strains and yeast husbandry

All budding yeast strains were derived from the wild-type diploid DDY1102 and propagated using standard techniques [42]. C-terminal GFP fusions were originally constructed as described previously [43]. The strains used in this study are listed in Tables 3.1 and 3.2.

Live cell imaging

TIRFM imaging was performed on a Nikon Eclipse Ti2 inverted microscope with a Nikon CFI60 60× 1.49-NA Apo oil immersion TIRF objective and a Hamamatsu Orca-Flash 4.0 V2 sCMOS camera. GFP and mRFP/mCherry were excited using 488- and 561-nm lasers and detected using a Chroma HC TIRF Quad Dichroic (C-FL TIRF Ultra Hi S/N 405/488/561/638) and Chroma HC Quad emission filters BP 525/550 and BP 600/650, respectively. Channels were acquired sequentially. The system was controlled with Nikon Elements software and maintained at 25°C by an OkoLab environmental chamber. Frames were separated by 1 sec.

Image and data analysis

Tracking of endocytic sites was performed using the MATLAB package cmeAnalysis [24]. The red and green channels for each movie were tracked independently, and the centroid position over time for each site determined. These data were used as input in custom MATLAB scripts that associated colocalized tracks in the red and green channels while rejecting tracks that came within 350 nm of one another [40]. The fluorescence intensity for each spot was calculated as an integrated intensity within a circular region with a diameter of 7 pixels (756 nm), centered at the spot position determined by cmeAnalysis. The background fluorescence was calculated as the average fluorescence intensity of an annulus 2 pixels (216 nm) wide surrounding the circular region used to calculate the spot intensity.

Custom MATLAB scripts were then used to clean our dataset by rejecting tracks that fall into several categories: Sites with a low signal-to-noise (brightness not significantly above background) were excluded from further analysis. Tracks that began or terminated within 5 frames of the beginning or end of the movie were excluded so that only complete tracks were kept for analysis. Sites whose calculated background-subtracted intensity went below $-0.25\times$ the maximum intensity were excluded to prevent abnormally high background or presence of nearby sites from affecting intensity measurements. Finally, outliers in spot lifetime, fluorescence intensity, time to arrival, and time to disappearance (defined as more than $1.5\times$ the interquartile distance from the median value) were also excluded. This was done to exclude erroneous traces in which two distinct tracks had been inadvertently linked, where two sites overlapped and thus were substantially brighter, as well as erroneous putative colocalizations.

GFP maximum fluorescence intensity and the lifetimes and maximum intensities of the red reference proteins were fit to the lifetimes of the GFP-tagged protein of interest via simple linear regression. To compare the slopes of the fit across GFP-tagged proteins with differing brightnesses and lifetimes, the data were first normalized by dividing by their respective medians, which does not change the R^2 of the fit.

Reproducibility of experiments

Three independent datasets were acquired for each pair of GFP- and red fluorophore-tagged proteins. Endocytic sites from each of the (dozens) of cells in several fields of view were tracked simultaneously and pooled for analysis. As the results from each dataset were indistinguishable, they were pooled for further analysis. The number of tracked spots for each protein pair, which for each was in the hundreds or thousands, is presented in Tables 3.3-3.26.

Table 3.1: Strains used in this study

Name	Genotype	Source
DDY1102	*MATa/MATα his3-Δ200/his3-Δ200, leu2-3, 112/leu2-3, 112, ura3-52/ura3-52, ade2-1/ADE2, lys2-801/LYS2*	Drubin Lab
RPY49.1	*MATa his3-Δ200, leu2-3, 112, ura3-52, ABP1-mRFP::HIS3, SLA1-GFP::KanMX*	This study
RPY297.1	*MATa his3-Δ200, leu2-3, 112, ura3-52, ABP1-mRFP::HIS3, Bzz1-GFP::HIS3*	This study
RPY307.1	*MATa his3-Δ200, leu2-3, 112, ura3-52, ABP1-mRFP::HIS3, ARC15-GFP::KanMX*	This study
RPY313.1	*MATa his3-Δ200, leu2-3, 112, ura3-52, ABP1-mRFP::HIS3, RVS167-GFP::HIS3*	This study
RPY315.1	*MATa his3-Δ200, leu2-3, 112, ura3-52, ABP1-mRFP::HIS3, SLA2-GFP::HIS3*	This study
RPY317.1	*MATa his3-Δ200, leu2-3, 112, ura3-52, ABP1-mRFP::HIS3, ARK1-GFP::KanMX*	This study
RPY319.1	*MATa his3-Δ200, leu2-3, 112, ura3-52, ABP1-mRFP::HIS3, SAC6-GFP::HIS3*	This study
RPY331.1	*MATa his3-Δ200, leu2-3, 112, ura3-52, bar1Δ::NatR, EDE1-mRFP::KanMX, PAL1-GFP::HIS3*	This study
RPY343.1	*MATa his3-Δ200, leu2-3, 112, ura3-52, bar1Δ::NatR, EDE1-mRFP::HIS3, SYP1-GFP::KanMX*	This study
RPY345.1	*MATa his3-Δ200, leu2-3, 112, ura3-52, bar1Δ::NatR, EDE1-mRFP::KanMX, Hrr25-3xGFP::HIS3*	This study
RPY347.1	*MATa his3-Δ200, leu2-3, 112, ura3-52, bar1Δ::NatR, SLA1-mCherry::HIS3, PAL1-GFP::HIS3*	This study
RPY351.1	*MATa his3-Δ200, leu2-3, 112, ura3-52, bar1Δ::NatR, SLA1-mCherry::HIS3, APL1-GFP::HIS3*	This study
RPY353.1	*MATa his3-Δ200, leu2-3, 112, ura3-52, bar1Δ::NatR, SLA1-mCherry::HIS3, EDE1-GFP::HIS3*	This study

Table 3.2: Strains used in this study, continued

Name	Genotype	Source
RPY355.1	*MATa his3-Δ200, leu2-3, 112, ura3-52, bar1Δ::NatR, SLA1-mCherry::HIS3, SYP1-GFP::KanMX*	This study
RPY359.1	*MATa his3-Δ200, leu2-3, 112, ura3-52, bar1Δ::NatR, SLA1-mCherry::HIS3, Hrr25-3xGFP::HIS3*	This study
DDY3293	*MATα his3-Δ200, leu2-3, 112, ura3-52, ABP1-mRFP::HIS3, LAS17-GFP::HIS3*	Drubin lab
DDY5617	*MATa his3-Δ200, leu2-3, 112, ura3-52, ABP1-mRFP::HIS3, LAS17-GFP::HIS3*	Drubin lab, Sun et al. 2017
DDY3288	*MATa his3-Δ200, leu2-3, 112, ura3-52, ABP1-mRFP::HIS3, MYO5-GFP::URA3::KanMX*	Drubin lab
DDY5640	*MATa his3-Δ200, leu2-3, 112, ura3-52, ABP1-mRFP::HygMX, MYO5-GFP::HIS3*	Drubin lab, Sun et al. 2017
DDY3063	*MATα his3-Δ200, leu2-3, 112, ura3-52, ABP1-mRFP::HIS3, Pan1-GFP::HIS3*	Drubin lab
DDY3314	*MATa his3-Δ200, leu2-3, 112, ura3-52, ABP1-mRFP::HIS3, Pan1-GFP::KanMX*	Drubin lab
DDY3867	*MATα his3-Δ200, leu2-3, 112, ura3-52, ABP1-mRFP::HIS3, SYP1-GFP::KanMX*	Drubin lab, Stimpson et al. 2009
DDY3868	*MATa his3-Δ200, leu2-3, 112, ura3-52, ABP1-mRFP::HIS3, Ede1-GFP::HIS3*	Drubin lab, Stimpson et al. 2009
DDY3061	*MATα his3-Δ200, leu2-3, 112, ura3-52, ABP1-mRFP::HIS3, CLC1-GFP::HIS3*	Drubin lab
DDY5635	*MATa his3-Δ200, leu2-3, 112, ura3-52, ABP1-mRFP::HygMX, VRP1-GFP::HIS3*	Drubin lab, Sun et al. 2017
DDY3791	*MATa his3-Δ200, leu2-3, 112, ura3-52, ABP1-mRFP::HIS3, APL1-GFP::HIS3*	Drubin lab
DDY3837	*MATα his3-Δ200, leu2-3, 112, ura3-52, bar1Δ::LEU2, EDE1-mRFP::HIS3, APL1-GFP::HIS3*	Drubin lab

3.6 Supplementary Figures and Tables

Figure 3.6: Data for GFP-tagged proteins of interest imaged with reference protein Ede1-RFP. (A-C) Scatterplots of A) Syp1-GFP maximum intensity, B) Ede1-RFP lifetime, and C) Ede1-RFP maximum intensity vs. Syp1-GFP lifetime. (D-F) Scatterplots of D) Hrr25-GFP maximum intensity, E) Ede1-RFP lifetime, and F) Ede1-RFP maximum intensity vs. Hrr25-GFP lifetime. (G-I) Scatterplots of G) Pal1-GFP maximum intensity, H) Ede1-RFP lifetime, and H) Ede1-RFP maximum intensity vs. Pal1-GFP lifetime. (J-L) Scatterplots of J) Apl1-GFP maximum intensity, K) Ede1-RFP lifetime, and L) Ede1-RFP maximum intensity vs. Apl1-GFP lifetime. Color indicates the normalized data density in the neighborhood around the point. Red lines are linear fits to the data with the indicated R^2 value.
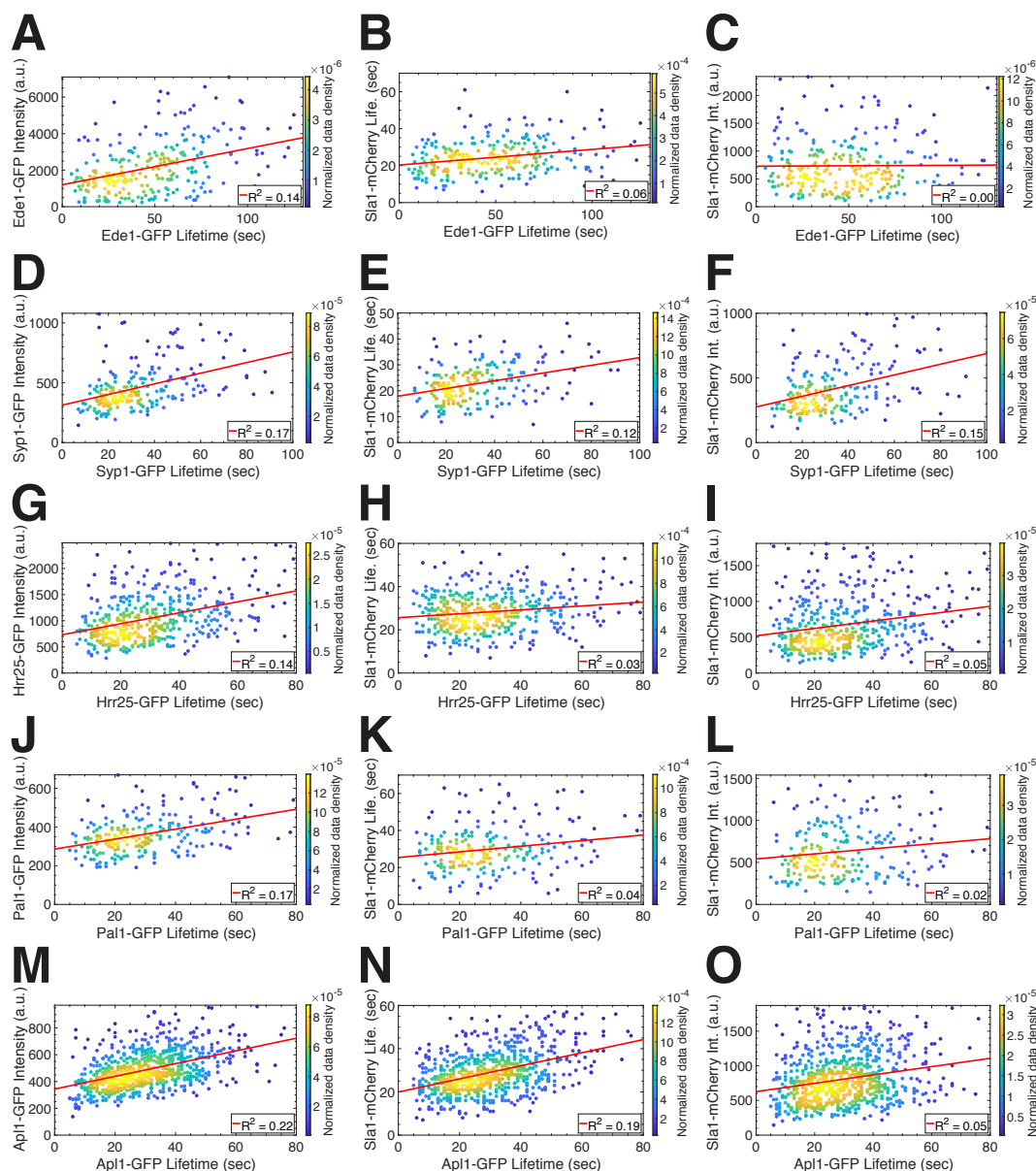
Figure 3.7: Data for GFP-tagged proteins of interest imaged with reference protein Sla1-mCherry. (A-C) Scatterplots of A) Ede1-GFP maximum intensity, B) Sla1-mCherry lifetime, and C) Sla1-mCherry maximum intensity vs. Ede1-GFP lifetime. (D-F) Scatterplots of D) Syp1-GFP maximum intensity, E) Sla1-mCherry lifetime, and F) Sla1-mCherry maximum intensity vs. Syp1-GFP lifetime. (G-I) Scatterplots of G) Hrr25-GFP maximum intensity, H) Sla1-mCherry lifetime, and H) Sla1-mCherry maximum intensity vs. Hrr25-GFP lifetime. (J-L) Scatterplots of J) Pal1-GFP maximum intensity, K) Sla1-mCherry lifetime, and L) Sla1-mCherry maximum intensity vs. Pal1-GFP lifetime. (M-O) Scatterplots of M) Apl1-GFP maximum intensity, N) Sla1-mCherry lifetime, and O) Sla1-mCherry maximum intensity vs. Apl1-GFP lifetime. Color indicates the normalized data density in the neighborhood around the point. Red lines are linear fits to the data with the indicated R^2 value.
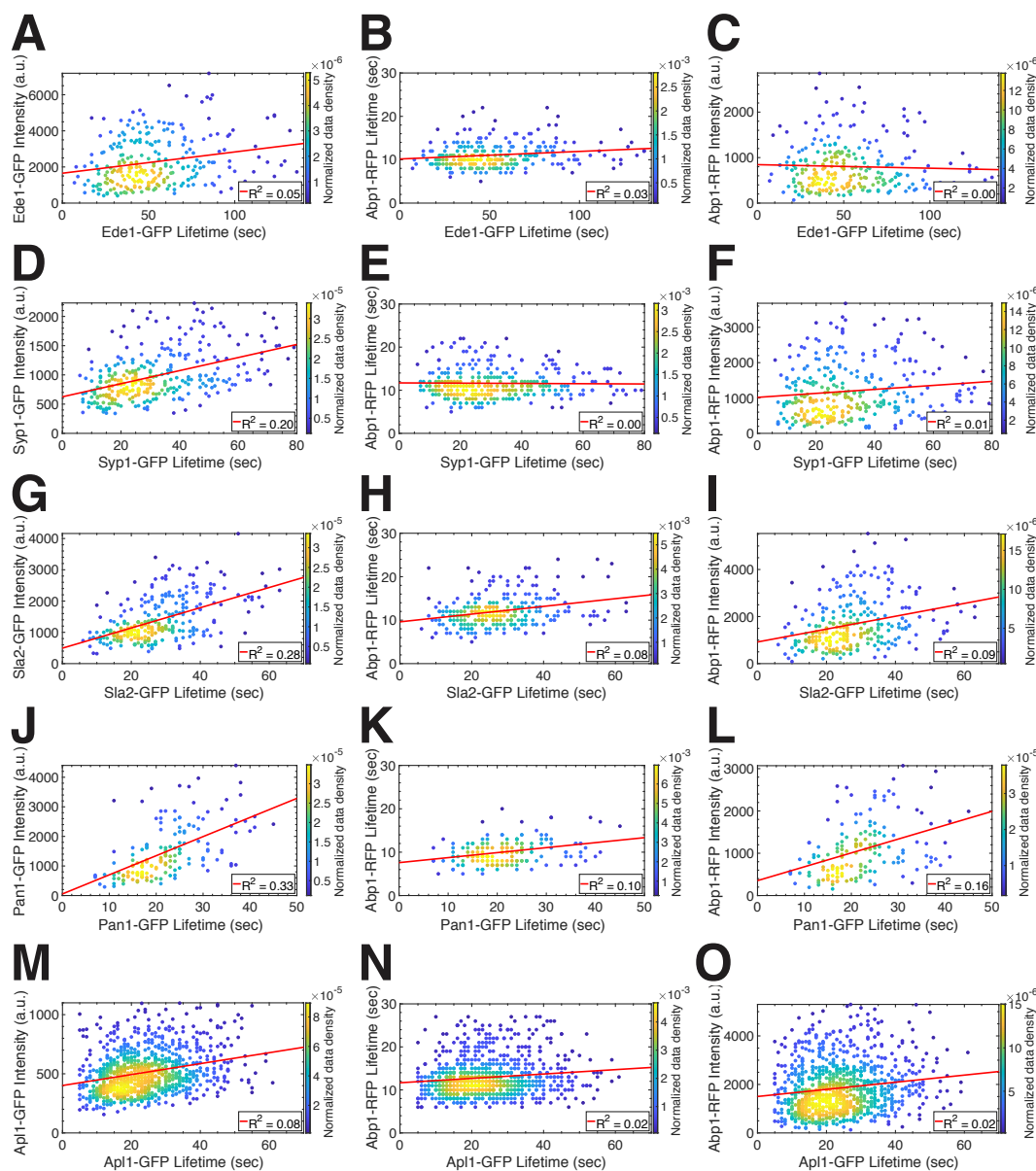
Figure 3.8: Data for GFP-tagged proteins of interest imaged with reference protein Abp1-RFP, Part 1. (A-C) Scatterplots of A) Ede1-GFP maximum intensity, B) Abp1-RFP lifetime, and C) Abp1-RFP maximum intensity vs. Ede1-GFP lifetime. (D-F) Scatterplots of D) Syp1-GFP maximum intensity, E) Abp1-RFP lifetime, and F) Abp1-RFP maximum intensity vs. Syp1-GFP lifetime. (G-I) Scatterplots of G) Sla2-GFP maximum intensity, H) Abp1-RFP lifetime, and H) Abp1-RFP maximum intensity vs. Sla2-GFP lifetime. (J-L) Scatterplots of J) Pan1-GFP maximum intensity, K) Abp1-RFP lifetime, and L) Abp1-RFP maximum intensity vs. Pan1-GFP lifetime. (M-O) Scatterplots of M) Apl1-GFP maximum intensity, N) Abp1-RFP lifetime, and O) Abp1-RFP maximum intensity vs. Apl1-GFP lifetime. Color indicates the normalized data density in the neighborhood around the point. Red lines are linear fits to the data with the indicated R^2 value.
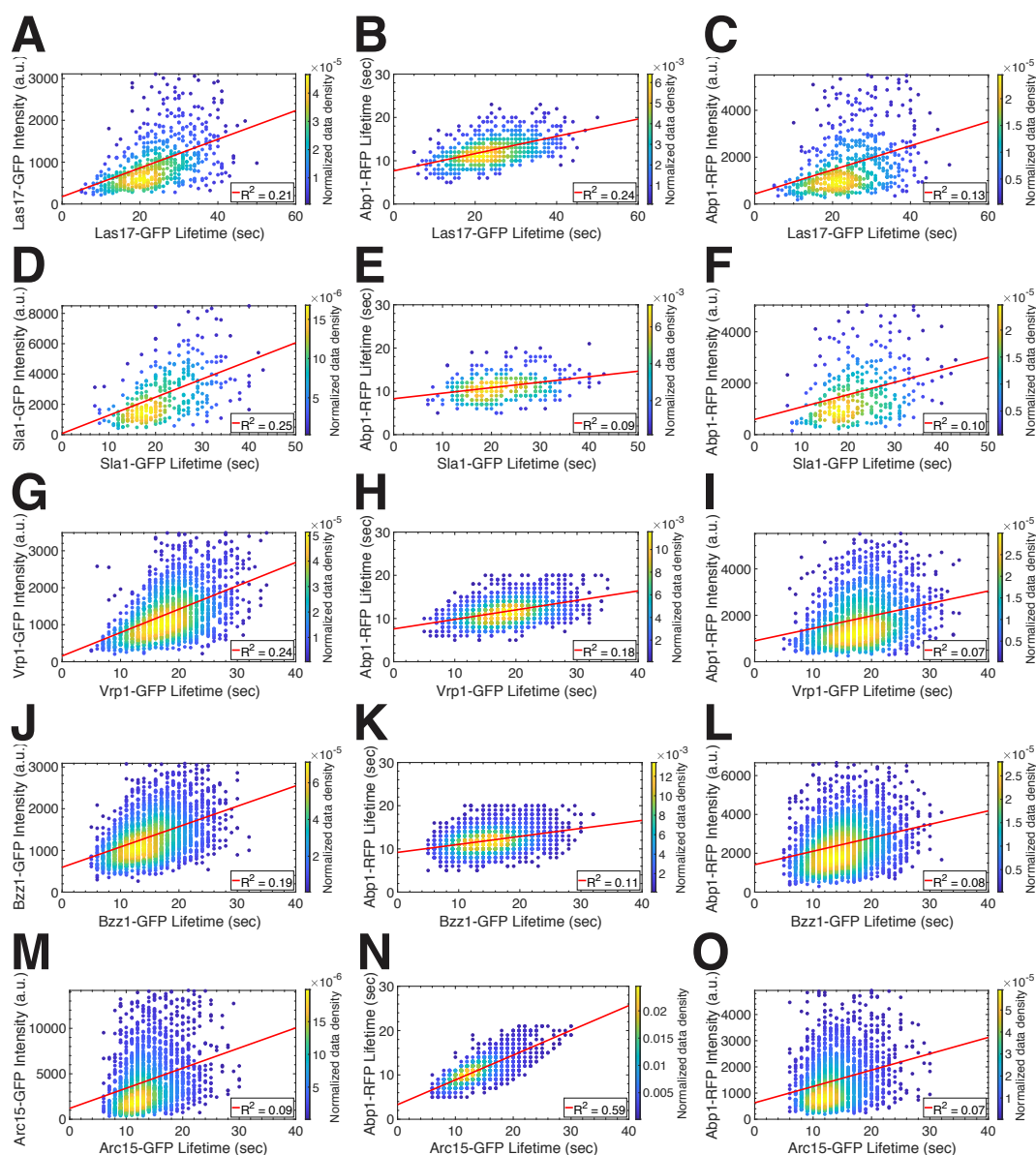
Figure 3.9: Data for GFP-tagged proteins of interest imaged with reference protein Abp1-RFP, Part 2. (A-C) Scatterplots of A) Las17-GFP maximum intensity, B) Abp1-RFP lifetime, and C) Abp1-RFP maximum intensity vs. Las17-GFP lifetime. (D-F) Scatterplots of D) Sla1-GFP maximum intensity, E) Abp1-RFP lifetime, and F) Abp1-RFP maximum intensity vs. Sla1-GFP lifetime. (G-I) Scatterplots of G) Vrp1-GFP maximum intensity, H) Abp1-RFP lifetime, and H) Abp1-RFP maximum intensity vs. Vrp1-GFP lifetime. (J-L) Scatterplots of J) Bzz1-GFP maximum intensity, K) Abp1-RFP lifetime, and L) Abp1-RFP maximum intensity vs. Bzz1-GFP lifetime. (M-O) Scatterplots of M) Arc15-GFP maximum intensity, N) Abp1-RFP lifetime, and O) Abp1-RFP maximum intensity vs. Arc15-GFP lifetime. Color indicates the normalized data density in the neighborhood around the point. Red lines are linear fits to the data with the indicated R^2 value.
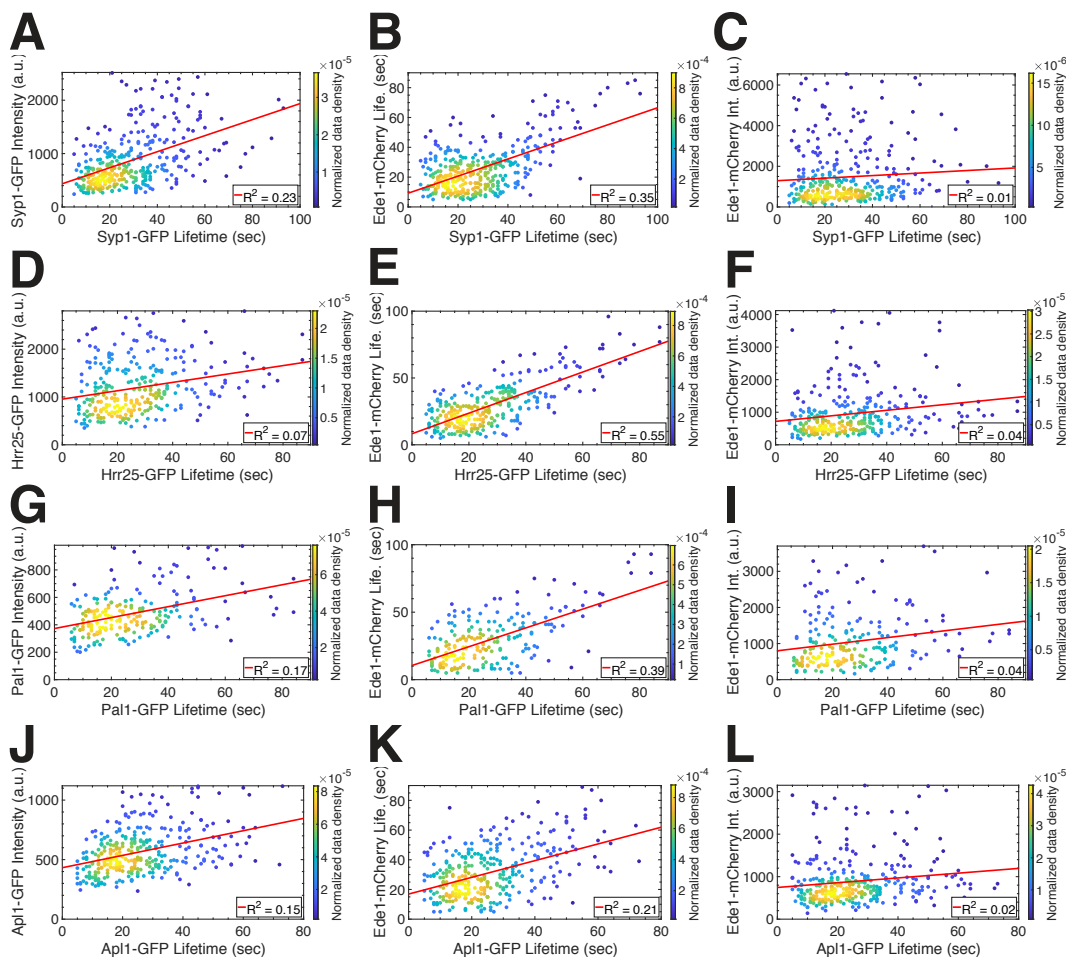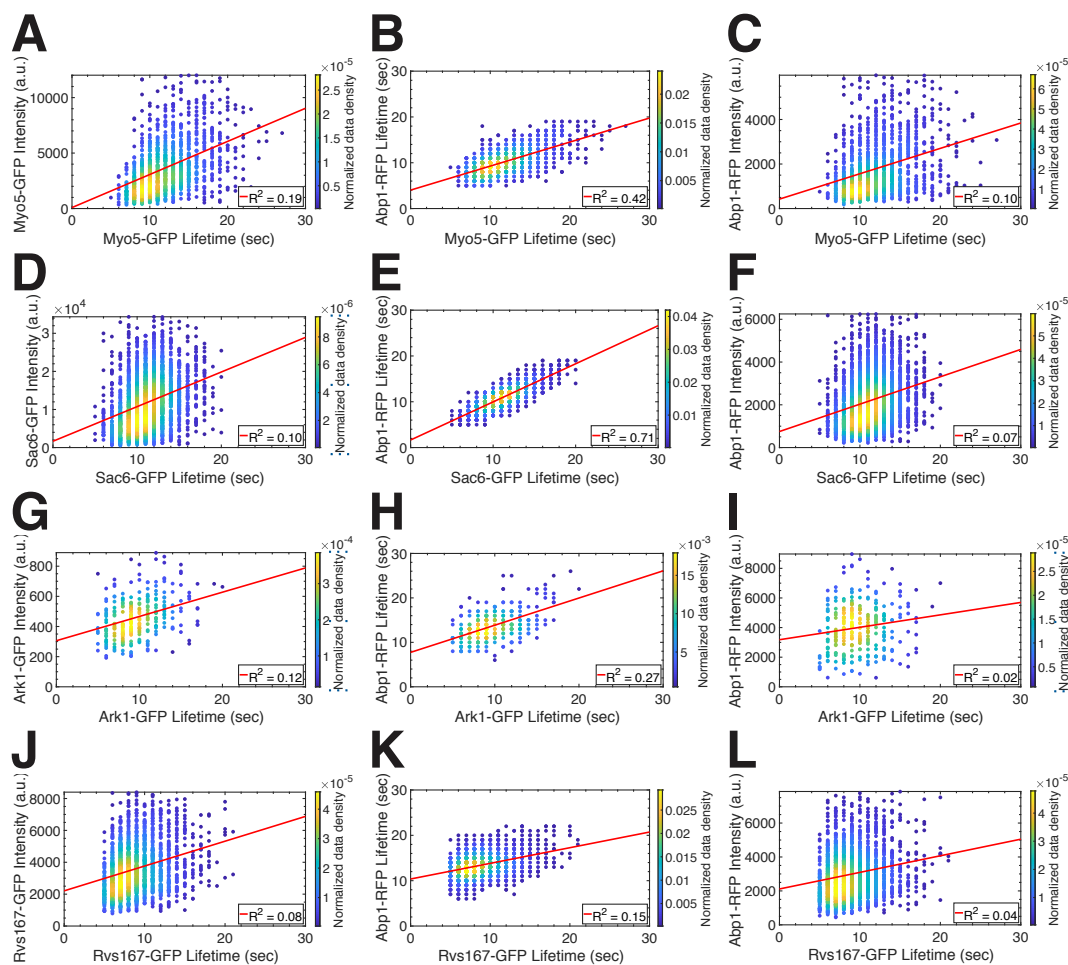
Figure 3.10: Data for GFP-tagged proteins of interest imaged with reference protein Abp1-RFP, Part 3. (A-C) Scatterplots of A) Myo5-GFP maximum intensity, B) Abp1-RFP lifetime, and C) Abp1-RFP maximum intensity vs. Myo5-GFP lifetime. (D-F) Scatterplots of D) Sac6-GFP maximum intensity, E) Abp1-RFP lifetime, and F) Abp1-RFP maximum intensity vs. Sac6-GFP lifetime. (G-I) Scatterplots of G) Ark1-GFP maximum intensity, H) Abp1-RFP lifetime, and H) Abp1-RFP maximum intensity vs. Ark1-GFP lifetime. (J-L) Scatterplots of J) Rvs167-GFP maximum intensity, K) Abp1-RFP lifetime, and L) Abp1-RFP maximum intensity vs. Rvs167-GFP lifetime. Color indicates the normalized data density in the neighborhood around the point. Red lines are linear fits to the data with the indicated R^2 value.

Table 3.3: Time to arrival of GFP-tagged proteins of interest colocalized with Ede1-RFP. All times in seconds. Goes with Figure 3.1D.

Protein of Interest ‖	N ‖	Median time to arrival	Mean	St Dev
Apl1 ‖	329 ‖	-7.0	-7.7	14.3
Hrr25 ‖	291 ‖	-1.0	-1.9	9.3
Pal1 ‖	207 ‖	-1.0	-2.6	12.0
Syp1 ‖	351 ‖	2.0	1.7	9.9

Table 3.4: Time to arrival of GFP-tagged proteins of interest colocalized with Sla1-mCherry. All times in seconds. Goes with Figure 3.1E.

Protein of Interest ‖	N ‖	Median time to arrival	Mean	St Dev
Apl1 ‖	728 ‖	3.0	3.8	12.1
Ede1 ‖	260 ‖	29.0	29.6	26.1
Hrr25 ‖	444 ‖	11.5	11.3	16.5
Pal1 ‖	229 ‖	3.0	6.0	15.7
Syp1 ‖	211 ‖	15.0	17.4	15.3

Table 3.5: Time to arrival of GFP-tagged proteins of interest colocalized with Abp1-RFP. All times in seconds. Goes with Figure 3.1F.

Protein of Interest	N	Median time to arrival	Mean	St Dev
Apl1	915	14.0	14.9	10.7
Arc15	1878	2.0	2.3	2.5
Ark1	260	-2.0	-2.3	2.2
Bzz1	2257	5.0	5.7	3.9
Ede1	252	42.5	48.0	27.9
Las17	582	14.0	14.1	6.9
Myo5	1202	1.0	1.5	1.8
Pan1	158	15.0	16.3	6.7
Rvs167	1802	-3.0	-3.1	2.0
Sac6	2512	0.0	0.0	1.1
Sla1	316	13.0	14.0	5.9
Sla2	274	18.0	18.9	9.9
Syp1	315	21.0	24.3	17.6
Vrp1	1604	9.0	9.0	4.4

Table 3.6: Lifetimes of GFP-tagged proteins of interest colocalized with Ede1-RFP. All times in seconds. Goes with Figure 3.2A.

Protein of Interest	N	Median Lifetime	Mean	St Dev	Coefficient of variation
Apl1	329	23.0	25.7	13.9	0.54
Hrr25	291	25.0	27.9	16.0	0.57
Pal1	207	24.0	27.6	16.5	0.60
Syp1	351	26.0	28.8	16.2	0.56

Table 3.7: Lifetimes of GFP-tagged proteins of interest colocalized with Sla1-mCherry. All times in seconds. Goes with Figure 3.2B.

Protein of Interest	N	Median Lifetime	Mean	St Dev	Coefficient of variation
Apl1	728	29.0	30.0	13.7	0.46
Ede1	260	48.5	49.5	27.4	0.55
Hrr25	444	28.0	30.5	15.8	0.52
Pal1	229	27.0	29.9	15.5	0.52
Syp1	211	30.0	33.3	17.2	0.52

Table 3.8: Lifetimes of GFP-tagged proteins of interest colocalized with Abp1-RFP. All times in seconds. Goes with Figure 3.2C.

Protein of Interest	N	Median Lifetime	Mean	St Dev	Coefficient of variation
Apl1	915	23.0	24.1	10.7	0.45
Arc15	1878	13.0	14.0	4.2	0.30
Ark1	260	9.0	9.9	3.0	0.30
Bzz1	2257	15.0	15.3	4.8	0.32
Ede1	252	49.0	54.2	26.7	0.49
Las17	582	24.0	24.4	8.3	0.34
Myo5	1202	12.0	12.3	3.6	0.29
Pan1	158	21.0	22.0	7.9	0.36
Rvs167	1802	8.0	9.1	2.9	0.32
Sac6	2512	11.0	11.3	2.5	0.22
Sla1	316	21.0	22.3	7.2	0.32
Sla2	274	26.0	28.0	11.2	0.40
Syp1	315	28.0	31.6	16.2	0.51
Vrp1	1604	18.0	18.6	5.3	0.29

Table 3.9: Maximum fluorescence intensity of GFP-tagged proteins of interest colocalized with Ede1-RFP.
All intensities are arbitrary units. Goes with Figure 3.2D.

Protein of Interest	N	Median maximum Intensity	Mean	St Dev
Apl1	329	517	565	186
Hrr25	291	1083	1199	542
Pal1	207	462	483	160
Syp1	351	694	868	508

Table 3.10: Maximum fluorescence intensity of GFP-tagged proteins of interest colocalized with Sla1-
mCherry. All intensities are arbitrary units. Goes with Figure 3.2E.

Protein of Interest	N	Median maximum Intensity	Mean	St Dev
Apl1	728	466	486	140
Ede1	260	1843	2183	1434
Hrr25	444	984	1052	441
Pal1	229	349	363	97
Syp1	211	419	461	183

Table 3.11: Maximum fluorescence intensity of GFP-tagged proteins of interest colocalized with Abp1-RFP.
All intensities are arbitrary units. Goes with Figure 3.2F.

Protein of Interest	N	Median maximum Intensity	Mean	St Dev
Apl1	915	484	513	180
Arc15	1878	3358	4291	3116
Ark1	260	457	465	142
Bzz1	2257	1241	1342	539
Ede1	252	1972	2292	1364
Las17	582	851	1012	615
Myo5	1202	3168	3743	2457
Pan1	158	1196	1479	896
Rvs167	1802	3378	3620	1558
Sac6	2512	10954	11916	7004
Sla1	316	2356	2749	1717
Sla2	274	1144	1399	687
Syp1	315	899	979	405
Vrp1	1604	1183	1329	681

Table 3.12: Lifetime of Ede1-RFP colocalized with GFP-tagged proteins of interest. All times in seconds.

Protein of Interest	N	Median Lifetime	Mean	St Dev
Apl1	329	29.0	31.4	16.9
Hrr25	291	27.0	29.7	16.6
Pal1	207	26.0	29.7	18.4
Syp1	351	23.0	25.7	15.7

Table 3.13: Lifetime of Sla1-mCherry colocalized with GFP-tagged proteins of interest. All times in seconds.

Protein of Interest	N	Median Lifetime	Mean	St Dev
Apl1	728	28.0	29.0	9.6
Ede1	260	24.0	24.5	9.2
Hrr25	444	28.0	28.4	8.9
Pal1	229	29.0	29.9	11.8
Syp1	211	22.0	22.8	7.3

Table 3.14: Lifetime of Abp1-RFP colocalized with GFP-tagged proteins of interest. All times in seconds.

Protein of Interest	N	Median Lifetime	Mean	St Dev
Apl1	915	12.0	12.9	4.2
Arc15	1878	11.0	11.1	3.0
Ark1	260	13.0	13.8	3.6
Bzz1	2257	12.0	12.0	2.7
Ede1	252	10.5	11.1	2.9
Las17	582	12.0	12.5	3.3
Myo5	1202	10.0	10.5	2.9
Pan1	158	10.0	10.1	2.8
Rvs167	1802	13.0	13.5	2.5
Sac6	2512	11.0	11.0	2.5
Sla1	316	11.0	11.1	3.0
Sla2	274	12.0	12.1	3.5
Syp1	315	11.0	11.6	3.4
Vrp1	1604	11.0	11.7	2.8

Table 3.15: Maximum fluorescence intensity of Ede1-RFP colocalized with GFP-tagged proteins of interest. All intensities are in arbitrary units.

Protein of Interest	N	Median maximum Intensity	Mean	St Dev
Apl1	329	727	890	562
Hrr25	291	748	956	720
Pal1	207	847	1052	730
Syp1	351	938	1473	1386

Table 3.16: Maximum fluorescence intensity of Sla1-mCherry colocalized with GFP-tagged proteins of interest. All intensities are in arbitrary units.

Protein of Interest	N	Median maximum Intensity	Mean	St Dev
Apl1	728	742	807	351
Ede1	260	629	735	455
Hrr25	444	587	676	357
Pal1	229	563	632	302
Syp1	211	366	413	182

Table 3.17: Maximum fluorescence intensity of Abp1-RFP colocalized with GFP-tagged proteins of interest. All intensities are in arbitrary units.

Protein of Interest	N	Median maximum Intensity	Mean	St Dev
Apl1	915	1651	1857	1055
Arc15	1878	1253	1501	954
Ark1	260	3985	4013	1675
Bzz1	2257	2270	2473	1211
Ede1	252	666	802	520
Las17	582	1285	1684	1182
Myo5	1202	1442	1821	1273
Pan1	158	937	1075	653
Rvs167	1802	2760	3002	1415
Sac6	2512	2006	2195	1190
Sla1	316	1374	1666	1091
Sla2	274	1410	1685	1044
Syp1	315	1010	1196	770
Vrp1	1604	1626	1897	1088

Table 3.18: Fit statistics, GFP-tagged protein of interest (colocalized with Ede1-RFP) maximum fluorescence intensity vs. lifetime with 95% confidence intervals. Goes with Figure 3.3D.

Protein of Interest	N	Slope	Lower	Upper	R^2	Lower	Upper
Apl1	329	0.23	0.17	0.29	0.15	0.08	0.23
Hrr25	291	0.20	0.11	0.29	0.07	0.02	0.13
Pal1	207	0.21	0.14	0.27	0.17	0.09	0.27
Syp1	351	0.56	0.45	0.67	0.23	0.15	0.31

Table 3.19: Fit statistics, GFP-tagged protein of interest (colocalized with Sla1-mCherry) maximum fluorescence intensity vs. lifetime with 95% confidence intervals. Goes with Figure 3.3E.

Protein of Interest	N	Slope	Lower	Upper	R^2	Lower	Upper
Apl1	728	0.30	0.25	0.34	0.22	0.16	0.27
Ede1	260	0.52	0.37	0.68	0.14	0.07	0.23
Hrr25	444	0.30	0.23	0.37	0.14	0.09	0.21
Pal1	229	0.20	0.14	0.26	0.17	0.09	0.26
Syp1	211	0.32	0.22	0.41	0.17	0.09	0.27

Table 3.20: Fit statistics, GFP-tagged protein of interest (colocalized with Abp1-RFP) maximum fluorescence intensity vs. lifetime with 95% confidence intervals. Goes with Figure 3.3F.

Protein of Interest	N	Slope	Lower	Upper	R^2	Lower	Upper
Apl1	915	0.22	0.17	0.27	0.08	0.05	0.11
Arc15	1878	0.86	0.73	0.98	0.09	0.06	0.11
Ark1	260	0.32	0.21	0.42	0.12	0.05	0.20
Bzz1	2257	0.59	0.54	0.64	0.19	0.16	0.22
Ede1	252	0.29	0.14	0.45	0.05	0.01	0.12
Las17	582	0.97	0.82	1.12	0.21	0.16	0.28
Myo5	1202	1.13	1.00	1.26	0.19	0.15	0.23
Pan1	158	1.14	0.88	1.39	0.33	0.21	0.45
Rvs167	1802	0.37	0.31	0.43	0.08	0.06	0.11
Sac6	2512	0.91	0.81	1.02	0.10	0.08	0.13
Sla1	316	1.07	0.86	1.27	0.25	0.17	0.33
Sla2	274	0.73	0.59	0.88	0.28	0.19	0.37
Syp1	315	0.35	0.27	0.43	0.20	0.13	0.28
Vrp1	1604	0.96	0.88	1.04	0.24	0.21	0.28

Table 3.21: Fit statistics, Ede1-RFP lifetime vs. GFP-tagged protein of interest lifetime with 95% confidence intervals. Goes with Figure 3.4D.

Protein of Interest	N	Slope	Lower	Upper	R^2	Lower	Upper
Apl1	329	0.45	0.35	0.54	0.21	0.14	0.30
Hrr25	291	0.71	0.64	0.79	0.55	0.47	0.62
Pal1	207	0.64	0.53	0.75	0.39	0.29	0.49
Syp1	351	0.65	0.55	0.74	0.35	0.27	0.43

Table 3.22: Fit statistics, Sla1-mCherry lifetime vs. GFP-tagged protein of interest lifetime with 95% confidence intervals. Goes with Figure 3.4E.

Protein of Interest	N	Slope	Lower	Upper	R^2	Lower	Upper
Apl1	728	0.31	0.27	0.36	0.19	0.14	0.24
Ede1	260	0.17	0.09	0.25	0.06	0.02	0.13
Hrr25	444	0.09	0.04	0.14	0.03	0.00	0.06
Pal1	229	0.14	0.05	0.23	0.04	0.01	0.10
Syp1	211	0.20	0.13	0.28	0.12	0.05	0.21

Table 3.23: Fit statistics, Abp1-RFP lifetime vs. GFP-tagged protein of interest lifetime with 95% confidence intervals. Goes with Figure 3.4F.

Protein of Interest	N	Slope	Lower	Upper	R^2	Lower	Upper
Apl1	915	0.10	0.05	0.15	0.02	0.00	0.04
Arc15	1878	0.66	0.63	0.69	0.59	0.56	0.61
Ark1	260	0.42	0.34	0.51	0.27	0.18	0.36
Bzz1	2257	0.23	0.20	0.26	0.11	0.09	0.14
Ede1	252	0.08	0.02	0.14	0.03	0.00	0.08
Las17	582	0.40	0.34	0.46	0.24	0.19	0.31
Myo5	1202	0.63	0.59	0.67	0.42	0.38	0.46
Pan1	158	0.24	0.13	0.35	0.10	0.03	0.21
Rvs167	1802	0.21	0.19	0.24	0.15	0.12	0.18
Sac6	2512	0.83	0.81	0.85	0.71	0.69	0.73
Sla1	316	0.24	0.16	0.33	0.09	0.04	0.16
Sla2	274	0.19	0.11	0.27	0.08	0.03	0.15
Syp1	315	-0.01	-0.07	0.05	0.00	0.02	0.01
Vrp1	1604	0.36	0.32	0.40	0.18	0.14	0.21

Table 3.24: Fit statistics, Ede1-RFP maximum fluorescence intensity vs. GFP-tagged protein of interest lifetime with 95% confidence intervals. Goes with Figure 3.5D.

Protein of Interest	N	Slope	Lower	Upper	R^2	Lower	Upper
Apl1	329	0.18	0.04	0.32	0.02	0.00	0.06
Hrr25	291	0.28	0.11	0.46	0.04	0.01	0.09
Pal1	207	0.26	0.09	0.43	0.04	0.01	0.11
Syp1	351	0.17	-0.08	0.42	0.01	0.00	0.03

Table 3.25: Fit statistics, Sla1-mCherry maximum fluorescence intensity vs. GFP-tagged protein of interest lifetime with 95% confidence intervals. Goes with Figure 3.5E.

Protein of Interest	N	Slope	Lower	Upper	R^2	Lower	Upper
Apl1	728	0.23	0.16	0.31	0.05	0.03	0.09
Ede1	260	0.01	-0.14	0.17	0.00	0.01	0.02
Hrr25	444	0.25	0.15	0.34	0.05	0.02	0.10
Pal1	229	0.14	0.02	0.27	0.02	0.00	0.08
Syp1	211	0.34	0.23	0.45	0.15	0.07	0.25

Table 3.26: Fit statistics, Abp1-RFP maximum fluorescence intensity vs. GFP-tagged protein of interest lifetime with 95% confidence intervals. Goes with Figure 3.5F.

Protein of Interest	N	Slope	Lower	Upper	R^2	Lower	Upper
Apl1	915	0.20	0.12	0.29	0.02	0.01	0.05
Arc15	1878	0.65	0.54	0.75	0.07	0.05	0.10
Ark1	260	0.19	0.04	0.34	0.02	0.00	0.07
Bzz1	2257	0.46	0.39	0.52	0.08	0.06	0.10
Ede1	252	-0.06	-0.24	0.12	0.00	0.03	0.01
Las17	582	0.96	0.76	1.16	0.13	0.08	0.18
Myo5	1202	0.95	0.79	1.11	0.10	0.07	0.14
Pan1	158	0.73	0.47	1.00	0.16	0.07	0.27
Rvs167	1802	0.28	0.22	0.35	0.04	0.02	0.06
Sac6	2512	0.70	0.60	0.80	0.07	0.05	0.09
Sla1	316	0.74	0.49	0.98	0.10	0.05	0.17
Sla2	274	0.50	0.31	0.70	0.09	0.03	0.16
Syp1	315	0.16	0.01	0.30	0.01	0.00	0.05
Vrp1	1604	0.59	0.49	0.70	0.07	0.05	0.09

References

1. McMahon, H. T. & Boucrot, E. Molecular mechanism and physiological functions of clathrin-mediated endocytosis. *Nature reviews Molecular cell biology* **12,** 517 (2011).

2. Lu, R., Drubin, D. G. & Sun, Y. Clathrin-mediated endocytosis in budding yeast at a glance. *J Cell Sci* **129,** 1531–1536 (2016).

3. Kaksonen, M., Sun, Y. & Drubin, D. G. A pathway for association of receptors, adaptors, and actin during endocytic internalization. *Cell* **115,** 475–487 (2003).

4. Kaksonen, M., Toret, C. P. & Drubin, D. G. A modular design for the clathrin-and actin-mediated endocytosis machinery. *Cell* **123,** 305–320 (2005).

5. Sun, Y., Martin, A. C. & Drubin, D. G. Endocytic internalization in budding yeast requires coordinated actin nucleation and myosin motor activity. *Developmental cell* **11,** 33–46 (2006).

6. Picco, A., Mund, M., Ries, J., Nedelec, F. & Kaksonen, M. Visualizing the functional architecture of the endocytic machinery. *Elife* **4,** e04535 (2015).

7. Kaksonen, M., Toret, C. P. & Drubin, D. G. Harnessing actin dynamics for clathrin-mediated endocytosis. *Nature reviews Molecular cell biology* **7,** 404–414 (2006).

8. Boettner, D. R., Chi, R. J. & Lemmon, S. K. Lessons from yeast for clathrin-mediated endocytosis. *Nature cell biology* **14,** 2 (2012).

9. Kaksonen, M. & Roux, A. Mechanisms of clathrin-mediated endocytosis. *Nature Reviews Molecular Cell Biology* **19,** 313 (2018).

10. Stimpson, H. E., Toret, C. P., Cheng, A. T., Pauly, B. S. & Drubin, D. G. Early-arriving Syp1p and Ede1p function in endocytic site placement and formation in budding yeast. *Molecular biology of the cell* **20,** 4640–4651 (2009).

11. Carroll, S. Y. *et al.* Analysis of yeast endocytic site formation and maturation through a regulatory transition point. *Molecular biology of the cell* **23,** 657–668 (2012).

12. Peng, Y. *et al.* Casein kinase 1 promotes initiation of clathrin-mediated endocytosis. *Developmental cell* **32,** 231–240 (2015).

13. Kukulski, W., Schorb, M., Kaksonen, M. & Briggs, J. A. Plasma membrane reshaping during endocytosis is revealed by time-resolved electron tomography. *Cell* **150,** 508–520 (2012).

14. Lewellyn, E. B. *et al.* An engineered minimal WASP-myosin fusion protein reveals essential functions for endocytosis. *Developmental cell* **35,** 281–294 (2015).

15. Kishimoto, T. *et al.* Determinants of endocytic membrane geometry, stability, and scission. *Proceedings of the National Academy of Sciences* **108,** E979–E988 (2011).

16. Cope, M. J. T., Yang, S., Shang, C. & Drubin, D. G. Novel protein kinases Ark1p and Prk1p associate with and regulate the cortical actin cytoskeleton in budding yeast. *The Journal of cell biology* **144,** 1203–1218 (1999).

17. Payne, G. S., Baker, D., van Tuinen, E. & Schekman, R. Protein transport to the vacuole and receptor-mediated endocytosis by clathrin heavy chain-deficient yeast. *The Journal of Cell Biology* **106,** 1453–1461 (1988).

18. Brach, T., Godlee, C., Moeller-Hansen, I., Boeke, D. & Kaksonen, M. The initiation of clathrin-mediated endocytosis is mechanistically highly flexible. *Current Biology* **24,** 548–554 (2014).

19. Layton, A. T. *et al.* Modeling vesicle traffic reveals unexpected consequences for Cdc42p-mediated polarity establishment. *Current Biology* **21,** 184–194 (2011).

20. Weinberg, J. S. & Drubin, D. G. Regulation of clathrin-mediated endocytosis by dynamic ubiquitination and deubiquitination. *Current Biology* **24,** 951–959 (2014).

21. Galletta, B. J., Chuang, D. Y. & Cooper, J. A. Distinct roles for Arp2/3 regulators in actin assembly and endocytosis. *PLoS biology* **6,** e1 (2008).

22. Sun, Y. *et al.* Switch-like Arp2/3 activation upon WASP and WIP recruitment to an apparent threshold level by multivalent linker proteins in vivo. *Elife* **6,** e29140 (2017).

23. Merrifield, C. J., Feldman, M. E., Wan, L. & Almers, W. Imaging actin and dynamin recruitment during invagination of single clathrin-coated pits. *Nature cell biology* **4,** 691 (2002).

24. Aguet, F., Antonescu, C. N., Mettlen, M., Schmid, S. L. & Danuser, G. Advances in analysis of low signal-to-noise images link dynamin and AP2 to the functions of an endocytic checkpoint. *Developmental cell* **26,** 279–291 (2013).

25. Adams, A. E., Botstein, D. & Drubin, D. G. Requirement of yeast fimbrin for actin organization and morphogenesis in vivo. *Nature* **354,** 404–408 (1991).

26. Carroll, S. Y. *et al.* A yeast killer toxin screen provides insights into a/b toxin entry, trafficking, and killing mechanisms. *Developmental cell* **17,** 552–560 (2009).

27. Youn, J.-Y. *et al.* Dissecting BAR domain function in the yeast Amphiphysins Rvs161 and Rvs167 during endocytosis. *Molecular biology of the cell* **21,** 3054–3069 (2010).

28. Reed, G. F., Lynn, F. & Meade, B. D. Use of coefficient of variation in assessing variability of quantitative assays. *Clin. Diagn. Lab. Immunol.* **9,** 1235–1239 (2002).

29. Axelrod, D. in *Methods in cell biology* 245–270 (Elsevier, 1989).

30. Mund, M. *et al.* Systematic nanoscale analysis of endocytosis links efficient vesicle formation to patterned actin nucleation. *Cell* **174,** 884–896 (2018).

31. Sirotkin, V., Berro, J., Macmillan, K., Zhao, L. & Pollard, T. D. Quantitative analysis of the mechanism of endocytic actin patch assembly and disassembly in fission yeast. *Molecular biology of the cell* **21,** 2894–2904 (2010).

32. Holland, D. O. & Johnson, M. E. Stoichiometric balance of protein copy numbers is measurable and functionally significant in a protein-protein interaction network for yeast endocytosis. *PLoS computational biology* **14,** e1006022 (2018).

33. Glantz, S. A. & Slinker, B. K. *Primer of applied regression and analysis of variance* **Sirsi) i9780070234079** (1990).

34. Pedersen, R. T. & Drubin, D. G. Type I myosins anchor actin assembly to the plasma membrane during clathrin-mediated endocytosis. *J Cell Biol* **218,** 1138–1147 (2019).

35. Sun, Y., Leong, N. T., Wong, T. & Drubin, D. G. A Pan1/End3/Sla1 complex links Arp2/3-mediated actin assembly to sites of clathrin-mediated endocytosis. *Molecular biology of the cell* **26,** 3841–3856 (2015).

36. Aghamohammadzadeh, S. & Ayscough, K. R. Differential requirements for actin during yeast and mammalian endocytosis. *Nature cell biology* **11,** 1039 (2009).

37. Basu, R., Munteanu, E. L. & Chang, F. Role of turgor pressure in endocytosis in fission yeast. *Molecular biology of the cell* **25,** 679–687 (2014).

38. Rodal, A. A., Manning, A. L., Goode, B. L. & Drubin, D. G. Negative regulation of yeast WASp by two SH3 domain-containing proteins. *Current Biology* **13,** 1000–1008 (2003).

39. Doyon, J. B. *et al.* Rapid and efficient clathrin-mediated endocytosis revealed in genome-edited mammalian cells. *Nature cell biology* **13,** 331 (2011).

40. Hong, S. H., Cortesio, C. L. & Drubin, D. G. Machine-learning-based analysis in genome-edited cells reveals the efficiency of clathrin-mediated endocytosis. *Cell reports* **12,** 2121–2130 (2015).

41. Taylor, M. J., Perrais, D. & Merrifield, C. J. A high precision survey of the molecular dynamics of mammalian clathrin-mediated endocytosis. *PLoS biology* **9,** e1000604 (2011).

42. Amberg, D. C. & Strathern, J. N. *Methods in yeast genetics: a Cold Spring Harbor Laboratory course manual* (CSHL press, 2005).

43. Longtine, M. S. *et al.* Additional modules for versatile and economical PCR-based gene deletion and modification in Saccharomyces cerevisiae. *Yeast* **14,** 953–961 (1998).

Chapter 4

Conclusions and Outlook

In Chapters 2 and 3, I sought to uncover general principles by which cells ensure the robustness and efficiency of clathrin-mediated endocytosis. In Chapter 2, I found that redundant but complementary methods for deforming the membrane can confer robustness in the face of challenging mechanical environments. In Chapter 3, I provided quantitative evidence for a regulatory transition point that appears to ensure efficiency of cargo uptake on a per endocytic site basis. These two insights contribute to the growing movement towards the study of cell biology on a quantitative and physical basis [1]. Crucially, these studies are only now possible because the tools of molecular biology, biochemistry, microscopy, and biophysics have advanced to the point where quantitative modeling and experiments can inform one another in a meaningful way.

4.1 Feedback between modeling and experiments

A seminal study in the field of clathrin-mediated endocytosis illustrating the value of modeling in biology is that of Liu, Sun, Drubin & Oster, 2009 [2]. In this paper, the authors combine membrane mechanics with modeling of curvature-based recruitment of proteins to fit the fluorescence intensity curves from microscopy data of budding yeast CME. The groundwork for this study was laid in a series of papers [3–6] that mapped out the CME pathway and measured the relative abundance and position of endocytic proteins over time. Like any good model, this one made experimentally testable predictions as to the expected phenotypes of various perturbations to the endocytic machinery.

New advances in the ability to calibrate fluorescence intensity to count numbers of molecules at endocytic sites [7, 8], new techniques to visualize the architecture of the endocytic machinery [9, 10] as well as advances in modeling [11–13], have opened the door to a new era of using theory to inform experiments and vice versa. For example, measurements of high turgor pressure in yeast [14–16] have led to investigations of how much force is needed to overcome this barrier to invagination [17], whether force from actin assembly is able to provide enough force to do so [18–20], and whether cells could employ alternate strategies

to locally reduce turgor pressure near endocytic sites [21]. Knowing the approximate numbers of molecules at endocytic sites has led to the realization that the coat is exceptionally crowded, and thus the prediction, now confirmed by superresolution microscopy techniques [9, 10], that late arriving proteins must bind at the edges of the coat [22]. Other modeling efforts have been focused on how actin is assembled and disassembled at endocytic sites [19, 23]. These studies have sought to incorporate the biochemical feedback mechanisms that drive successive recruitment of downstream proteins, which feed back on the abundance of early protein. Future modeling efforts will likely seek to add ever more complexity, incorporating the mechanical forces at play, the geometry of the membrane, and the biochemical interactions that all contribute during CME.

My own modeling efforts, as detailed in Chapter 2, were initially only meant to be a first step in constructing such a model. However, models need not be unnecessarily complex to explain biological phenomena as highlighted by the fact that I was able to uncover novel insights into how the mechanical robustness of CME is achieved simply through the implementation of a somewhat more versatile continuum modeling framework [24]. Despite this caution, I expect that models incorporating all of the known parameters of CME including protein numbers, resistance from membrane tension and turgor pressure, etc. will soon be capable of making novel, testable predictions how the feedback between protein recruitment dynamics and membrane mechanics dictates progression through the pathway.

4.2 Big data in biology and CME

Over the past couple of decades, tremendous advances have been made in microscopy that have massively increased the quantity and quality of imaging data. The study of clathrin-mediated endocytosis has already benefited enormously from this explosion in data. The high signal-to-noise capabilities of TIRF microscopy have allowed for the visualization of dynamin at endocytic sites long before would have previously been expected [25] as well as for the examination of recruitment dynamics of both early endocytic proteins and dynamin [26, 27]. Superresolution microscopy [9] and correlated light and electron microscopy [10, 28] have provided detailed views of the location of proteins at endocytic sites at various stages of membrane deformation. All of these advances have required the development or application of new quantitative analysis tools.

Perhaps the most important development over the last decade is the invention and refinement of lattice light-sheet microscopy [29]. This, coupled with genome editing capabilities [30, 31] allows for an unperturbed look at CME dynamics within an entire organism [32] or in an organoid grown from human stem cells [33]. These data sets will allow the field to move beyond looking at dynamics of CME in cells adhered to glass substrates to looking at the dynamics in a natural physiological state. This will then allow for direct observation of how CME is altered in various disease states. Presently, our capability to generate these data sets outstrips our ability to analyze them. Typical movies taken via lattice light-sheet microscopy reach into the hundreds of gigabytes, and data sets of many terabytes are now

being produced [32]. New tools are needed to work with and analyze these data [33] in order to unlock the promise of this transformative new imaging modality which is ushering in the era of big data in cell biology.

Beyond the extensive new quantitative data that are sure to come, there is almost certainly more to be learned from the dataset that I collected for the work presented in Chapter 3. In particular, reporting only the maximum fluorescence intensity ignores features like the shape of the trace, time to the peak intensity, fluctuations in the intensity, etc. Perhaps further analysis of these types of features would give new insight into how progression through CME is regulated.

4.3 Final thoughts

CME is a process that has fascinated biologists for over 40 years [34]. Decades of work were spent identifying the genes involved in regulating this process and then characterizing the function, timing, and interactions of the proteins encoded by these genes. This rich history has laid the foundation for the study of CME from the point of view of the physics involved or how the system of protein interactions confers robustness and efficiency to the process. This is a particularly exciting time as the field has now progressed from asking "which" and "when" questions (Which genes are involved? When does each protein arrive at endocytic sites?) to "how" and "why" questions (How are robustness and efficiency achieved? Why does a particular mutation cause a particular phenotype?). I feel certain that, given both the complexity and the conceptual simplicity of the pathway, CME will continue to be a productive area of study for another 40 years.

References

1. Howard, J. Quantitative cell biology: the essential role of theory. *Molecular biology of the cell* **25,** 3438–3440 (2014).

2. Liu, J., Sun, Y., Drubin, D. G. & Oster, G. F. The mechanochemistry of endocytosis. *PLoS biology* **7,** e1000204 (2009).

3. Kaksonen, M., Sun, Y. & Drubin, D. G. A pathway for association of receptors, adaptors, and actin during endocytic internalization. *Cell* **115,** 475–487 (2003).

4. Kaksonen, M., Toret, C. P. & Drubin, D. G. A modular design for the clathrin-and actin-mediated endocytosis machinery. *Cell* **123,** 305–320 (2005).

5. Sun, Y., Martin, A. C. & Drubin, D. G. Endocytic internalization in budding yeast requires coordinated actin nucleation and myosin motor activity. *Developmental cell* **11,** 33–46 (2006).

6. Sun, Y., Carroll, S., Kaksonen, M., Toshima, J. Y. & Drubin, D. G. PtdIns (4, 5) P2 turnover is required for multiple stages during clathrin-and actin-dependent endocytic internalization. *The Journal of cell biology* **177,** 355–367 (2007).

7. Sirotkin, V., Berro, J., Macmillan, K., Zhao, L. & Pollard, T. D. Quantitative analysis of the mechanism of endocytic actin patch assembly and disassembly in fission yeast. *Molecular biology of the cell* **21,** 2894–2904 (2010).

8. Picco, A., Mund, M., Ries, J., Nedelec, F. & Kaksonen, M. Visualizing the functional architecture of the endocytic machinery. *Elife* **4,** e04535 (2015).

9. Mund, M. *et al.* Systematic nanoscale analysis of endocytosis links efficient vesicle formation to patterned actin nucleation. *Cell* **174,** 884–896 (2018).

10. Sochacki, K. A., Dickey, A. M., Strub, M.-P. & Taraska, J. W. Endocytic proteins are partitioned at the edge of the clathrin lattice in mammalian cells. *Nature cell biology* **19,** 352 (2017).

11. Agrawal, A. & Steigmann, D. J. Modeling protein-mediated morphology in biomembranes. *Biomechanics and modeling in mechanobiology* **8,** 371 (2009).

12. Nedelec, F. & Foethke, D. Collective Langevin dynamics of flexible cytoskeletal fibers. *New Journal of Physics* **9,** 427 (2007).

13. Schöneberg, J. & Noé, F. ReaDDy-a software for particle-based reaction-diffusion dynamics in crowded cellular environments. *PloS one* **8,** e74261 (2013).

14. Schaber, J. *et al.* Biophysical properties of Saccharomyces cerevisiae and their relationship with HOG pathway activation. *European Biophysics Journal* **39,** 1547–1556 (2010).

15. De Mara on, I., Marechal, P.-A. & Gervais, P. Passive response of Saccharomyces cerevisiae to osmotic shifts: cell volume variations depending on the physiological state. *Biochemical and biophysical research communications* **227,** 519–523 (1996).

16. Minc, N., Boudaoud, A. & Chang, F. Mechanical forces of fission yeast growth. *Current Biology* **19,** 1096–1101 (2009).

17. Dmitrieff, S. & Nédélec, F. Membrane mechanics of endocytosis in cells with turgor. *PLoS computational biology* **11,** e1004538 (2015).

18. Carlsson, A. E. & Bayly, P. V. Force generation by endocytic actin patches in budding yeast. *Biophysical journal* **106,** 1596–1606 (2014).

19. Wang, X., Galletta, B. J., Cooper, J. A. & Carlsson, A. E. Actin-regulator feedback interactions during endocytosis. *Biophysical journal* **110,** 1430–1443 (2016).

20. Nickaeen, M., Berro, J., Pollard, T. D. & Slepchenko, B. M. Actin assembly produces sufficient forces for endocytosis in yeast. *Molecular biology of the cell,* mbc–E19 (2019).

21. Scher-Zagier, J. K. & Carlsson, A. E. Local turgor pressure reduction via channel clustering. *Biophysical journal* **111,** 2747–2756 (2016).

22. Schöneberg, J. *et al.* Lipid-mediated PX-BAR domain recruitment couples local membrane constriction to endocytic vesicle fission. *Nature communications* **8,** 15873 (2017).

23. Berro, J., Sirotkin, V. & Pollard, T. D. Mathematical modeling of endocytic actin patch kinetics in fission yeast: disassembly requires release of actin filament fragments. *Molecular biology of the cell* **21,** 2905–2915 (2010).

24. Steigmann, D. Fluid films with curvature elasticity. *Archive for Rational Mechanics and Analysis* **150,** 127–152 (1999).

25. Aguet, F., Antonescu, C. N., Mettlen, M., Schmid, S. L. & Danuser, G. Advances in analysis of low signal-to-noise images link dynamin and AP2 to the functions of an endocytic checkpoint. *Developmental cell* **26,** 279–291 (2013).

26. Cocucci, E., Aguet, F., Boulant, S. & Kirchhausen, T. The first five seconds in the life of a clathrin-coated pit. *Cell* **150,** 495–507 (2012).

27. Cocucci, E., Gaudin, R. & Kirchhausen, T. Dynamin recruitment and membrane scission at the neck of a clathrin-coated pit. *Molecular biology of the cell* **25,** 3595–3609 (2014).

28. Kukulski, W., Schorb, M., Kaksonen, M. & Briggs, J. A. Plasma membrane reshaping during endocytosis is revealed by time-resolved electron tomography. *Cell* **150,** 508–520 (2012).

29. Chen, B.-C. *et al.* Lattice light-sheet microscopy: imaging molecules to embryos at high spatiotemporal resolution. *Science* **346,** 1257998 (2014).

30. Doyon, J. B. *et al.* Rapid and efficient clathrin-mediated endocytosis revealed in genome-edited mammalian cells. *Nature cell biology* **13,** 331 (2011).

31. Dambournet, D., Hong, S., Grassart, A. & Drubin, D. in *Methods in enzymology* 139–160 (Elsevier, 2014).

32.   Liu, T.-l. *et al.* Observing the cell in its native state: Imaging subcellular dynamics in multicellular organisms. *Science* **360,** eaaq1392 (2018).

33.   Schöneberg, J. *et al.* 4D cell biology: big data image analytics and lattice light-sheet imaging reveal dynamics of clathrin-mediated endocytosis in stem cell–derived intestinal organoids. *Molecular biology of the cell* **29,** 2959–2968 (2018).

34.   Schmid, S. L. A nostalgic look back 40 years after the discovery of receptor-mediated endocytosis. *Molecular biology of the cell* **30,** 1–3 (2019).